Title
The Micro-Accelerator Platform

Author
McNeur, Joshua Clarke

Publication Date
2014

Peer reviewed|Thesis/dissertation

University of California
Los Angeles

The Micro-Accelerator Platform

A dissertation submitted in partial satisfaction
of the requirements for the degree
Doctor of Philosophy in Physics

by

Joshua Clarke McNeur

2014

Abstract of the Dissertation

The Micro-Accelerator Platform

by

Joshua Clarke McNeur

Doctor of Philosophy in Physics

University of California, Los Angeles, 2014

Professor James B. Rosenzweig, Chair

Multiple applications in attosecond science, standoff nuclear detection, oil-well logging, and medicine require the use of compact high-gradient accelerators. The microstructure-based field of Dielectric Laser Accelerators (DLA's) leverages high-power optical lasers and well-established nanofabrication techniques to accelerate electrons with GV/m electromagnetic fields over mm-scale distances, thus filling providing compact high-gradient acceleration. The Micro-Accelerator Platform (MAP) is a micron-scale slab-symmetric resonant-cavity DLA that accelerates electrons with a potential acceleration gradient approaching 1 GeV/m. In principle, electrons are synchronously accelerated as they traverse the standing wave resonance in the MAP's vacuum cavity, excited by a side-coupled Ti:Sapphire laser and confined by Distributed Bragg Reflectors above and below the vacuum cavity. Extensive analysis, simulations, and a proof-of-principle experiment show that the MAP is a viable candidate for compact high-gradient acceleration.

A simplified model of the MAP is used to develop analytic expressions of the resonant fields and associated forces in the vacuum cavity of the MAP. These resonant fields are shown to be capable of accelerating electrons with GeV/m acceleration gradients with no transverse defocusing.

To examine the dependence of the quality and frequency of the MAP's resonance on it's geometry and component materials, simulations in the frequency-domain EM solver HFSS and the time-domain EM solver and PIC code VORPAL are utilized. After a set of design parameters and materials that are practical to fabricate has been detailed, the quality of the MAP's resonance, spectral characteristics of the MAP, error tolerances of the design, ability of the resonance to accelerate electrons, and transverse dynamics of electrons traversing the MAP are presented via simulation results.

Optical lithography and sputtering deposition techniques are used to fabricate the final design of the MAP. After characterization of the fabricated sample is described, the testing of the MAP at the Next Linear Collider Test Accelerator is discussed. A 60 MeV electron beam traverses the MAP as it is illuminated by a Ti:Sapphire laser. The energy spectra of the beam after having passed through the illuminated MAP is then compared to the energy spectra of the beam after having passed through the MAP without laser illumination in order to deduce whether acceleration has occurred. The strength of acceleration versus the relative timing of the laser and electron beam is examined. It is deduced that for a subset of the data collected, the MAP accelerated electrons with a 50.6 MeV/m accelerating gradient. The implications of this finding and potential ways to increase the accelerating gradient are discussed.

The dissertation of Joshua Clarke McNeur is approved.

Warren Grundfest

Warren Mori

Pietro Musumeci

Gil Travish

James B. Rosenzweig, Committee Chair

University of California, Los Angeles

2014

This dissertation is dedicated to my family, John, Clare, Catherine, and Luke McNeur and my advisor, Gil Travish. Without their support and guidance, the work detailed here would have never happened.

Table of Contents

1 Introduction **1**

1.1 A Brief History of Conventional Linear Accelerators 2

1.1.1 The Wideroe LINAC 3

1.1.2 Development into the Modern RF LINAC 3

1.1.3 The Limitations of RF LINACs 4

1.2 The Optical Regime 5

1.2.1 Dielectric Materials and Field-Induced Breakdown 7

1.2.2 Power Sources and Fabrication 7

1.3 The Micro-Accelerator Platform 9

1.3.1 Design 10

1.3.2 The Accelerating Mode 12

1.3.3 The Monolithic MAP 12

1.4 Other Dielectric Laser Accelerators 14

1.4.1 Photonic Bandgap Structures 15

1.4.2 The Woodpile 16

1.4.3 The Grating Structure 17

1.4.4 Experiments To Date 19

1.5 Applications of the MAP 20

1.5.1 Stand-off Nuclear Detection 20

1.5.2 Attosecond Time Scale 21

1.5.3 The MAP for Cancer Therapy 22

1.6 Thesis 23

2 Theory **24**

2.1 The MAP as a Resonant Cavity 24

2.1.1 A Simplified Standing Wave Resonator 24

2.1.2 The Resonant Fields 25

2.1.3 An Analytical Model 28

2.2 The Dynamics of Acceleration 30

2.2.1 Longitudinal Dynamics 31

2.2.2 Transverse Dynamics 32

2.2.3 An Analytical Model of the Actual MAP 33

3 Simulations **35**

3.1 Process Flow 35

3.2 Tools Used 36

3.2.1 HFSS 36

3.2.2 VORPAL 38

3.2.3 Other Software 39

3.3 Resonance 40

3.3.1 Characteristics of a Strong Resonance 40

3.3.2 Mode Excitation in Dielectrics 42

3.3.3 Three-D Field Variation 45

3.3.4 Designs Considered 47

3.3.5 Spectral Characterization 50

3.3.6 Temporal Characteristics of the Resonance 53
3.3.7 Error Tolerance 57
3.4 Acceleration and Dynamics in the Relativistic Design 60
3.4.1 Acceleration due to Standing Wave Resonance 60
3.4.2 The Expected Accelerated Signal 61
3.4.3 Phase Stability 65
3.4.4 Transverse Dynamics 65
3.4.5 Wakefields 67
3.4.6 Space Charge 68

4 Experiment 71
4.1 Fabrication 71
4.1.1 Fabrication Processes 71
4.1.2 Measuring Structure Parameters 75
4.1.3 Optical Testing 79
4.2 Experimental Setup 82
4.2.1 Test Facility 82
4.2.2 Experimental Procedure 89

5 Acceleration Testing: Results and Analysis 98
5.1 Analysis Methods 99
5.2 Acceleration Tests 100
5.2.1 Electron Energy Spectra 101

5.2.2 Cross-correlation of Energy Gain and Relative Timing in Run 9 103
5.2.3 The Spatial Overlap of the Electron Beam and the IR Pulse 110
5.2.4 Rotation and Tip of the the MAP Sample 112
5.2.5 Fluence of the Incident IR 114
5.3 Summary and Discussion 116
5.4 Conclusion 120

6 Addendum 124
6.0.1 Particle Dynamics in the Sub-Relativistic Regime 124
6.0.2 Resonance in the Subrelativistic MAP 128

References 134

List of Figures

1.1 A Standing Wave Iris-Coupled Linear Accelerator composed of Copper. 4

1.2 An illustration of synchronous acceleration of a short electron bunch over one optical cycle of the incident laser (and accelerating mode resonance). In this illustration, the bunch sees accelerating fields. 5

1.3 Maximum surface electric field versus pulse length for X-band structures made of different materials: copper (x's), gold-plated (squares), and stainless steel (diamonds). Taken from Figure 2 of Ref. 13. 6

1.4 Breakdown fluence of thin film Fused Silica as a function of laser pulse length for wavelengths of 825nm and 1024nm. Taken from Figure 3 in Ref. 9. 7

1.5 The frequency and fluence for a set of power sources with the potential to power accelerating structures. Note that the output power fluences of these sources increases as their output wavelengths decrease. 8

1.6 A schematic design of a few periods of a cross-section of the MAP. The structure is periodic horizontally and invariant into the page. 10

1.7 The nonzero electric field components of the standing wave resonance in one period of a cross section of the MAP. The incident laser is propagating from the top of the image to the bottom and fields are represented with a color overlay. The amplitude of the legend is relative to the amplitude of the incident field source. . . 13

1.8 A schematic of the Monolithic MAP, designed to produce electrons and accelerate them to 1 MeV or more. 14

1.9 a. A image of the design of a Photonic Bandgap Fiber where the horizontal and vertical axes correspond to relative horizontal and vertical displacement respectively. b. A color overlay of the longitudinal component of the electric field in this PBG [21]. This image is taken from Figure 4 of Ref. 21. 16

1.10 The log-cabin style design of the Woodpile PBG Accelerator [23]. This image is taken from Figure 1 of Ref. 23. 17

1.11 An image of the fabricated woodpile structure [23]. This image is taken from Figure 4 of Ref. 23. 17

1.12 The design of the Grating Accelerator. λ is typically 800nm [27]. This image is taken from Figure 1 of Ref. 27. 18

1.13 Energy Modulation in the Grating [28]. This image is taken from Figure 2 of Ref. 28. 19

1.14 An illustration of stand-off nuclear detection. The X-Ray source in this image can be an array of MAPs. 20

1.15 The momenta distribution of p-orbital electron in an Argon gas, imaged using an attosecond X-ray bunch train [29]. This image is taken from Figure 3c of Ref. 29. 22

1.16 The stopping range (left) and power (right) of 1-6 MeV electrons in soft tissue. This image is taken from Ref. 30. 23

2.1 A schematic design of one period of a cross-section of the Ideal DLA. The structure is periodic in the z direction and invariant in the x direction (into the page). 25

2.2 A schematic design of a one periods of a cross-section of a simplified MAP, with reference labels for relevant parameters. 28

2.3 A color overlay of the fields solved for in a Bragg Accelerator device by Mizrahi and Schachter. Blue corresponds to positive fields and red negative. The black and white image on the end of the overlay shows the structure, a vacuum gap surrounded by two DBRs. This image is taken from Figure 5 of Ref. 31 34

3.1 The Micro-Accelerator Platform as implemented in HFSS. A plane wave is incident from the top left, surfaces 1 and 2 have perfect magnetic boundary conditions, surface 3 has a radiative boundary condition and the model is periodic in the z direction. 37

3.2 The Mesh generated by HFSS when solving for the electromagnetic fields in a typical MAP design. 37

3.3 The non-zero electric field components of the standing wave resonance in one period of a cross section of the MAP. The incident laser is propagating from the top of the image to the bottom and fields are represented with a color overlay. The amplitude of the legend is relative to the amplitude of the incident field source. . . 41

3.4 The resonant frequency of a MAP design as a function of substrate thickness 43

3.5 E_z in the substrate of the MAP model when the accelerating mode is excited. The node to node distance is 380nm. 44

3.6 A cross-section color overlay of E_z in a fully 3-dimensional MAP model in HFSS. Note the variation of E_z with respect to x (into the page) as a result of edge reflections. 46

3.7 E_z as a function of x in a MAP model that incorporates edges in x. Twelve microns away from the edge, the variation of E_z reduces to less than 10 percent. The ripples in E_z near the edge of the structure are due to the impedance mismatch at the edge. 47

3.8 Legend with the geometric parameters labelled for reference. . . . 50

3.9 The transmittance/reflectance of the MAP as a function of frequency on the left/right. Ptrans refers to the transmitted power, Pref the reflected power and Pin the incident power. Each plot point represents a separate simulation; the point density is higher near the central resonance 51

3.10 A color overlay of E_z for a Fabry-Perot Mode of the MAP. The incident plane wave travels from the left to the right. The invariance of E_z with respect to z makes this mode non-accelerating. 52

3.11 A color overlay of E_z for an anti-symmetric mode excited in the MAP. The incident plane wave travels from the left to the right. E_z is zero on axis and thus incapable of accelerating charged particles. 52

3.12 The incident source in the VORPAL time-based simulations of the MAP. It is a sine wave with a near-infrared central wavelength and a gaussian envelope. 54

3.13 A color overlay of the longitudinal component of the electric field in the standing wave accelerating mode in the MAP, as simulated in VORPAL The field is shown after the cavity has been illuminated by a incident laser for 5 ps (the fill time of the structure). Red corresponds to accelerating fields and blue to decelerating fields. . 55

3.14 The amplitude of the longitudinal component of the standing wave accelerating mode in the vacuum gap of the MAP as a function of time. The incident source, indicated by the black line, is abruptly terminated at a time of 36 ps. 56

3.15 The field amplitude in the vacuum cavity of the MAP as a function of the standard deviation of the gaussian envelope of the incident source. The peak amplitude of the incident source is 1 GV/m. . . 56

3.16 The energy profile of an electron bunch at injection (injected at 60 MeV) and 1mm after injection. The maximum field gradient in the accelerating cavity is 2 GV/m. The energy profile broadens slightly due to different electrons in the bunch encountering different amplitude fields. The electron bunch length is 1/40th the length of the wavelength of the accelerating mode in the MAP. . . 61

3.17 Illustration demonstrating the means of energy modulation as the NLCTA electron beam travels through the MAP. 62

3.18 Energy distribution of electron bunch after having traveled through the MAP in G4beam-line. The initial energy distribution matches the initial energy distribution of Figure 3.16. 63

3.19 Energy distribution of electron bunch after having traveled through the MAP in with a 0.4 GV/m accelerating mode excited (a field amplitude chosen to reflect modest experimental goals). The zeroth bin corresponds to 59 MeV and the bin size is 2 keV/bin. . . 63

3.20 Energy distribution of the transmitted electron bunch after having traveled through the MAP in with a 0.4 GV/m accelerating mode excited. The vertical axis shows the percentage of the electron bunch with a certain energy relative to the total transmitted population. 64

3.21 The energy distribution of an electron bunch after having travelled through the MAP's accelerating mode in Mathematica (with no phase slippage assumed) and in VORPAL (with all potential phase slippage causes accounted for) as a function of phase. 66

3.22 The transverse spot size of the electron beam as it traverses the cavity in two cases: with the accelerating mode excited and with the laser off. 67

3.23 A color overlay and line out of the longitudinal component of the electric wake fields generated by a 10 fC beam passing through the MAP's accelerating cavity. The periodicity of the fields generated by the beam is a multiple of the longitudinal beam length. 68

3.24 The transverse spot size of a 50 fC electron bunch after it has traversed the MAP's vacuum cavity for 1mm with no accelerating mode excited. The initial spot size is 400nm tall by 50nm wide. . 69

3.25 The transverse spot size of a 50 fC electron bunch after it has traversed the MAP's vacuum cavity for 1mm with no accelerating mode excited. The initial spot size is 400nm tall by 10μm wide. . 70

4.1 A series of fabrication steps summarizing how the coupling slots are patterned and deposited [38]. 73

4.2 A series of fabrication steps summarizing how the DBR and metal spacers are deposited [38]. 74

4.3 An optical image of the MAP after it has been fabricated, bonded, and diced. The blue regions correspond to the sections in which the top and bottom halves of the MAP are aligned. In the experiment described in section 4.2.2, electrons traverse these blue "accelerating regions" from the bottom of the figure to the top. The IR laser is incident into the page. The black regions correspond to the sections of the MAP sample onto which the metallic spacers were deposited. 75

4.4 A SEM image of the top half of the MAP accelerator. Three coupling slots, as well as the DBR and matching layers are visible. 76

4.5 The set-up of a generic spectrophotometer [40]. 80

4.6 The transmitted light through the MAP as a function of wavelength for 3 fabricated MAP samples and the simulated MAP design. 81

4.7 A simplified overview of the NLCTA beam-line. Although not all of the focusing/steering quadrupoles are accounted for, the overall schematic is correct. 85

4.8 An image of the electron beam on the YAG screen at the same longitudinal position as the MAP sample. The beam, used in the data described in sections 5.2.1 and 5.2.2, is fitted to a gaussian in both x and y. The fitted FWHM is 25 microns in x and 15 microns in y. 87

4.9 A diagram of the final section of the E-163 beam-line, including the interaction with the MAP itself. Ideally, the electron beam is focused to a small spot at the MAP's location, where an IR laser pulse has excited the accelerating mode. Downstream of the MAP, the beam traverses a 90 degree bend magnet that serves as an energy profile diagnostic. 88

4.10 A schematic of the final section of the experimental hall, with the fast photodiode's position indicated. Note that the OTR and IR signals travel straight through the spectrometer bend magnet. . . 91

4.11 An Image of the back of the MAP sample while it is both illuminated by the IR laser and struck by the electron beam. The reflections of the IR beam are visible on the top edge of the top half of the MAP sample, the middle surface where the top and bottom halves meet and the surface where the bottom half touches the DLA holder. The optical transition radiation generated by the electron beam hitting the sample is visible on the middle surface, next to the IR reflection. 92

4.12 An Image of the MAP in which the top surface is not perpendicular to the propagating direction of the incident laser source. 93

4.13 The setup used to confirm that the IR is perpendicular to the top surface of the MAP surface. When perpendicularity is achieved to within .01 degrees, the incident (red) and reflected (orange) spots overlap on the screen. 94

4.14 An image of the Lanex phosphor screen downstream of the spectrometer bend magnet when the electron beam is straddling the top edge of the MAP sample. The x-axis of this screen is correlated with energy. The broader, lower energy distribution to the left corresponds to the electron population that has scattered through the glass and lost energy to the glass. The thinner higher energy population corresponds to the electrons that have passed over the top of the glass. 95

4.15 A line out of the energy spectrum of the NLCTA beam after having traversed the MAP. The thinner population to the right (higher energy) corresponds to those electrons that were transmitted through the acceleration channel. The broader peak on the left corresponds to those electrons that scattered through the glass/dielectric materials of the MAP. 96

5.1 The energy profile of an electron bunch from the NLCTA after having traversed the cavity with no resonating mode excited (left) and with laser illumination (right). 101

5.2 Energy profiles of electron bunches collected during Run 9 with no resonant mode excited (left) and with the resonant mode excited (right). 102

5.3 The width of the transmitted electron distribution as a function of the relative timing of the electron beam and the incident IR. Red dots correspond to the IR laser being on and blue dots correspond to the IR laser being off. 104

5.4 The energy spectrum of an electron beam that has traversed the LINAC upstream at a drifted phase (left) and at the optimal phase (right). Note that the straggled glass population in the left spectrum is wider than the same population on the right. These spectra are taken from Run 9. 105

5.5 The peak of the portion of the electron distribution that has lost energy to the glass substrate as a function of the relative timing of the electron beam and the incident IR. Red dots correspond to the IR laser being on and blue dots correspond to the IR laser being off. 106

5.6 The width of the transmitted electron population versus the relative timing of the IR and electron beam. Laser-on data are red dots and laser-off data are blue dots. The lines denoted by σ represent the mean of the laser-off data plus 1, 2, and 3 standard deviations of the laser-off data. The zoomed in region of interest is highlighted in the image on the right. Data was collected during Run 9. 107

5.7 Energy profiles of electron bunches collected during Run 9 with no resonant mode excited (left) and with the resonant mode excited (right). The broadening of the transmitted population on the right is indicative of acceleration. 108

5.8 The gaussian r.m.s. of the transmitted population of electrons for an electron beam traversing the grating structure described in section 1.3.1.3 with the laser illuminating the structure (orange) and the laser off (blue). The laser on data fits to a sech^2 function, as is expected for electrons being accelerated by a standing wave [28]. This Figure is taken from Figure 3a of Ref. 21. 109

5.9 The gaussian r.m.s. of the straggled populations of electrons (that had lost energy to the glass). As data was collected the event number increased from 1 to 528 in this data set. Between event numbers 150 and 250, the width of the straggled population increases, indicating a degradation in beam quality. Although this is corrected after event 250 through beam tuning, there are many events with widths indicative of beam degradation after event 250. 110

5.10 The figure of merit K as a function of the relative spatial overlap of the laser and electron beam. At an overlap of 0 microns, the strongest acceleration signal is seen. This corresponds to the data set in Figure 5.6 112

5.11 The figure of merit K as a function of the rotational orientation of the MAP sample. At an rotation of 0 degrees, the strongest acceleration signal is seen. This corresponds to the data set in Figure 5.6 113

5.12 The figure of merit K as a function of the tip orientation of the MAP sample. At an tip of 0 degrees, the strongest acceleration signal is seen. This corresponds to the data set in Figure 5.6. The dotted line shows the calculate acceleration signal strength based on the analysis in section 4.2.2.4. 115

5.13 The width of the transmitted electron population versus the relative timing of the IR and electron beam. Laser on data are red dots and laser-off data are blue dots. The fluence of the incident IR is .071 J/cm^2. 116

5.14 An optical microscope image of the top surface of the MAP sample tested in Run 9. Damage due to high-fluence IR exposure is evident.117

5.15 An optical microscope image of the top surface of the MAP sample tested in Run 9. The missing DBR (the top section of the sample in which only a transparent substrate is visible) and darkened region to the left are indicative of the occlusion of the vacuum cavity caused by the dicing process. 119

6.1 A top-down image of the sub-relativistic map. The black lines correspond to the slot positions in the original design, placed $\beta_s\lambda$ apart, where β is v/c and λ is 800 nm. The orange lines correspond to the new dithered positions. 125

6.2 Four snapshots of the on-axis electric field seen by a sub-relativistic electron bunch when the standing wave accelerating mode has a 800 nm wavelength. 129

6.3 Cross sectional field overlay of fields excited in 2.4 micron period structure. 130

6.4 On axis fields for the newly proposed sub relativistic scheme. . . . 131

6.5 Snapshots in time showing method in which electrons are accelerated by the distorted standing wave resonance. 132

6.6 Energy spectrum of electrons before and after having travelled through 250 microns of a structure designed to accelerate 25 keV electrons. 132

List of Tables

1.1 Accelerator Energies and Sizes. 2

3.1 Varying the Size of the MAP in x. 48

3.2 Properties of Materials Considered for the MAP Design. 49

3.3 Material Combinations Used in Designs. 50

3.4 The MAP Design Materials and Parameters. 51

3.5 Comparing the MAP in HFSS and VORPAL. 54

3.6 Error Tolerances for Resonant Quality. 58

3.7 Error Tolerances for Resonant Frequency. 59

4.1 Fabricated MAP Parameters. 77

4.2 Fabricated MAP Parameters for First MAP Design. 78

4.3 Requirements for A Facility in which MAP can be Tested. 84

4.4 NLCTA Nominal Electron Beam Parameters for E163 Operation. 86

5.1 Summary of Experimental Testing of the Micro-Accelerator Platform. 99

Acknowledgments

The author would like to thank Gil Travish for his tireless efforts on both leading the MAP project and providing guidance throughout the author's tenure at UCLA. Moreover, the work of the other MAP team members, including but not limited to Esin Sozer, Kiran Hazra, Jianyun Zhou, Nestor Carranza, Zach Hoyer, Ritika Dusad, Ninel Vartanian and Esperanza Arab made the MAP project possible. Without the assistance of the E-163 team at SLAC, including Joel England, Ken Soong, Edgar Peralta and Ziran Wu, the experimental testing of the MAP would not have been possible. Finally, the author is grateful for the extensive editing of Rodney Yoder and Joe Duris.

Vita

2007	B.S. w Honors (Mathematics) and B.S. w Honors. (Physics), University of Chicago.
2009-2013	Graduate Student Researcher, Physics Department, UCLA.

Publications

E. Peralta, J. McNeur et al., ”Demonstration of Electron Acceleration in a Laser-Driven Dielectric Micro-Structure,” Nature Vol.503, No.7474, 91-94 (2013).

J. McNeur et al., ”The Experimental Search for Acceleration in the Micro-Accelerator Platform, Proc. 1st Intl. Particle Accelerator Conference (IPAC13), 1307-1309 (2013).

E. Sozer, J. McNeur et al., ”Numerical Modeling and Experimental Data Analysis for Dielectric Laser Accelerators, Proc. 1st Intl. Particle Accelerator Conference (IPAC13), 1310-1312 (2013).

J. McNeur et al., ”Resonance, particle dynamics, and particle transmission in the micro-accelerator platform,” AIP Conf. Proc. 1507, 470 (2012).

J. McNeur et al., ”A monolithic relativistic electron beam source based on a dielectric laser accelerator structure,” AIP Conf.Proc. 1507, 464 (2012).

G. Travish, J. McNeur et al., ”Experimental Progress Towards a Resonant Slab-Symmetric Dielectric Laser Accelerator, Proceedings,” 1st Intl. Particle Accelerator Conference (IPAC12), 2738-2740 (2012).

J. McNeur et al., ”Using Simulations to Understand Dynamics and Resonance in the MAP,” 1st Intl. Particle Accelerator Conference (IPAC12), 2372-2374 (2012).

J. McNeur et al., ”Resonance, Particle Stability and Acceleration in the Micro-Accelerator Platform,” Proc. 1st Particle Accelerator Conference Proceedings, 121-123 (2011).

J. Zhou, J. McNeur, et al., ”Fabrication of a Prototype All-Dielectric Micro-Accelerator,” AIP Conf. Proc. 1299, 433 (2010).

J. McNeur et al., ”An Examination of Resonance, Acceleration, and Particle Dynamics in the Micro-Accelerator Platform,” AIP Conf. Proc. 1299, 427 (2010).

J. McNeur et al., ”A Tapered Dielectric Structure for Laser Acceleration at Low Energy,” Proc. 1st Intl. Particle Accelerator Conference (IPAC10), 4387-4389 (2010).

CHAPTER 1

Introduction

The search for new discoveries in particle physics has been the primary motivator for accelerator development. Since the creation of high energy density is essential for these discoveries, accelerator technology has produced beams with increasingly greater final energies in increasingly smaller spot sizes. Since the transverse spot size σ of a charged particle beam scales with the final energy γ as $\sigma \propto \gamma^{-1/2}$, the latter is correlated with the former. For example, the Large Hadron Collider at CERN produces proton bunches with energies exceeding 1 TeV and transverse spot sizes on the order of tens of microns [1]. Table 1.1 shows that the size of an accelerator inevitable scales with the final energy of the particles it accelerates. However, the cost of an accelerator also scales with its size. A 2008 survey shows that the cost of a typical linear accelerator is roughly 100M USD per km [2]. For an accelerator such as the Large Hadron Collider that produces particle beams with energies exceeding 1 TeV, the total cost exceeds 6B USD [1].

On the other hand, new discoveries in particle physics (as well as attosecond science, medical physics and other fields) can potentially be found with laser-based accelerators. Laser-based accelerators operate in a different regime than the accelerators in Table 1.1 (with ramifications that are discussed throughout the entirety of this dissertation): they are low-cost and tabletop-size but also able to produce high-energy and high-quality beams [5]. In order to use laser power sources to impart energy to particles, these advanced accelerators must be able

Table 1.1: Accelerator Energies and Sizes.

Accelerator	**Final Energy**	**Size**
Cosmotron	3.3 GeV	72 meter (Circumf.)
SLAC LINAC	50 GeV	3 km
LEP Collider	90 GeV	27 km (Circumf.)
Tevatron	980 GeV	6.3 km (Circumf.)
LHC	4 TeV	27 km (Circumf.)

to confine and shape the high-gradient electromagnetic fields produced by the laser sources. This field-shaping can be accomplished with either plasma confinement [3] or structure-based confinement. Structure-based confinement provides the advantage of high-precision field control and an unobstructed particle path [4]. Among those accelerators that utilize structure confinement, the optically-powered accelerators are known as Dielectric Laser Accelerators (DLA's) [5] (since the only way to achieve structure-based confinement at optical frequencies is with the use of dielectrics – see section 1.2.1). This class of accelerator is the focus of this dissertation.

1.1 A Brief History of Conventional Linear Accelerators

RF-powered Linear Accelerators (LINAC's) were first designed in the late 1920s. For the next century, their designs and operating parameters were optimized to accelerate charged particles to higher energies with higher energy gradients. In fact, the mechanism by which conventional LINAC's accelerate charged particles is utilized by the accelerator that is the subject of this work. However, for reasons that are described in section 1.1.3, RF-powered LINAC's are limited in the energy gradients that they yield. This limitation in field gradient motivated the birth of the field of DLA's.

1.1.1 The Wideroe LINAC

A linear accelerator (LINAC) is a device that increases the energy of charged particles as they traverse a linear series of cavities in which electromagnetic fields exist. The first LINAC was conceptualized by Szilard and later patented by Widerøe in 1928 [6]. The principle of acceleration in the Widerøe LINAC (an example of a Drift Tube LINAC) is that charged particles traverse cavities with temporally oscillating electromagnetic fields powered by MW radio-frequency (RF) source. These cavities are separated by copper tubes in which no field is excited. The lengths of the cavities and tubes are determined so that whenever an electron passes through a cavity, it sees an accelerating field, resulting in a net energy gain.

1.1.2 Development into the Modern RF LINAC

The Linear Accelerator has appeared in many variations [7-9]. The general operating principle of RF-powered Linear Accelerators is that charged particles (e.g. electrons, protons, positrons) traverse a series of vacuum cavities in which electromagnetic fields have been excited by a RF source [10]. The fields and timing of the charged particles' passage are designed in a manner that ensures that the particles see more accelerating fields than decelerating fields. As a result, a net energy gain is imparted to the particles [11]. For RF electron LINAC's, MW power sources at GHz operating frequencies and 10-100 MeV/m acceleration are typical. An image of a generic standing wave iris coupled LINAC is given in Figure 1.1. Radio-frequency power enters each cavity and excites an standing wave electromagnetic field that accelerates electrons.

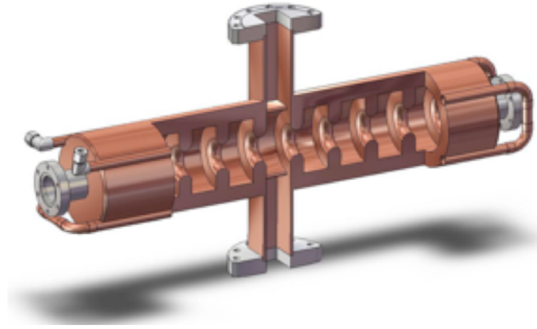

Figure 1.1: A Standing Wave Iris-Coupled Linear Accelerator composed of Copper.

As electrons traverse this standing wave, they encounter electromagnetic fields that oscillate in time with the same temporal period as the incident RF source. For electrons traveling relativistically, the distance travelled over one temporal period is equal to the wavelength of the incident source. If this distance matches the wavelength of the standing wave in the cavity, synchronous acceleration occurs. This is illustrated in Figure 1.2.

1.1.3 The Limitations of RF LINACs

RF accelerators are widely used and robust in the sense that they can function in beam-lines for multiple years. However, they are ill suited for high-gradient acceleration for a few reasons. First, the output power of RF power sources is limited: the maximum intensity of a X-Band source is limited to 10 W/cm^2 (see Figure 1.5. Second, for X-Band RF accelerators, the maximum field gradient supported in the accelerating cavities is 80 MV/m [13] (see Figure 1.3). At shorter wavelengths (e.g. 800nm), this breakdown threshold only slightly improves to 100 MV/m [12]. Third, since the particle beam size scales with the wavelength

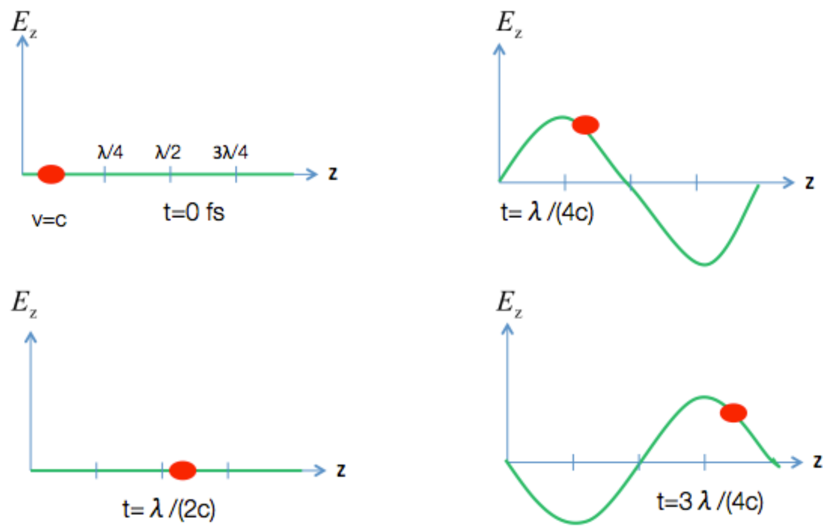

Figure 1.2: An illustration of synchronous acceleration of a short electron bunch over one optical cycle of the incident laser (and accelerating mode resonance). In this illustration, the bunch sees accelerating fields.

of the source, RF accelerators are limited in the bunch length of beams they can produce.

RF accelerators are thus far incapable of achieving compact high gradient acceleration of particle bunches with bunch lengths small enough to probe new physics. On the other hand, optical acceleration is well-suited to reach these goals of compact acceleration and ultrashort particle bunches.

1.2 The Optical Regime

For a source with power P, the peak electric field strength E that the source generates scales inversely with the source's central wavelength λ.

$$E \propto \frac{P}{\lambda}. \tag{1.1}$$

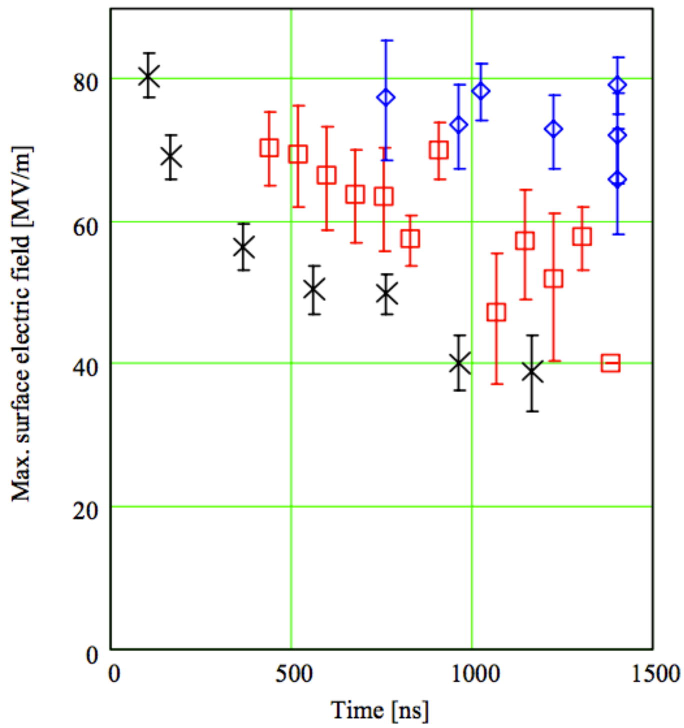

Figure 1.3: Maximum surface electric field versus pulse length for X-band structures made of different materials: copper (x's), gold-plated (squares), and stainless steel (diamonds). Taken from Figure 2 of Ref. 13.

Thus, smaller wavelength sources provide higher energy gradients for acceleration. To achieve higher gradient acceleration while simultaneously leveraging available power sources and fabrication techniques, optical and near-optical laser sources have been considered to power the electromagnetic fields used to accelerate particles, for reasons that will be elaborated upon in sections 1.2.2 and 1.2.3. However, the metals commonly used in RF accelerators cannot withstand the high-gradient (GV/m) electromagnetic fields produced by optical sources and as a result, non-metals with different high-field behavior must be considered as the materials composing optical accelerators.

1.2.1 Dielectric Materials and Field-Induced Breakdown

Copper, the material most commonly used in RF accelerators, is not a suitable material in optical scale accelerators as it breaks down at the field gradients that an optical laser generates [12]. Instead, dielectric materials are strong candidates for being used in optical-scale laser-powered accelerators, as these materials can withstand laser fluences exceeding 1 J/cm^2 and electromagnetic field gradients exceeding 1 GV/m. The breakdown fluence of fused silica, a dielectric material widely used in optical-scale laser-powered accelerators, is shown in Figure 1.4 as a function of laser pulse length for near-optical sources.

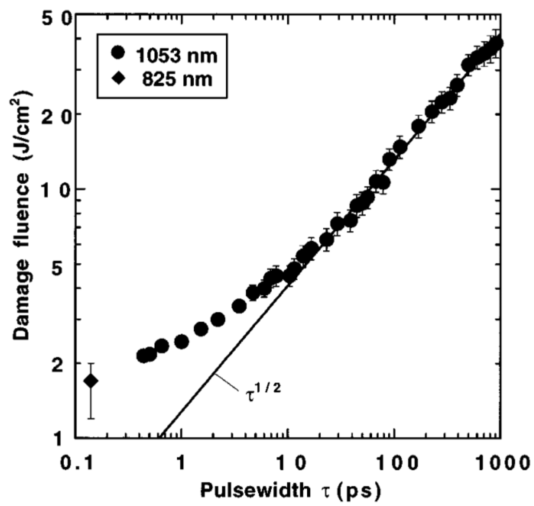

Figure 1.4: Breakdown fluence of thin film Fused Silica as a function of laser pulse length for wavelengths of 825nm and 1024nm. Taken from Figure 3 in Ref. 9.

1.2.2 Power Sources and Fabrication

High power sources in the optical and near infrared wavelength regimes that can generate GV/m fields are readily available. For instance, GW-power Ti:Sapphire lasers, capable of creating GV/m fields in DLA's, are standard even in small accelerator facilities [14].

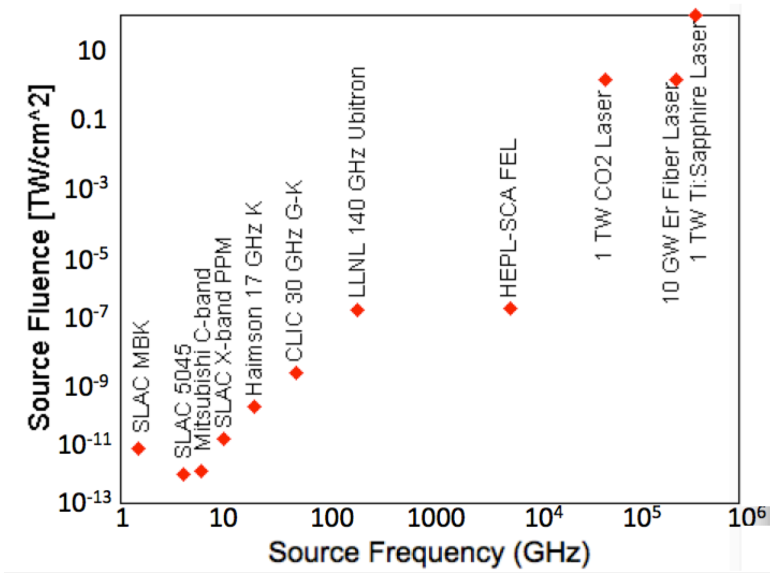

Figure 1.5: The frequency and fluence for a set of power sources with the potential to power accelerating structures. Note that the output power fluences of these sources increases as their output wavelengths decrease.

Figure 1.5 details the kinds of power sources available with wavelengths smaller than RF wavelengths. Among the output wavelengths spanned by these sources, there is an optimal range that balances the desire to achieve GV/m fields and the practicality of fabricating a DLA with feature sizes comparable to the source wavelength: the optical regime. For example, a GW Ti:Sapphire laser, with a central output wavelength of 800nm, is capable of generating GV/m electromagnetic fields. An accelerating structure powered by the Ti:Sapphire laser will have feature sizes on the scale of 1 micron; building a structure of this scale is well within the capabilities of nanofabrication facilities. Sputtering a thin film of dielectric material that is hundreds of nanometers thick is common in the field of nanofabrication, as is the process of lithographically patterning a wafer with features that repeat over a period of roughly 1 micron. The specific processes used to fabricate the accelerator that is the focus of this dissertation are detailed in section 4.1.

1.3 The Micro-Accelerator Platform

Dielectric Laser Accelerators leverage optical power sources, the high damage thresholds of dielectric materials, and state-of-the-art nanofabrication techniques to provide low cost, compact high-gradient acceleration and the production of high quality ultrashort beams. Since DLA's operate in a different regime than RF accelerators, the designs of DLA's must taken into account issues related to this new regime. DLA's must efficiently couple optical power to form high-quality accelerating fields (defined in section 3.3.1), suppress higher order modes disadvantageous to acceleration, and minimize the effects of space charge and wakefields induced by the particles passing through the DLA's. The Micro-Accelerator Platform (MAP) is one design in the burgeoning field of DLA's (other designs are discussed in section 1.4) that addresses these issues. The Micro-Accelerator Platform stands out in the DLA regime due to a few advantageous design properties. The MAP has a straightforward energy coupling scheme and smooth inner walls surrounding the acceleration cavity that limit the effects of beam wakefields [17]. Furthermore, the MAP is a resonant cavity accelerator. Thus, for a given incident fluence, the fields supported in the MAP are an order of magnitude greater than the fields in a non resonant accelerator [18].

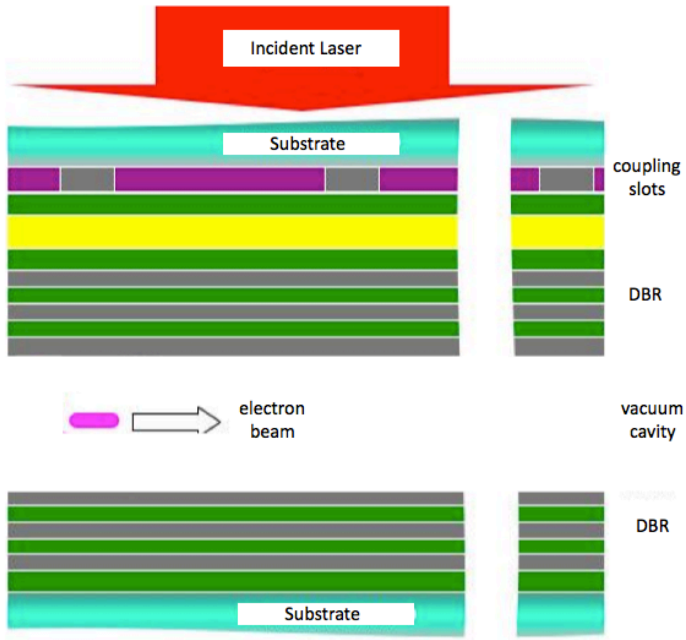

Figure 1.6: A schematic design of a few periods of a cross-section of the MAP. The structure is periodic horizontally and invariant into the page.

1.3.1 Design

1.3.1.1 Distributed Bragg Reflectors

Similar to other DLAs, the Micro-Accelerator Platform is designed in order to yield electromagnetic fields that can accelerate electrons when the structure is illuminated by an optical laser. The accelerating mode of the MAP is a standing wave resonance with a large longitudinal electric field component meant to impart energy to electrons traversing the MAP's vacuum cavity. The longitudinal electric field is designed to have no variation in either transverse dimension in the vacuum gap, so as to minimize transverse beam instabilities. To confine this mode, planar Distributed Bragg Reflectors (DBRs) surround the vacuum gap in which it is excited. A cross section of these DBRs is visible in Figure 1.6. A DBR is composed of two dielectric materials in alternating layers. By setting the layer thicknesses for each dielectric material to one quarter of the wavelength of the standing wave mode being confined, each dielectric interface reflects that mode in such a way that the cumulative effect of the DBR is to serve as a mirror for a mode at the design wavelength. The reflective quality of the DBR increases when the difference between the indices of refraction for the two materials used in it is large. As a result, high contrast materials are desirable to effectively confine the standing wave mode in the vacuum gap of the MAP. Furthermore, the reflection coefficient increases as the number of alternating pairs increases. In Figure 1.6, the top DBR (the set of alternating dielectric layers above the vacuum cavity) serves two purposes. This DBR needs to be transmissive enough to let the incident laser light travel through it but reflective enough to confine the accelerating mode excited in the vacuum cavity beneath it. On the other hand, the bottom DBR (the set of alternating dielectric layers below the vacuum cavity) only needs to confine the accelerating mode in the vacuum cavity above it. Thus, the number of pairs in the top DBR (4) is less than the number of pairs in the bottom DBR (11).

1.3.1.2 Coupling Slots

In order to excite a standing wave field pattern in the vacuum cavity of the MAP, the MAP needs to introduce a longitudinal periodicity to an incoming electric field that is initially invariant in the longitudinal direction (the horizontal axis in Figure 1.6). This is accomplished by introducing a periodic phase mask above the top DBR. This phase mask, consisting of coupling slots with a longitudinal periodicity matching the intended periodicity of the standing wave resonance and surrounded by a second dielectric material with a lower index of refraction, allows the electric field of the incident light to propagate vertically in Figure 1.6 in a manner that is dependent on the longitudinal direction. As the incident laser traverses the coupling slots, the electric field that travels through the higher index of refraction slot evolves in phase more quickly than the electric field that travels through the adjacent material with the lower index of refraction. After traversing matching layers and the aforementioned DBR which allow for the resulting field pattern to develop into a standing wave pattern, the incident light has been transformed into the resonant mode of the MAP.

1.3.2 The Accelerating Mode

The resonant mode of the MAP is a standing wave in the longitudinal component (z) of the electric field. The spatial periodicity of this standing wave matches the periodicity of the coupling slots in the phase mask of the MAP. As is discussed in detail in section 3.3.1, when the quality of the mode is strong, there is little to no variation of the field strength with respect to the transverse dimensions (x and y), so as to prevent transverse instabilities in the particles traversing the fields in the cavity. The different field components of this standing wave are given in Figure 1.7.

1.3.3 The Monolithic MAP

In addition to its viability as a compact high-gradient accelerator, with a few design additions, the MAP can be transformed into a monolithic electron source capable of producing electron bunches with small emittances, high repetition rates and MeV scale energies. This 'Monolithic MAP' has a range of applications that extend beyond the field of accelerator physics and is thus important to consider. Combining the MAP design with a micron-scale electron emitter and a

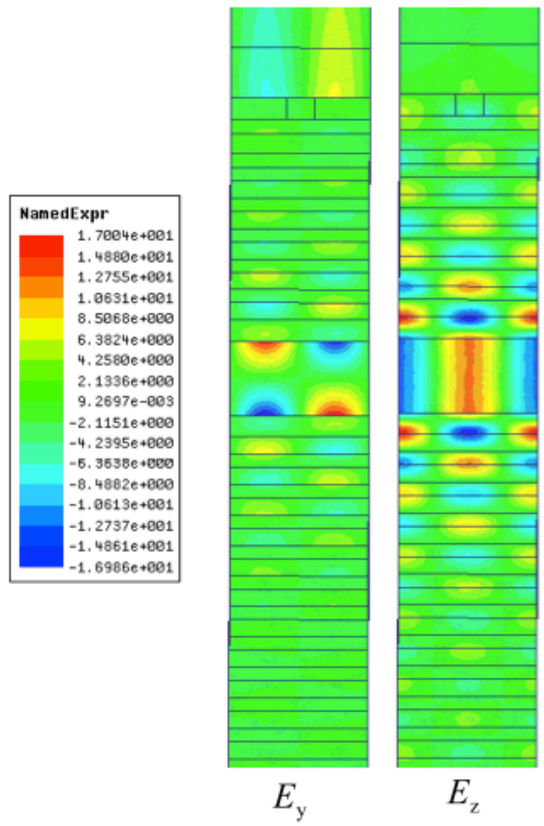

Figure 1.7: The nonzero electric field components of the standing wave resonance in one period of a cross section of the MAP. The incident laser is propagating from the top of the image to the bottom and fields are represented with a color overlay. The amplitude of the legend is relative to the amplitude of the incident field source.

subrelativistic capture section leads to its implementation as a monolithic electron source. Electrons with subrelativistic energies are produced via field-enhanced emission from a thin wedge with a nanometer scale tip radius. The electrons are then captured by a modified MAP region and are accelerated to velocities near the speed of light, at which point the relativistic design described in section 1.4.1 can be employed. To capture and accelerate sub-relativistic electrons a design

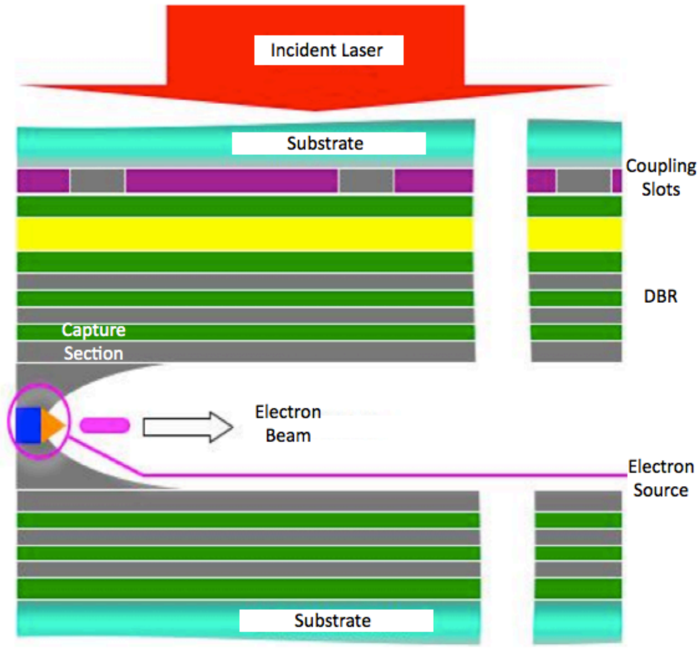

Figure 1.8: A schematic of the Monolithic MAP, designed to produce electrons and accelerate them to 1 MeV or more.

similar to the MAP design is employed. However, since the lower energy electrons travel less distance over one optical cycle, the coupling slot periodicity is adjusted appropriately. There are subtle hurdles with this sub-relativistic scheme that are addressed in the addendum, including generating a resonance adequate for accelerating subrelativistic electrons and maintaining transverse focusing of these electrons. A preliminary design of this monolithic MAP is shown in Figure 1.8.

1.4 Other Dielectric Laser Accelerators

The MAP is but one of many DLA's that have been researched over the last decade. Some of the other DLA designs that have been researched are now described.

1.4.1 Photonic Bandgap Structures

A PBG structure usually consists of a spatially periodic lattice of structural features; examples are the MAP and the design presented in Figure 1.9 (in which the periodicity is in the axial dimension). A cylindrical defect in the center of the lattice in Figure 1.9 serves to confine a mode that can be used to accelerate charged particles traveling through the cylindrical cavity generated by this defect. The geometry of PBG fibers is designed in such a way that this mode is separated in frequency from non-accelerating modes which, as a result of this frequency separation, are not confined within the defect cavity. A common mode that is confined in PBG structures is one in which there is a component of the electric field parallel to the particle direction of travel but no component of the magnetic field in this direction, referred to as a transverse magnetic (TM) mode. Fabrication of, and laser coupling into [19], PBG structures is well established by extensive research in the photonics fiber communications industry and PBG design is well understood [20]. However, transmitting particles through PBGs of significant length remains a challenge, since the aperture size of the defect is typically the size of the source wavelength, 1 micron, in order to maximize the frequency separation between the accelerating TM mode and the non-accelerating higher order modes.

Nevertheless, experimental efforts to observe acceleration in these PBG fibers are ongoing. Researchers at the Stanford Linear Accelerator Center (SLAC) have attempted to excite the TM mode and accelerate electrons with that mode [21], though their efforts have been unsuccessful to date. A diagram of the PBG design that has been tested is given in Figure 1.9.

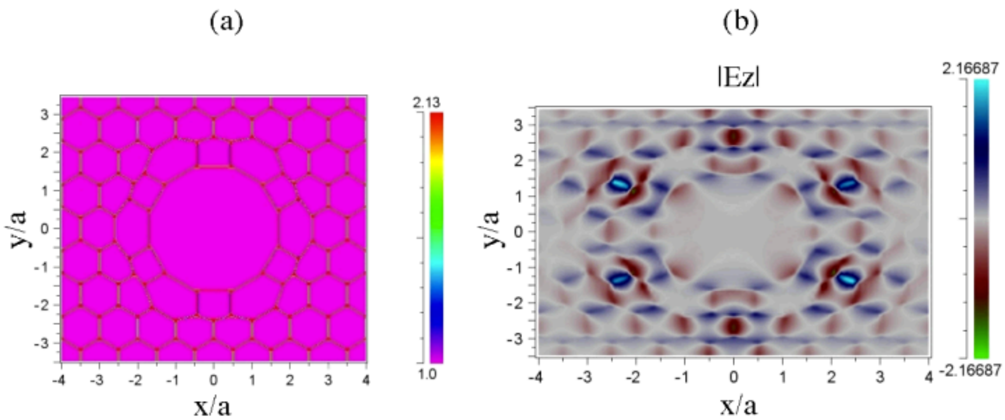

Figure 1.9: a. A image of the design of a Photonic Bandgap Fiber where the horizontal and vertical axes correspond to relative horizontal and vertical displacement respectively. b. A color overlay of the longitudinal component of the electric field in this PBG [21]. This image is taken from Figure 4 of Ref. 21.

1.4.2 The Woodpile

The woodpile is one variant of a PBG structure that has been researched by groups as a waveguide and recently as an accelerator [22]. It is composed of rectangular fused silica rods laid upon each other in a criss-crossing "log cabin" fashion [23]. A small 1 micron tall channel is left unobstructed by fused silica rods in the center of the woodpile. The design is shown below.

This defect creates a band gap that can be used to confine a speed of light accelerating TM mode while allowing non-accelerating modes to leak out of the cavity. How to best couple light into this channel and excite the aforementioned mode is an open question that is still being addressed [24]. Using the waveguide-like properties of the woodpile to couple a TM-accelerating mode into the accelerating defect cavity of the woodpile has proven to be difficult; the defect aperture size must be very small to maximize the frequency separation of the

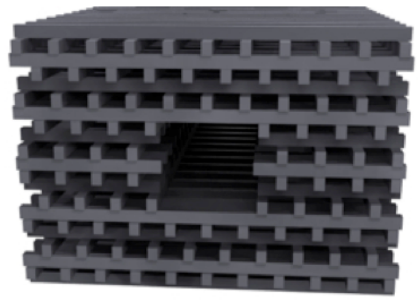

Figure 1.10: The log-cabin style design of the Woodpile PBG Accelerator [23]. This image is taken from Figure 1 of Ref. 23.

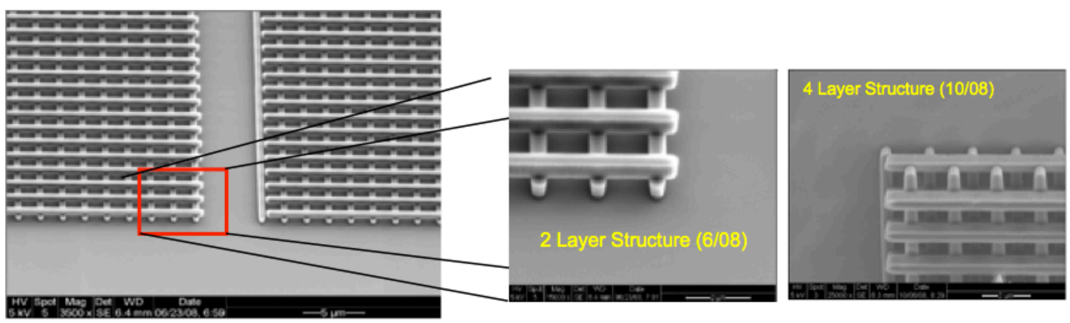

Figure 1.11: An image of the fabricated woodpile structure [23]. This image is taken from Figure 4 of Ref. 23.

TM-mode and other non-accelerating modes, leading to difficulty with transmitting particles through the defect. Nevertheless, if the mode can be successfully coupled into the structure, field gradients in excess of 300 MV/m are expected to be achieved [22].

1.4.3 The Grating Structure

The grating structure, recently tested at SLAC, is a mm-long fused silica DLA that consists of two substrates with "teeth" etched into two opposing faces of the substrates [25]. The substrates are bonded such that there is a micron tall gap in between them in which electrons are injected. The teeth effectively serve as a phase mask that generates a field pattern similar to a standing wave in the gap. Since the temporal period of the laser source matches the time it takes a relativistic electron to travel one spatial period of the accelerating fields, synchronous acceleration occurs for those electrons that see accelerating fields during each optical cycle. A schematic of the grating structure is given in Figure 1.12.

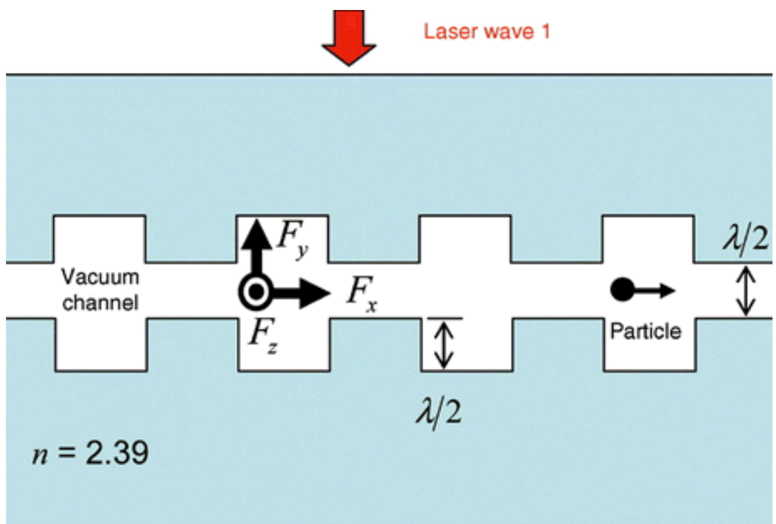

Figure 1.12: The design of the Grating Accelerator. λ is typically 800nm [27]. This image is taken from Figure 1 of Ref. 27.

The grating accelerator benefits from simple energy coupling scheme and an aperture that, although approximately one wavelength tall in one transverse dimension, is effectively infinitely wide in the second transverse dimension. Further, fabrication of the grating involves a straight-forward optical lithography and reactive ion etching process [26]. Unfortunately, the grating is subject to breakdown due to the field enhancement of the laser fields at the corners of the grating teeth. Nevertheless, the grating structure has recently been shown to experimentally accelerate electrons.

1.4.4 Experiments To Date

Recently, researchers at SLAC and UCLA found experimental evidence of acceleration in the grating structure [28]. A 60 MeV beam generated by the Next Linear Collider Test Accelerator (NLCTA) described in Chapter 4 was sent through the grating structure described in section 1.4.3.

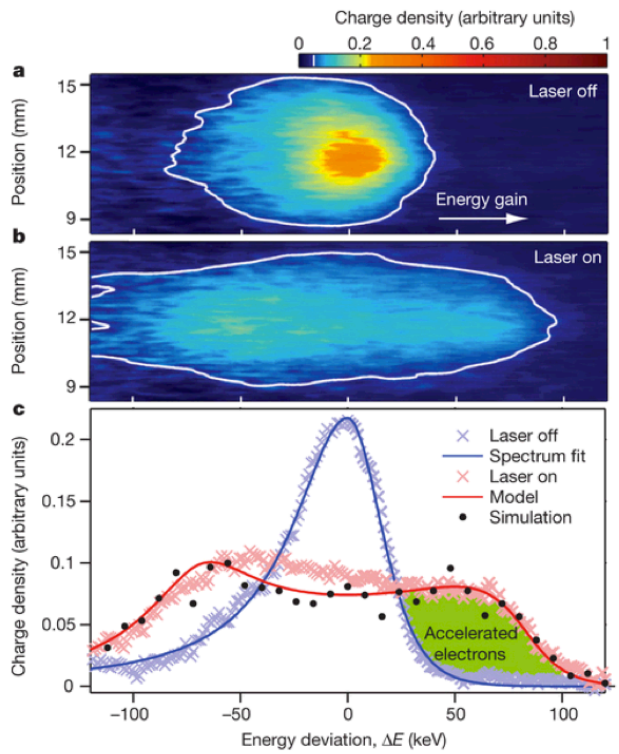

Figure 1.13: Energy Modulation in the Grating [28]. This image is taken from Figure 2 of Ref. 28.

A Ti:Sapphire laser illuminated the grating structure from above and generated an accelerating electromagnetic field mode between the grating teeth. By comparing the energy spectrum of the electron bunches downstream of the structure after the electrons had travelled through the grating with both the laser on and off, energy modulation and ultimately acceleration was observed. A sample energy spectrum for the laser on and off shots is shown in Figure 1.13. Since the experimental methods used in this study are very similar to those used to observe acceleration in the Dielectric Laser Accelerator that is the subject of this dissertation, these methods will be described in chapter 4.

1.5 Applications of the MAP

If the accelerated electrons produced by the MAP strike a high-Z target such as tungsten, they can produce X-Rays via bremsstrahlung. These X-Rays can be used for a wide variety of applications.

1.5.1 Stand-off Nuclear Detection

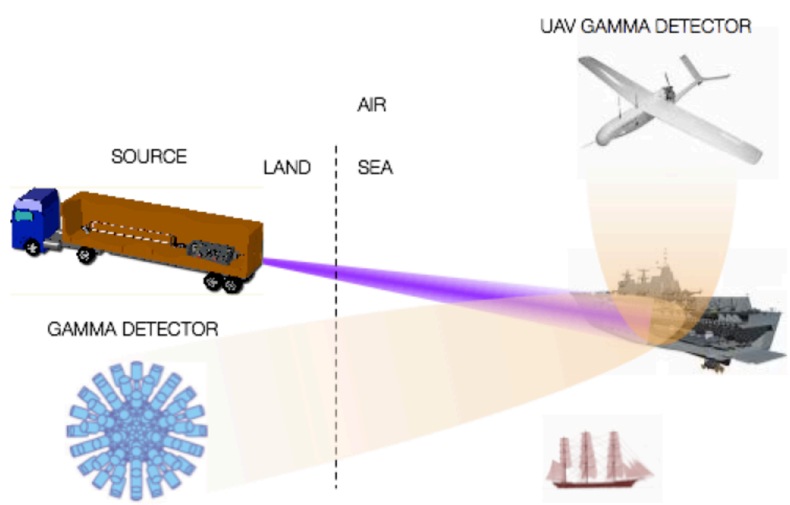

Figure 1.14: An illustration of stand-off nuclear detection. The X-Ray source in this image can be an array of MAPs.

Since many applications require high flux as well as high brightness, an array of MAP devices may be required to achieve the required photon count. However, given the MAP's semiconductor-like fabrication methods, construction of large numbers of MAP modules is feasible and can be very cost-effective. These modules can act as a high-flux portable x-ray source to be aimed at potential sites of nuclear material. If nuclear material exists at the suspected site, characteristic nuclear resonance fluorescence occurs when the nuclei of the material absorbs the x-rays and then emits high energy photons. This reaction can be observed using Gamma detectors (either in the air or on the ground), as illustrated in the Figure 1.14.

1.5.2 Attosecond Time Scale

Since the fields generated in the accelerating regions of dielectric laser accelerators tend to have micron-scale wavelengths, the electron bunches produced by DLAs are naturally hundreds of attoseconds long if the accelerating fields are used to trap the electron bunches. These electron bunches can in turn generate attosecond length x-ray bunches that can then probe many physical phenomena previously unobserved, such as electron cloud dynamics and bubble formation.

For example, an attosecond X-ray bunch train was recently used to ionize Argon atoms [29]. The attosecond bunch train was combined with a colinearly copropagating IR beam and focused into a velocity-map imaging spectrometer where the attosecond train ionized Ar atoms. The resulting photoelectrons were accelerated toward a dual microchannel plate assembly after which they struck a phosphor screen and were imaged by a camera system. The resulting image shows the momenta distribution for the p-orbital of the Ar atom, shown in Figure 1.15.

Attosecond science has only recently begun to blossom as a field of research. The development of DLA's will serve to accelerate its growth.

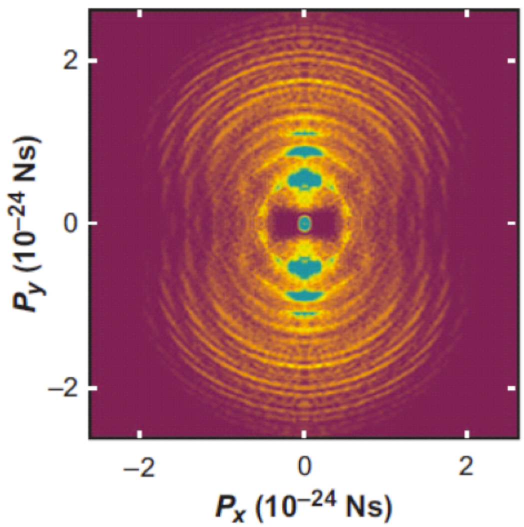

Figure 1.15: The momenta distribution of p-orbital electron in an Argon gas, imaged using an attosecond X-ray bunch train [29]. This image is taken from Figure 3c of Ref. 29.

1.5.3 The MAP for Cancer Therapy

Currently in medicine, high-energy protons, photons, neutrons, and electrons are used to eradicate tumors. Because these particles deposit energy over a very small region when injected into flesh, they have the advantage of being able to damage a cancerous tumor via energy deposition without hurting the surrounding tissue. However, to produce these high energy particles often requires the use of expensive and large accelerators such as cyclotrons. To reduce the cost of particle therapy, one could instead use the MAP as an electron source. The monolithic MAP may produce electrons with an energy on the order of a few MeV and be used as an electron source that can be placed upon surgical equipment. As shown in Figure 1.16, the deposition of energy for electrons in this energy range is on the order of a couple centimeters, so if the surgical device is placed close to the tumor inside the body, a localized and cheaper form of charged particle therapy could occur.

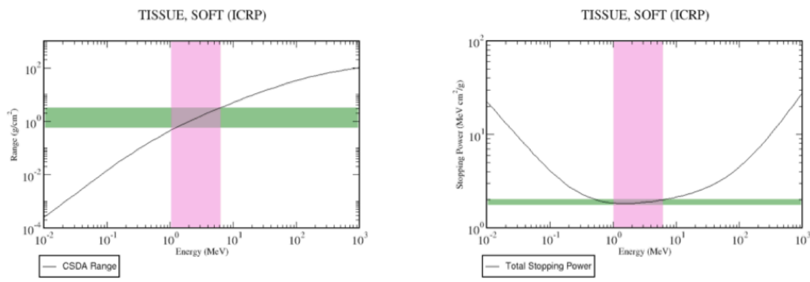

Figure 1.16: The stopping range (left) and power (right) of 1-6 MeV electrons in soft tissue. This image is taken from Ref. 30.

1.6 Thesis

Dielectric Laser Accelerators are an attractive option to achieve compact high gradient accelerators. Fabricating and operating these structures is well within the capabilities of current technology. In this dissertation it will be shown that DLAs, and specifically the Micro-Accelerator Platform, are viable candidates for compact high-gradient acceleration.

CHAPTER 2

Theory

A theoretical analysis of the Micro-Accelerator Platform serves as a starting point for an in-depth understanding of the MAP and its associated numerical and experimental results. In what follows, the fields, forces, resonant conditions and particle dynamics relevant to the MAP will be discussed.

2.1 The MAP as a Resonant Cavity

Acceleration occurs in the MAP as electrons encounter a standing wave resonance in the MAP's vacuum cavity. The fields and forces associated with this resonance are now described.

2.1.1 A Simplified Standing Wave Resonator

The analysis of the standing wave resonance is elucidated if the ideal DLA structure in Figure 2.1 is considered. This structure has only two dielectric layers, one on top of and one on bottom of an accelerating cavity, and a perfect conductor above and below these respective layers.

In comparison with the Micro-Accelerator Platform design, the ideal DLA design reduces the number and complexity of the boundary conditions significantly, rendering the math involved much simpler. Although the fields derived

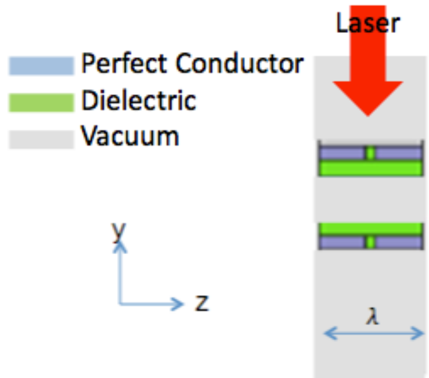

Figure 2.1: A schematic design of one period of a cross-section of the Ideal DLA. The structure is periodic in the z direction and invariant in the x direction (into the page).

in the dielectric layer of the ideal DLA do not match the fields in the DBR of the MAP, the fields that will be derived in the vacuum cavity of this ideal DLA match the standing-wave resonant fields in the vacuum cavity of the MAP [31]. The analysis of the ideal DLA will thus be used as a vehicle to understand the resonant fields in the MAP.

2.1.2 The Resonant Fields

The longitudinal component z of the electric field E in the vacuum cavity of the ideal DLA is a standing wave with a wavelength that matches the periodicity of the coupling slots. Define β_s as the ratio of the coupling periodicity to the incident wavelength of the laser source. Thus, the wave vector component in the z-direction takes the form in Equation 2.1.

$$k_z = \frac{\omega}{\beta_s c}. \tag{2.1}$$

In Equation 2.1, ω is the radial frequency of the resonance and c is the speed of light in vacuum. It is assumed that the resonant fields do not have any dependence on the transverse dimension x (into the page in Figure 2.1). As a result, the component of the wave vector in the x direction, k_x, is equal to 0. The dispersion relationship yields the remaining component of the wave vector, k_y:

$$k_x^2 + k_y^2 + k_z^2 = \frac{\omega^2}{c^2}. \tag{2.2}$$

Combining Equation 2.2 with Equation 2.1 yields

$$k_z = \frac{\omega}{\beta_s c}; \tag{2.3}$$

$$k_x = 0; \tag{2.4}$$

$$k_y = \frac{i\omega}{\gamma_s \beta_s c}. \tag{2.5}$$

Here, $\gamma_s = \frac{1}{\sqrt{1-\beta_s^2}}$. By assumption, the longitudinal component of the electric field takes on the recognizable form of a standing wave in z:

$$E_z = E_0 \cos[k_z z] \cos[\omega t + \varphi_0] f(y). \tag{2.6}$$

In Equation 2.6, E_0 is the amplitude of the standing wave resonance, φ_0 is the initial phase of the resonance and $f(y)$ represents the dependence of E_z on the transverse dimension y. The dependence of E_z on y is found through use of the transverse wave equation:

$$\nabla_\perp^2 E + (\frac{\omega^2}{c^2} - k_z^2)E = 0. \tag{2.7}$$

In Equation 2.7, $\nabla_\perp$ is the transverse gradient. When combined with Equation 2.2, Equation 2.7 simplifies to

$$\frac{\partial^2 E_z}{\partial y^2} + k_y^2 E_z = 0. \tag{2.8}$$

Thus,

$$E_z = E_0 \cos{[k_z z]} \cosh{[\frac{k_z y}{\gamma_s}]} \cos{[\omega t + \varphi_0]}. \tag{2.9}$$

Note that if the structural period of the ideal DLA matches the wavelength of the incident source, then $\beta_s = 1$ and $k_y = 0$ (i.e. $\gamma_s \to \infty$). As a result, the dependence of E_z on the transverse coordinate y vanishes. Electrons traversing the vacuum cavity will encounter the same longitudinal accelerating field regardless of their transverse position.

To proceed further with the analysis, the assumption that the charge passing through the vacuum cavity does not affect the fields in the cavity must be made. In reality, the electrons traversing the standing wave yield two effects. First, they generate wakefields. However, as will be discussed in section 3.3.5, for low bunch charges, it can generally be expected that the wakefields will be modest. Indeed, for an electron bunch charge of 10 fC, these fields are on the order of 10 kV/m, whereas the resonating fields are on the order of 1 GV/m. Second, the electron bunch absorbs energy from the fields as it accelerated to satisfy conservation of energy. However, the electrons gain tens of keV whereas the fields store greater than 1 MeV of energy. Accordingly, these effects may be ignored and $\nabla \cdot E = 0$. With the assumption that $E_x = 0$, E_y can be calculated:

$$E_y = \frac{E_0}{\gamma} \sin{[k_z z]} \sinh{[\frac{k_z y}{\gamma}]} \cos{[\omega t + \varphi_0]}. \tag{2.10}$$

Additionally, using Faraday's Law the following Equations for the magnetic field are obtained:

$$B_x = \frac{i E_0 \beta_s \gamma}{c} \sin{[k_z z]} \sinh{[\frac{k_z y}{\gamma}]} \cos{[\omega t + \varphi_0]}; \tag{2.11}$$

$$B_y = 0; \tag{2.12}$$

$$B_z = 0. \tag{2.13}$$

Note that both B_x and E_y vanish when $\beta_s = 1$.

2.1.3 An Analytical Model

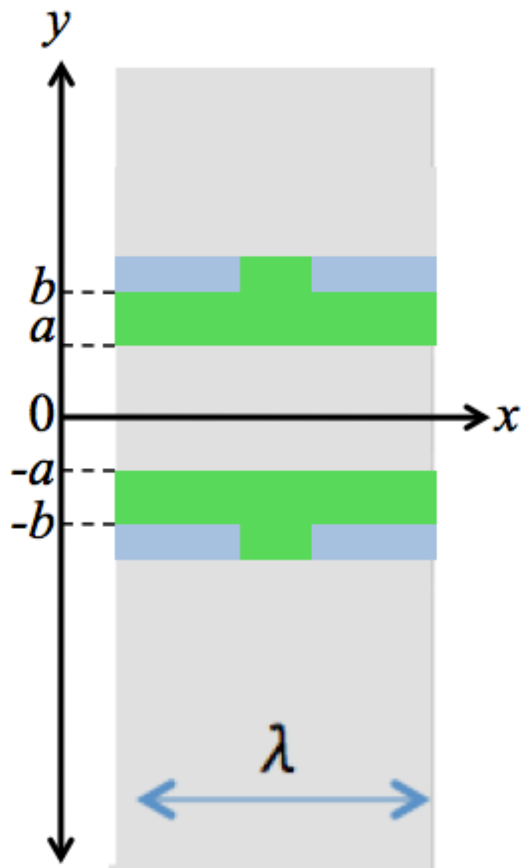

Figure 2.2: A schematic design of a one periods of a cross-section of a simplified MAP, with reference labels for relevant parameters.

The simplified model of the ideal DLA can be used to develop a resonance condition based upon the geometric parameters a and b, defined in Figure 2.2. It is assumed that the electromagnetic fields take on the form derived in Equation 2.6, Equation 2.10, and Equation 2.13. The boundary conditions at the vacuum-dielectric and dielectric-conductor interfaces dictate the frequency of the standing-wave accelerating mode. To apply these boundary conditions, the fields in the dielectric layers need to be solved for first. The solution to the wave equation yields the form of the fields in the dielectric layer:

$$E_z = [A\cos[k_\perp y] + B\sin[k_\perp y]]e^{ik_z z}. \tag{2.14}$$

In Equation 2.14, $k_\perp$ is the transverse wave number in the dielectric, determined by the dispersion relationship in the dielectric (which has a relative dielectric coefficient of ϵ_r):

$$k_\perp^2 + k_z^2 = \frac{\epsilon_r \omega^2}{c^2}; \tag{2.15}$$

$$k_\perp = \sqrt{\epsilon_r - \frac{1}{\beta_s^2}}\frac{\omega}{\beta_s c}. \tag{2.16}$$

The boundary condition at the inner walls ($y = b$) of the perfect conductor ensures that $E_z = 0$ so that

$$A = -B\tan k_\perp b. \tag{2.17}$$

Thus, the longitudinal component of the electric field becomes

$$E_z = -\frac{B\sin[k_\perp(b-y)]}{\cos[k_\perp]}e^{ik_z z}. \tag{2.18}$$

Since $E_x = 0$ and $\nabla \cdot E = 0$ (where $\nabla\cdot$ denotes the divergence) , E_y is determined:

$$E_y = \frac{ik_z B}{k_\perp \cos[k_\perp b]}\cos[k_\perp(b-y)]e^{ik_z z}. \tag{2.19}$$

Continuity of E_z and ϵE_y at $y = a$ dictates that

$$E_0\cosh[\frac{\omega}{\gamma_s \beta_s c}a] = \frac{-B}{\cos[k_\perp b]}\sin[k_\perp(b-a)] \tag{2.20}$$

$$-\gamma_s E_0\sinh[\frac{\omega}{\gamma_s \beta_s c}a] = \frac{\epsilon_r k_z}{k_\perp}\frac{B}{\cos[k_\perp b]}\cos[k_\perp(b-a)]. \tag{2.21}$$

Equation 2.19 and Equation 2.21 can be combined by solving for B in each and setting the solutions for B equal to each other, yielding

$$\frac{\gamma\beta_s}{\epsilon_r}\sqrt{\epsilon_r - \frac{1}{\beta_s^2}} = \coth[\frac{\omega}{\gamma\beta_s c}a]\cot[\sqrt{\epsilon_r - \frac{1}{\beta_s^2}}\frac{\omega}{\beta_s c}(b-a)]. \tag{2.22}$$

This transcendental equation allows one to determine the resonance frequency $\omega$for the standing wave mode resonance in the ideal DLA, given a gap height a, dielectric thickness $(b-a)$ and relative dielectric constant ϵ_r. If the transcendental equation does not have a real solution for a given set of parameters, then a resonance does not exist for those parameters. For instance, if $a = 400$nm, $b = 624$nm and $epsilon_r = 2.19^2$, the resonance frequency, as solved for in Equation 2.22, is 374.7 THz. On the other hand, if $a = 300$nm, $b = 624$nm and $epsilon_r = 2.19^2$, the resonant frequency is 377.2 THz, unsuitable for synchronous acceleration (see section 3.3.7). Moreover, if $a = 400$nm, $b = 624$nm and $epsilon_r = 1.2^2$, a solution to Equation 2.22 does not exist and as a result no standing wave resonance is possible in the ideal DLA with these parameters. Clearly, the existence and frequency of the resonance is dependent on the geometric parameters of the design. Although an analogous transcendental equation has not been found for the MAP, similar conclusions can be drawn for the resonance in the MAP. The frequency of the standing-wave accelerating mode in any design of the MAP depends on the geometric parameters (e.g. layer thicknesses, permittivity of component materials) of that design, as is discussed in section 3.3.7.

2.2 The Dynamics of Acceleration

In order to evaluate particle dynamics in the MAP, the forces that are generated in the vacuum cavity of the MAP must be made explicitly by using the Biot-Savart law in combination with the fields derived in section 2.1.2. In general, the components of the forces experienced by electrons can be solved for as:

$$F_x = q(E_x + c(\beta_y B_z - \beta_z B_y);) \tag{2.23}$$

$$F_y = q(E_y + c(\beta_z B_x - \beta_x B_z)); \tag{2.24}$$

$$F_z = q(E_z + c(\beta_x B_y - \beta_y B_x)). \quad (2.25)$$

Here, β_i corresponds to the i^{th} component of the electron velocity divided by the speed of light and q is the charge of one electron. By using the fields derived in section 2.1.2 and taking the real projections of the resulting expressions, F_z is derived as follows:

$$F_z = q\gamma_s E_0 \cosh[\frac{\omega}{\beta_s c\gamma_s}]Re(e^{ik_z z}) + qc\beta_z E_0 \frac{\beta_s\gamma_s}{c}\sinh[\frac{\omega}{\beta_s c\gamma_s}y]Re(ie^{ik_z z}) \quad (2.26)$$

$$= qE_0[\cosh[\frac{\omega}{\beta_s c\gamma_s}y]\cos[k_z z] + \beta_y\beta_s\gamma_s \sinh[\frac{\omega}{\beta_s c\gamma_s}y]sin[k_z z]] \quad (2.27)$$

$$\approx qE_0(\cosh[\frac{\omega}{\beta_s c\gamma_s}y]\cos[k_z z]). \quad (2.28)$$

The implications of Equation 2.28 are discussed in section 2.2.1. Similarly F_y is calculated:

$$F_y = q\gamma E_0 \sinh[\frac{\omega}{\beta_s c\gamma}y]Re(-ie^{ik_z z}) + qc\beta_z E_0 \frac{\beta_s\gamma_s}{c}\sinh[\frac{\omega}{\beta_s c\gamma}y]Re(e^{ik+zz}). \quad (2.29)$$

In the relativistic regime, $\beta_z \approx c$ and $\beta_y \approx 0$. Therefore F_y can be simplified:

$$F_y \approx qE_0\gamma_s[\sinh[\frac{\omega}{\beta_s c\gamma}y]sin[k_z z] - \beta_s^2 \sinh[\frac{\omega}{\beta_s c\gamma}y]\sin[k_z z]] \quad (2.30)$$

$$= \frac{qE_0}{\gamma_s}\sinh[\frac{\omega}{\beta_s c\gamma_s}y]sin[k_z z]. \quad (2.31)$$

The implications of Equation 2.31 are discussed in section 2.2.2.

2.2.1 Longitudinal Dynamics

Acceleration of an electron due to interaction with the standing wave resonance in the MAP can be approached analytically. For the purposes of this analysis, consider an electron that encounters a maximally accelerating field when on-crest of the standing wave. The longitudinal force experienced by the on-crest electron as a function of time is:

$$F_z(z = ct, y = 0) = qE_0 \cosh[\frac{\omega}{\beta_s c\gamma}0]\sin[k_z\beta_s ct]\sin[\omega t]. \quad (2.32)$$

Since $k_z = \frac{\omega}{\beta_s c}$, the longitudinal force simplifies to:

$$F_z(z = ct, y = 0) = qE_0 \sin^2[\omega t]. \tag{2.33}$$

The average force over one optical cycle is then $\frac{qE_0}{2}$ and the energy gain per period is $\frac{qE_0 \Delta l}{2}$, where $\Delta l = \lambda$. For example, if a 1 GV/m amplitude standing wave with a wavelength of $\lambda = 800nm$ accelerates electrons traversing the MAP, the average energy gain per period of the MAP is 0.4 keV. After traveling through 1mm of the MAP, the on-crest electrons will see a total energy gain of 500 keV, implying an accelerating gradient of 500 MeV/m. Off-crest electrons well encounter either a smaller accelerating force or a decelerating force of equal or smaller amplitude, depending on their phase. For an electron beam that is longer than the wavelength of the resonance, this analysis implies that 50 percent of the beam will gain energy and 50 percent of the bunch will lose energy. For electrons to avoid deceleration, an electron bunch smaller than half of the wavelength of the resonance must be injected into the MAP. In the above example (with a 800 nm wavelength resonance), an electron bunch shorter than 1.5 fs is thus required. More details on the energy evolution of an electron bunch traveling along the MAP's standing wave mode are given in section 3.4.1.

2.2.2 Transverse Dynamics

The Panofsky-Wenzel theorem dictates that any transverse variation of a longitudinal electric field results in a transverse momentum kick imparted to charged particles traversing that field. The electromagnetic fields generated by the MAP's standing wave resonance indeed follow this principle as the transverse variation of Equation 2.6 leads to a transverse defocusing force. In terms of the forces derived in Equation 2.31 and Equation 2.28, the Panofsky-Wenzel theorem is manifested as follows. Since F_z has a cosine dependence on z (Equation 2.28) and F_y has a sine dependence on z (Equation 2.31), it is impossible for an electron to be simultaneously longitudinally stable and transversely focused. For $y > 0$ and $k_z z \in [-\pi/2, \pi/2]$ (i.e. a longitudinally stable phase), $F_y > 0$, indicating a defocusing force.

Fortunately $F_y \propto \frac{1}{\gamma_s}$ so that for a design with a structural period of λ (and thus $\gamma_s = \infty$), the traverse forces vanish. Additonally, in this regime E_z is constant with respect to y, and so the Panofsky-Wenzel theorem implies there is no transverse defocusing. Thus, when the coupling slot periodicity of the MAP matches the wavelength of the incident source ($\beta_s = 1$), the MAP's standing wave resonance does not introduce any defocusing forces. This is supported by simulations that are detailed in section 3.3.4. On the other hand, for designs of the MAP meant to capture and accelerate sub-relativistic electrons (described in the addendum) F_y is the same order of magnitude as F_z and defocusing becomes a non-negligible effect. This is discussed in more detail in the addendum.

2.2.3 An Analytical Model of the Actual MAP

The ideal DLA in Figure 2.1 aided with the analytical approach of diagnosing the MAP's standing wave resonance since there were only a few boundary conditions to deal with in the ideal DLA's analysis. However, such a DLA does not exist at optical frequencies of the incident laser, since there are no perfect conductors in the optical regime. A more realistic design, the MAP, needs to be implemented instead. Although the fields in the vacuum gap of the ideal DLA match those in the MAP, to perform an analysis yielding an analog to Equation 2.22 is difficult. There are many more boundary conditions to consider and no perfect conductor to provide a simple extinction boundary condition to the fields. Mizrahi and Schecter have approached solving this problem analytically by assuming a standing wave resonance in the vacuum gap, and then solving a series of boundary conditions similar to Equation 2.19 and Equation 2.21 combined with a final boundary condition that the electric field is a plane wave above the structure [32]. The solution that Mizrahi and Schachter found is shown as a color overlay in Figure 2.3.

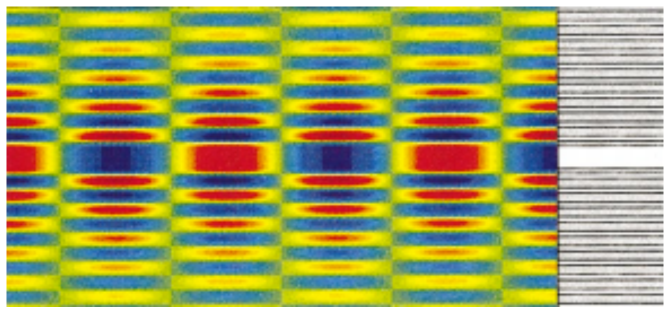

Figure 2.3: A color overlay of the fields solved for in a Bragg Accelerator device by Mizrahi and Schachter. Blue corresponds to positive fields and red negative. The black and white image on the end of the overlay shows the structure, a vacuum gap surrounded by two DBRs. This image is taken from Figure 5 of Ref. 31

However, they did not include phase mask coupling slots, crucial to the MAP design, in their analysis. Simulations, described in section 3.3.7, have shown that the dimensions and materials of the coupling slot layer have a significant impact on the quality and frequency of the MAP's resonance. Incorporating the slots into the Mizrahi's analysis would significantly complicate the boundary conditions. Instead of pursuing solving for the MAP fields analytically, simulations were used as a more direct method of understanding the numerous variations of the MAP that were considered in the design process. These simulations are now described.

CHAPTER 3

Simulations

Simulations of the resonances and particle dynamics in the MAP are necessary to develop the simplified analysis described in Chapter 2 into an actual design. Although issues such as the effect of fabrication errors on the resonance and the effect of space charge on the dynamics of electrons in the MAP are nearly intractable from an analytical standpoint, they can be treated using simulations. After briefly describing the simulation programs most commonly used to analyze the MAP, the numerical results regarding the resonance and particle dynamics of the MAP will be discussed in detail.

3.1 Process Flow

Simulations were used as the main analysis tool to determine a final design of the MAP. A multistep process flow was followed:

1. Consultation with nanofabrication experts leads to determination of a set of structure parameters and materials (see section 3.3.4);

2. HFSS (a frequency-domain EM-solver described in section 3.2.1) is used to characterize and optimize the standing wave resonance in the design decided upon; the resonant frequency is shifted into an acceptable frequency range (See section 3.3.7) by adjusting design parameters.

3. VORPAL (a time-domain EM-solver and PIC-code described in section 3.2.2) is used to characterize the temporal behavior of the resonance as well as the longitudinal and transverse particle dynamics of electrons traversing the resonance;

4. Further consultation with nanofabrication experts, based on the results of steps 2 and 3, leads to potentially repeating steps 1 through 3.

3.2 Tools Used

3.2.1 HFSS

HFSS (High Frequency Structural Simulator) is a high-frequency electromagnetic software that has been frequently used to understand the properties of resonances in the MAP. It uses both a Finite Element Method (FEM) solver and adaptive meshing to generate solutions to Maxwell's Equations in a variety of structures with different boundary conditions. HFSS is not the only EM-solver that operates in this fashion; it was used because it is accurate in modeling the physics of micron-scale electromagnetic structures and commonly used in the DLA community. The model of the MAP serves as a convenient example to illustrate precisely how HFSS arrives at an electromagnetic solution.

In the Figure 3.1, the structure of the MAP model and it's boundary conditions are evident. The associated problem can be summarized as: solve for the electromagnetic fields when a plane wave of a certain frequency is incident upon a series of dielectric layers, taking into account periodic boundary conditions in the z-direction, boundary conditions that ensure that $E_x = H_y = H_z = 0$ on surfaces 1 and 2 (hereafter referred to as the perfect H boundary conditions), and a radiative boundary condition on surface 3 that allows for the electromagnetic

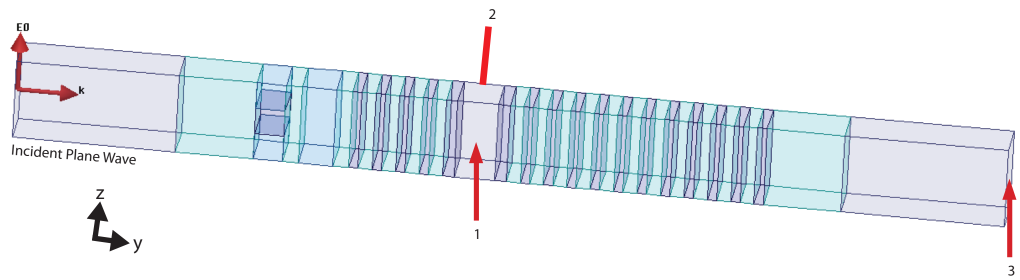

Figure 3.1: The Micro-Accelerator Platform as implemented in HFSS. A plane wave is incident from the top left, surfaces 1 and 2 have perfect magnetic boundary conditions, surface 3 has a radiative boundary condition and the model is periodic in the z direction.

energy of the fields to flow through it. HFSS approaches this problem by first creating a mesh matching both the feature sizes of the model and the wavelength of the incident plane wave, as shown in Figure 3.2.

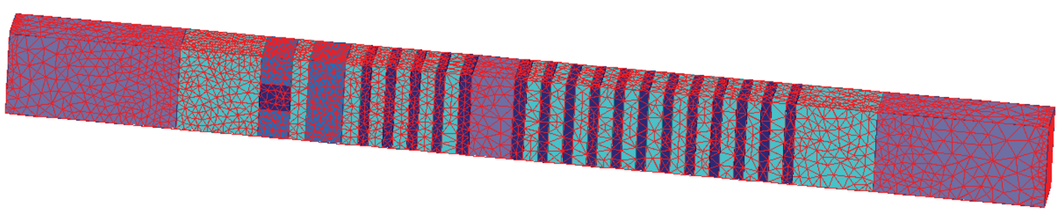

Figure 3.2: The Mesh generated by HFSS when solving for the electromagnetic fields in a typical MAP design.

FEM Element, a commercial Finite Element Method solver, is then used to solve for the electromagnetic fields in each cell. After one such solution is made, HFSS then calculates an error metric based on the variation of the electromagnetic potential from cell to cell. If this metric exceeds a user-defined threshold, the mesh is refined in the regions of highest variation. In the MAP example, these areas of high variation are typically at the dielectric interfaces, especially near the coupling slot closest to the incident plane wave. HFSS will then find a solution using the FEM Element solver once more, compute the error metric again, and refine the mesh as necessary. After multiple passes, the error metric will eventually be less than the threshold and a convergent solution is then reached. In this manner, we have used HFSS to model and optimize many variants of the MAP. This work is detailed in sections 3.2.3 and 3.2.4.

3.2.2 VORPAL

Though HFSS is well-suited for simulating fields in the frequency domain, it is incapable of simulating the MAP in the time domain. For simulations of resonance in the time domain as well as particle dynamics, VORPAL was used. VORPAL, a particle-in-cell (PIC) code combined with a self-consistent electromagnetic field solver, was used as a time-domain simulation tool since it is well-suited to both solve for the EM-fields and the particle dynamics in a micron-scaled dielectric laser accelerator. Similar to HFSS, VORPAL can take a user-specified dielectric design with boundary conditions and solve for the fields involved. Additionally, it can track and characterize particles traveling through these fields as well as the electromagnetic fields generated by those particles.

In the case of the MAP, VORPAL takes into account periodic boundary conditions in the z direction, perfect H boundary conditions in the x-direction and radiative boundary conditions in the y-direction. A laser pulse with a gaussian envelope in time is incident upon the structure from the positive y-direction. Additionally, electrons are passed through the vacuum cavity in the positive z-direction.

To solve for the fields as a function of time, VORPAL takes into account initial conditions of the electromagnetic fields, particle positions and velocities, and a user defined mesh. In each cell of the mesh, the magnetic field on the boundary of the cell is used to update the electric field at the center of each cell over one-half time-step according to Faraday's law. During the next half time-step, the electric field at the center of the cell is used to update the magnetic field on the boundary according to Ampere's law. The particle positions and velocities are then updated using the Biot-Savart law. The new particle positions/velocities are then used to update the electric and magnetic fields.

VORPAL has been used to model and refine many versions of the MAP, taking into account particle dynamics and the temporal response of the structure to laser excitation. These results are detailed in section 3.3.6.

3.2.3 Other Software

A variety of software was used to model other properties of the MAP and its associated experiment. As will be described in the Chapter 4, the MAP was tested at the Next Linear Collider Test Accelerator (NLCTA) at SLAC. To model the various beam-line elements in the NLCTA that would be upstream of the MAP in the experimental setup, the 3-d particle tracking code "elegant" was used. beam-line elements are described by transport elements up to 3rd order. The simulation software "elegant" was used to characterize how the NLCTA beam would interact with the MAP structure as well as the optimal position and strengths of the various magnets in the NLCTA. However, even when the upstream magnets are optimally placed and powered, the electron beam that reaches the MAP is much larger than the acceleration gap in the vertical dimension. As a result, much of the electron beam scatters through the dielectric material of the MAP and the glass substrate on which that dielectric material is deposited. To model this scattering, the Geant4-based code G4beamline was used. After the electron beam's propagation through the beam-line elements of the NLCTA up to the MAP sample has been simulated with "elegant", the momenta and positions of each electron that is the output of the "elegant" simulation is then used as the input of a G4beam-line simulation. G4beam-line is a monte-carlo based beam-line simulation that incorporates many of the well-developed features of the Geant 4 library, particle scattering included. Each electron from the output of the "elegant" simulation is passed through the substrate and scattered probabilistically with its momentum appropriately adjusted. The results of these simulations are described in more detail in section 3.4.2.

3.3 Resonance

3.3.1 Characteristics of a Strong Resonance

In conventional accelerating structures, high-Q resonances are straightforward to quantify (e.g. using the quality factor, fill time, and S-parameters of the structures). In the MAP where moderate-Q resonances (i.e. 10^3) are formed, more qualitative methods are often helpful during initial designs. There are certain properties of the standing-wave resonance in the MAP that are beneficial for achieving efficient acceleration with minimal adverse effects in terms of beam dynamics. An example of a high quality resonance in the MAP is shown in Figure 3.3. The qualities of this resonance that make it ideal include the invariance of E_z with respect to y, the antisymmetry of E_y with respect to y, the high ratio of the maximum longitudinal field in the vacuum cavity to the maximum field in the material of the MAP (hereafter referred to as κ), and the high enhancement factor η (the ratio of the peak E_z to the incident field amplitude). The invariance of E_z with respect to y ensures uniform acceleration/deceleration of the beam,

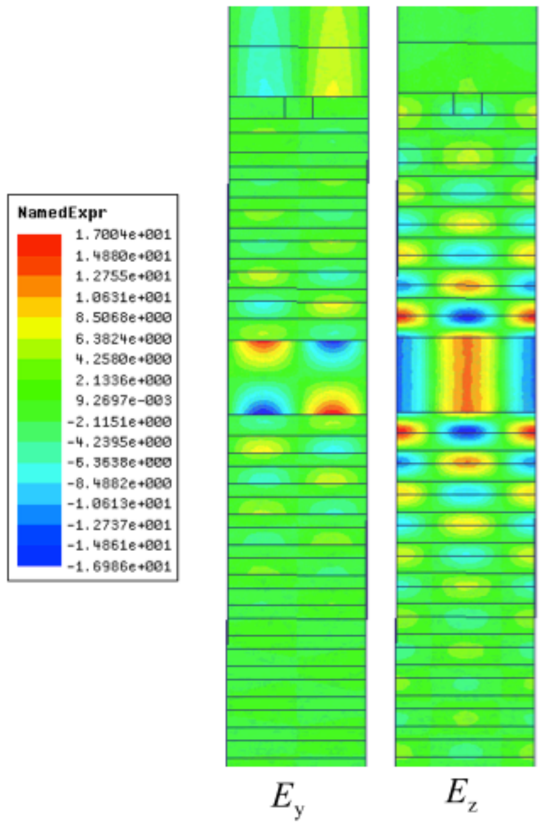

Figure 3.3: The non-zero electric field components of the standing wave resonance in one period of a cross section of the MAP. The incident laser is propagating from the top of the image to the bottom and fields are represented with a color overlay. The amplitude of the legend is relative to the amplitude of the incident field source.

independent of where it entered the vacuum gap. If E_z was not independent of y, then electrons traversing the cavity at different transverse heights would traverse different field strengths, leading to transverse beam instabilities. Given the fact that the electron beams produced in accelerator facilities are typically much larger than the vacuum gap of the MAP, it is therefore very important that E_z is independent of y. The anti-symmetry of E_y with respect to y ensures that the transverse force of Equation 2.31 is symmetric in y so that there are no transverse dynamics that are unaccounted for in the analysis detailed in section 2.2.2. In the experimental setting, optical lasers are well equipped to generate electromagnetic fields that are much stronger than the fields needed to reach the breakdown levels of the materials that compose the MAP. For instance, Fused Silica has a breakdown fluence of 0.8 J/cm^2 in vacuum, yet Ti:Sapphire lasers (described in section 4.2.1.2) are capable of reaching fluences exceeding 10 J/cm^2. To achieve maximum acceleration, one illuminates the MAP with a laser fluence just below the breakdown threshold of the materials composing the MAP's DBR's and coupling slots. A high κ ratio ensures that when the MAP is at this fluence level, the accelerating fields in the vacuum cavity are maximal, yielding the highest accelerating gradient possible. Finally, the large ratio η of peak accelerating field to incident laser field is indicative of optimal energy coupling into the structure as well as high efficiency acceleration. For a given incident laser pulse energy, a maximal η ensures that the largest possible fraction of the incident laser's electromagnetic energy is transferred to the accelerating mode.

3.3.2 Mode Excitation in Dielectrics

When the accelerating mode of the MAP is excited, the fields in the vacuum cavity are not the only fields that are enhanced. The fields in the dielectric materials are enhanced as the mode leaks into the DBR and coupling slots. As a result, any change in the geometry of the DBR or coupling slots changes the quality and frequency of the accelerating mode. To accurately model the experimental implementation of the MAP, discussed in section 4.1, substrates are placed immediately above the coupling slots of the MAP and below the bottom DBR of the MAP in it's HFSS model. However, the resonating mode leaks into the substrate in the same manner as it leaks into the DBR and as a result, the thickness of the substrate affects the resonant frequency. For the MAP design in Table 3.4, the resonant frequency as a function of substrate thickness is given in Figure 3.4.

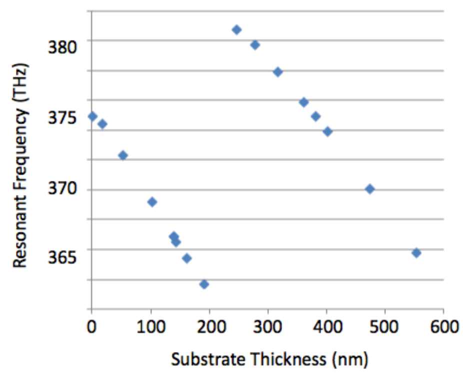

Figure 3.4: The resonant frequency of a MAP design as a function of substrate thickness

The resonant frequency's dependence on the substrate thickness takes on the profile of a sawtooth pattern with a periodicity of 380 nm (when the longitudinal periodicity of the MAP is 800 nm as it is in the simulations that generated the data in Figure 3.4). Visual inspection of the fields excited in the substrate in Figure 3.5 shows that the transverse nodes of the accelerating mode E_z field pattern are spaced 380 nm apart. From Figure 3.4, it is then apparent the resonant frequency shifts so that the substrate terminates on a node of the field pattern.

In the MAP experiment, the substrate is 500 microns thick and should not be treated as a thin film layer as it is in the HFSS models discussed in this section. However, because of the small feature sizes in the MAP, simulating a 500 micron thick substrate and the massive mesh entailed would require computational resources unavailable to the MAP project. As a result, the substrate is

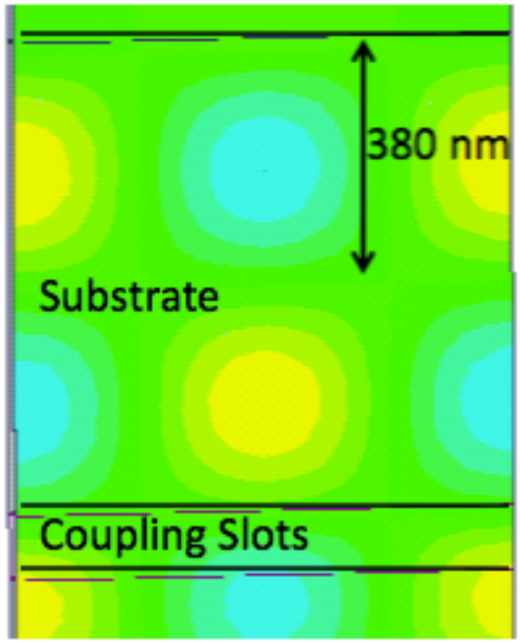

Figure 3.5: E_z in the substrate of the MAP model when the accelerating mode is excited. The node to node distance is 380nm.

left in the model (to allow for the simulation of the diffraction of light at the substrate/coupling slot interface) at a thickness that does not alter the resonant frequency (i.e. a multiple of 380nm). It is assumed that a 500 micron substrate would not affect the resonant frequency in the same way that a thin film substrate does in numerical simulations. In simulations, energy losses in the dielectrics are also ignored. Fused silica and similar dielectrics have loss tangents on the order of 10^{-12}. When these loss tangents were included in the model of the MAP simulated in HFSS, the quality and frequency of the resonance was not altered, although the simulation time increased by a factor of 10. As a result, to reach numerical results in a timely fashion, losses were not included in most of the simulations.

3.3.3 Three-D Field Variation

Recall from section 3.3.1 that a variation in the standing wave accelerating mode E_z with respect to the transverse coordinate y leads to a nonuniform acceleration of an electron beam traversing the MAP cavity. Electrons traveling off-axis will be accelerated/decelerated with a different field gradient than those traveling on-axis. The same logic applies to the transverse coordinate x. If the E_z varies with respect to x, the energy modulation an electron undergoes will depend on it's horizontal location within the electron bunch, potentially leading to beam instability.

The simulations that generated the resonance displayed in Figure 3.3 do not account for the potential issue of E_z dependence on x since the "perfect-H" boundary conditions of those simulations ensured that $E_x = 0$, $H_y = 0$ and $H_z = 0$. The combination of these null fields with Farday's Law ensures that $\frac{dE_z}{dx} = \frac{dE_y}{dx} = 0$.

To account for a potential variation in E_z with respect to x, a model was built in HFSS with radiative boundary conditions replacing the perfect H boundary conditions in Figure 3.1. Furthermore, the edge of the MAP is introduced in x as is shown in Figure 3.6. The resonating standing wave solved for in this model indeed has a variation depending on x, as is shown in Figure 3.7. Sufficiently far from the x-edge of the structure (12 microns in Figure 3.7), the variation in E_z reduces to less than 10 percent of its average value.

As the size of the model grows, one expects that the fraction of the MAP with low E_z variation with respect to x will grow, while the size of the region in which E_z shows variation due to edge effects will remain the same size. This was confirmed by a series of simulations varying the size of the model in x up to 70 microns, the results of which are given in Table 3.1. In Table 3.1, L_x refers to

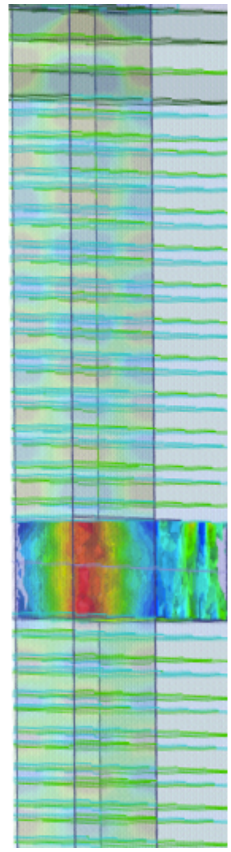

Figure 3.6: A cross-section color overlay of E_z in a fully 3-dimensional MAP model in HFSS. Note the variation of E_z with respect to x (into the page) as a result of edge reflections.

the length of the model in x and l_x refers to the size of the region in which E_z varies by less than 10 percent.

In reality the size of the MAP in x exceeds 1 mm (see section 4.1.1.3). However, a model of this size cannot be simulated, since mesh features are typically 10 nm in the HFSS MAP models. Creating a model of the MAP that is hundreds of microns large in the x dimension would thus require a total number of mesh edges exceeding 10 million, requiring more computational resources than are available even on desktop computers with over 100 GB of RAM. Nevertheless, the results

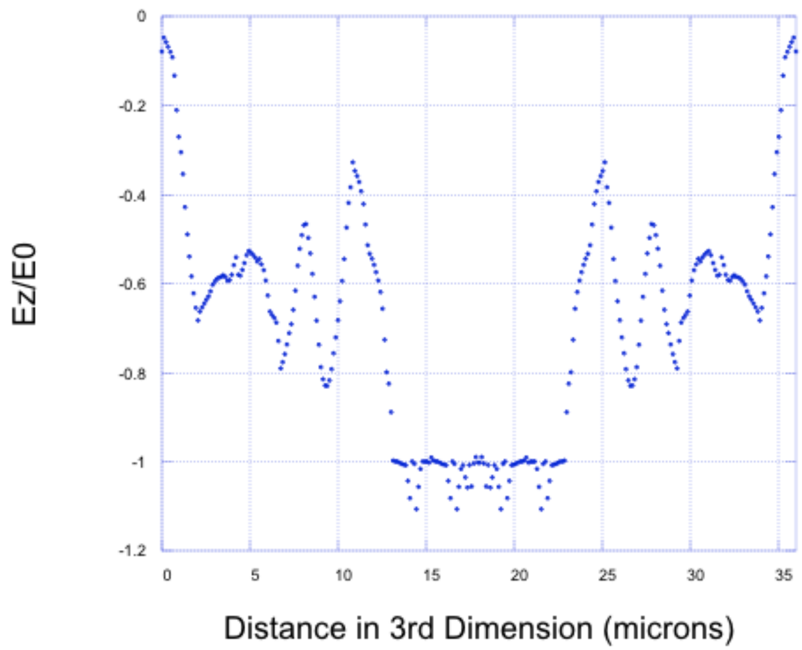

Figure 3.7: E_z as a function of x in a MAP model that incorporates edges in x. Twelve microns away from the edge, the variation of E_z reduces to less than 10 percent. The ripples in E_z near the edge of the structure are due to the impedance mismatch at the edge.

shown in Table 3.1 indicate that one can expect the fields approximately microns away from the edge of the structures to exhibit minimal dependence on x.

3.3.4 Designs Considered

A large number of combinations of realistic dielectric materials have been modeled in the simulation software HFSS. The indices of refraction of these materials have been selected so as to reflect the characteristics measured in the fabrication lab at UCLA (see section 4.1.2). Strong resonances (as defined in section 3.3.1) have been found for those combinations of dielectrics that exhibit a large contrast in

Table 3.1: Varying the Size of the MAP in x.

L_x **(microns)**	l_x **(microns)**
5	0
20	2
30	6
35	11
40	15
50	28
60	37

their respective indices of refraction.

Using a set of high-contrast (in index of refraction) dielectric materials provides a few advantages for generating a high quality resonance. First, if the material in the coupling slot has a significantly higher index of refraction than the surrounding material, the electric field of the incident laser will be "drawn into" the higher index material, leading to strong diffraction and hence better coupling into the longitudinally varying accelerating mode. Second, if the two materials in the DBRs have high contrast in their indices of refraction, then the DBR is more effective in confining the accelerating mode in the vacuum gap. The net effect of this optimized coupling and confinement is a resonance with a large enhancement factor η and κ ratio.

The combinations of dielectrics considered generally include one oxide with a high dielectric constant, one oxide with a low dielectric constant, and one oxide with an intermediate dielectric constant. Additionally, a large bandgap energy (¿5 eV) was necessary in the constituent materials, as a high band gap energy results in a large damage damage threshold. Table 3.2 lists the relevant proper-

Table 3.2: Properties of Materials Considered for the MAP Design.

Material	Index of Refraction at 800 nm	Bandgap Energy (eV)
hafnia	1.89	5.7
zirconia	2.19	5.0
fused silica	1.45	8.9
magnesium fluoride	1.38	10.8
sapphire	1.76	2.6

ties for many of the materials considered. Though fluorides and arsenides were included in designs that provided strong resonances, they were eventually ruled out as candidates due to fabrication impracticality. Dielectrics like magnesium fluoride, though attractive due to its low index of refraction, cannot be deposited in most machines, as the fluoride contaminates sputtering and evaporating machines, rendering them unusable for other materials. The final set of materials that were used in the design of the MAP were zirconia, fused silica, and hafnia. The lower contrast in the dielectric permittivity of the materials used was partially compensated for by adding dielectric pairs to the DBR's. Although this compensated for the reflective ability of the DBR's, it did not compensate for the reduced diffractive capabilities of the coupling slots. This is reflected in the quality of the resonance (see section 3.3.1).

In addition to setting limits on the materials used in the MAP design, the fabrication process also set limits to the layer thicknesses and widths in the design. The slot lithography methodology described in chapter 4 limits the width of the coupling slot to be more than 270 nm, thus limiting the diffractive capabilities of the coupling slot. Depending on the parameters of layer deposition, the index of refraction of each material in the MAP can deviate from the values found in

Table 3.3: Material Combinations Used in Designs.

Material	η	κ	**Comments**
hafnia, zirconia, magnesium fluoride	12.0	0.8	fluorides impractical
sapphire, zirconia, magnesium fluoride	8.1	0.7	fluorides impractical
hafnia, zirconia, silica	6.0	0.6	Practical materials
sapphire, zirconia, silica	7.2	0.65	Sapphire is birefringent

literature. As a result, an iterative process in which simulation designs were modified due to fabrication requirements and new designs were sent to the fabrication team repeated itself throughout the development period of the MAP. The final set of design parameters that both met fabrication capabilities and optimized the quality of the standing wave resonance in the MAP are given in Table 3.4.

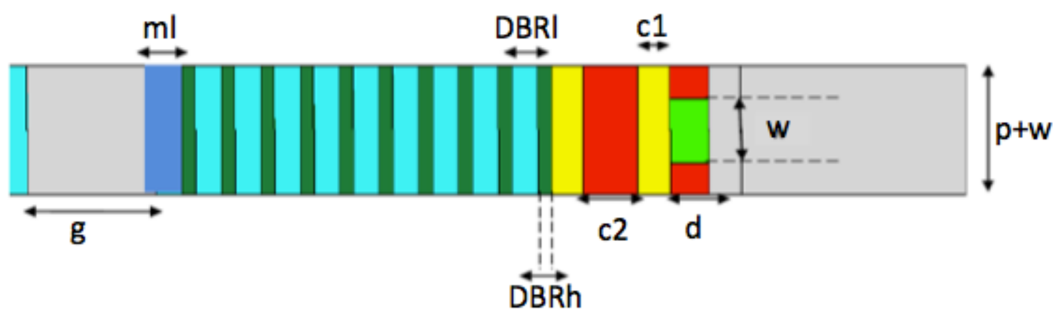

Figure 3.8: Legend with the geometric parameters labelled for reference.

3.3.5 Spectral Characterization

To confirm that the MAP successfully excites a resonance, the standing wave resonance needs to be experimentally observed. The transmitted and reflected spectra of the MAP can be used to make this observation. When the MAP is illuminated with plane waves at different frequencies, the transmitted and

Table 3.4: The MAP Design Materials and Parameters.

Parameter	**Material**	**Thickness**
g	vacuum	400nm
ml	hafnia	112nm
DBRl	fused silica	14nm
DBRh	hafnia	104nm
c1	fused silica	155nm
c2	hafnia	340nm
d	hafnia	290nm
w	zirconia	400nm
p	hafnia/zirconia	800nm

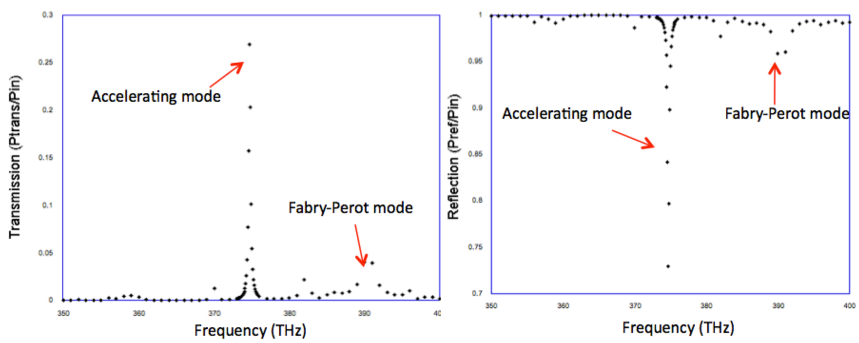

Figure 3.9: The transmittance/reflectance of the MAP as a function of frequency on the left/right. Ptrans refers to the transmitted power, Pref the reflected power and Pin the incident power. Each plot point represents a separate simulation; the point density is higher near the central resonance

reflected intensity of light depends strongly on whether a resonance is excited in the structure. If the accelerating mode is excited then less of the incident plane wave intensity is transmitted and more is reflected. Sharp features in reflected and transmitted spectra indicate the presence of this resonance. The transmitted and reflected spectra, resulting from HFSS simulations of the MAP, are given in Figure 3.9. The sharp dip (peak) on the left (right) in Figure 3.9 corresponds to the accelerating mode shown in Figure 3.3. However, there are other modes excited in the MAP at nearby frequencies, as is evidenced by the nearby features in Figure 3.9.

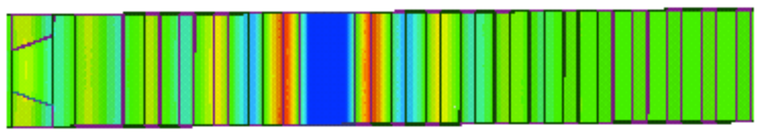

Figure 3.10: A color overlay of E_z for a Fabry-Perot Mode of the MAP. The incident plane wave travels from the left to the right. The invariance of E_z with respect to z makes this mode non-accelerating.

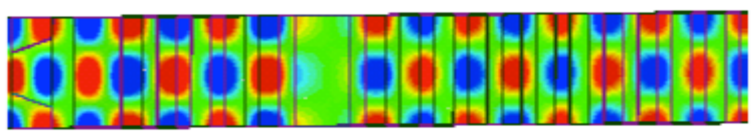

Figure 3.11: A color overlay of E_z for an anti-symmetric mode excited in the MAP. The incident plane wave travels from the left to the right. E_z is zero on axis and thus incapable of accelerating charged particles.

Fabry-Perot modes as well as modes that are antisymmetric in E_z about the $y = 0$ axis are often excited in the MAP and examples are shown in Figure 3.10 and Figure 3.11. Being a resonant cavity, it is expected that when illuminated, the MAP will have modes other than the accelerating mode excited. Preventing these non-accelerating modes from interfering with acceleration, however, is crucial. Fortunately, the bandwidth of an optical laser is often much smaller than the frequency separation of the accelerating mode and nearby non-accelerating modes. As will be discussed in section 4.2.1.2, the bandwidth of the Ti:Sapphire used to excite the MAP is less than 0.2 THz, much smaller than the separation of the accelerating mode from the nearest non-accelerating mode in Figure 3.9, 5 THz.

It is also worth noting that, in contrast with typical RF accelerators, the reflectance (transmission) at the resonance frequency is unusually high (low) [33], a consequence of the design of the MAP. The partially transmissive coupling slots combined with the reflective DBR on the incident (top) half of the MAP design lead to unusually high reflection (and low transmission) of incident light, even when the accelerating mode is excited. This is also reflected in a unusually low quality factor, which will be discussed in section 3.3.6.2.

3.3.6 Temporal Characteristics of the Resonance

3.3.6.1 Benchmarking the Resonance

To confirm the validity of the HFSS simulation results, the time-based Electromagnetic Field Solver and particle-in-cell (PIC) code VORPAL (described in section 3.2.2) was used to model the MAP design based on the parameters in Table 3.4. Unlike HFSS, a frequency domain code that finds a steady state electromagnetic solution, VORPAL is a time-based code that incorporates excitation sources with a finite temporal extent. Instead of illuminating a model of the MAP with a plane wave, VORAL can illuminate the MAP with a pulse that more closely resembles that which an optical laser can generate, a sine wave with a gaussian envelope, shown in Figure 3.12.

To compare the simulated electromagnetic fields in VORPAL with those in HFSS, the enhancement factor η and the κ ratio. These values are measured in

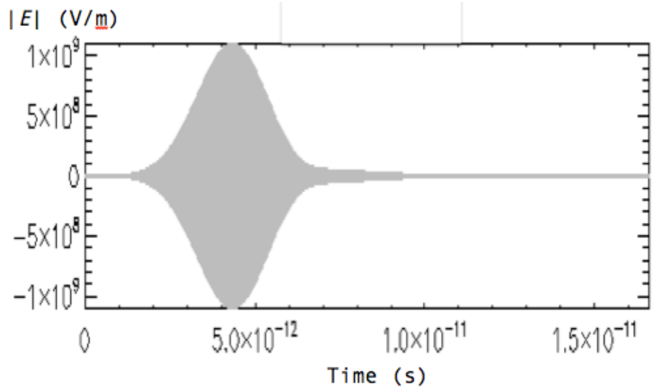

Figure 3.12: The incident source in the VORPAL time-based simulations of the MAP. It is a sine wave with a near-infrared central wavelength and a gaussian envelope.

Table 3.5: Comparing the MAP in HFSS and VORPAL.

Model	η	κ
HFSS	6.0	0.6
VORPAL	5.7	0.6

the VORPAL simulation after the incident source has filled the vacuum cavity with the accelerating mode. More precisely, η and κ are measured once the accelerating fields in the vacuum cavity have reached maximum amplitude. The amount of time it takes the fields to reach their maximum values is the fill time of the structure and is discussed in more detail in section 3.3.5.2.

Table 3.5 shows close agreement between the frequency and time-domain solutions of the model of the MAP detailed in Table 3.4. The difference in enhancement factor (3.3 percent) can be explained by the difference between the finite difference time domain solver of VORPAL and the finite element method solver of HFSS [34].

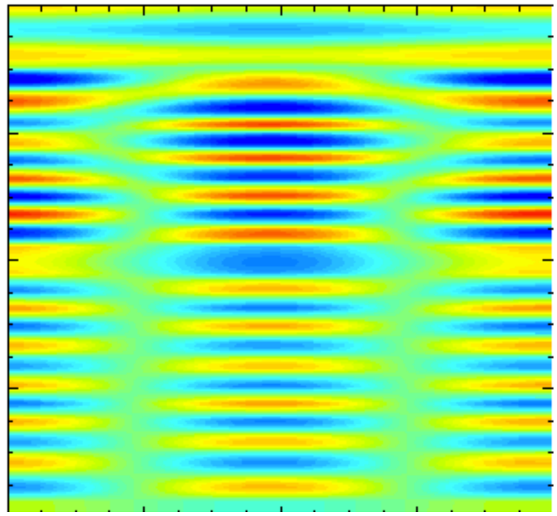

Figure 3.13: A color overlay of the longitudinal component of the electric field in the standing wave accelerating mode in the MAP, as simulated in VORPAL The field is shown after the cavity has been illuminated by a incident laser for 5 ps (the fill time of the structure). Red corresponds to accelerating fields and blue to decelerating fields.

3.3.6.2 Fill Time

The fill time of the cavity can be measured computationally by exciting the accelerating mode with an incident electromagnetic source, abruptly turning the source off and then monitoring the decay of the resonating mode's amplitude.

Specifically, the fill time can be calculated from Figure 3.14 by determining the time it takes the energy stored in the cavity (E^2) to decay to $\frac{E^2}{e}$ after the source has been terminated. In the above field history, this corresponds to 5.1 picoseconds. As an aside, note that the quality factor of the accelerator can be defined as the number of resonant cycles that pass during the fill time of the structure. For this model of the MAP, the quality factor is therefore 1900.

The fill time of the structure is independently calculated by exciting the accel-

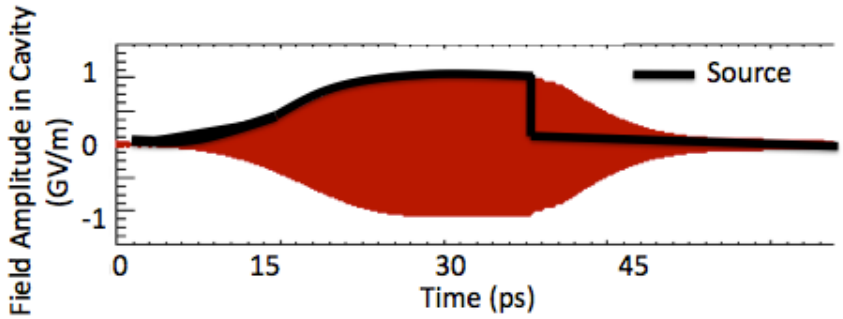

Figure 3.14: The amplitude of the longitudinal component of the standing wave accelerating mode in the vacuum gap of the MAP as a function of time. The incident source, indicated by the black line, is abruptly terminated at a time of 36 ps.

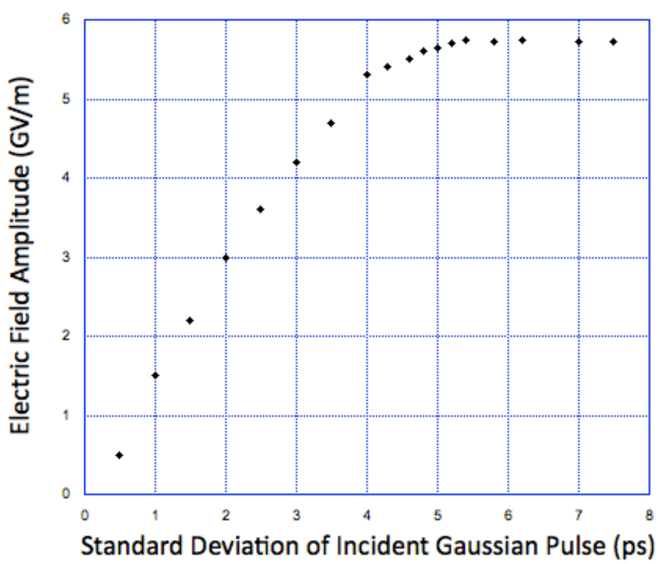

Figure 3.15: The field amplitude in the vacuum cavity of the MAP as a function of the standard deviation of the gaussian envelope of the incident source. The peak amplitude of the incident source is 1 GV/m.

erating mode of the MAP with a set of gaussian excitations (such as that shown in Figure 3.12) with varying temporal widths. When the standard deviation of the gaussian envelope is less than the fill time, the amplitude of the accelerating mode will be less than maximal, but when the standard deviation of the gaussian envelope exceeds the fill time, the amplitude of the accelerating mode will reach its maximum value. Increasing the width of the incident pulse beyond the fill time should not further increase the field amplitude beyond its maximum value. The result of this set of simulations is shown in Figure 3.15. For gaussian standard deviations exceeding 5 ps, the field amplitude plateaus at 5.72 GV/m, consistent with a fill time of 5 ps and an enhancement factor η of 5.72 (see Table 3.5).

3.3.7 Error Tolerance

Once the structure parameters that provide for a strong resonance have been found for a given set of dielectric materials, it is necessary to determine how far the fabricated MAP can vary from this set of parameters and still provide a resonance that can accelerate electrons. Two factors affect how efficiently the resonating mode of the MAP can accelerate electrons: the quality of the resonance and the frequency of the resonance. To monitor the effect of structural errors on the quality of the resonance, each parameter of the MAP is varied from its optimal value (while maintaining all other parameters at their optimal values) until the E_z field overlay is visibly distorted. Though this is a qualitative approach, it has proven fairly consistent among the different models of the MAP that have been simulated. The error tolerances for each layer (labeled according to the legend in Figure 3.8) are given in the following table.

Additionally, if the resonant frequency does not match $\frac{c}{\lambda_s}$, synchronous acceleration does not occur. In this case, the distance that a relativistic electron

Table 3.6: Error Tolerances for Resonant Quality.

Parameter	**Error Tolerance (percent of nominal value)**	Absolute Tolerance
g	15	60 nm
ml	5	6 nm
DBRl	10	14 nm
DBRh	10	10 nm
c1	5	8 nm
c2	12	34 nm
d	10	25 nm
w	18	50 nm
λ_s	8	64 nm
n_{silica}	3	0.04
n_{hafnia}	3	0.05
$n_{zirconia}$	8	0.17

Table 3.7: Error Tolerances for Resonant Frequency.

Parameter	**Error Tolerance (percent of nominal value)**	Absolute Tolerance
g	15	60 nm
ml	4	5 nm
DBRl	1	1 nm
DBRh	1	1 nm
c1	2	3 nm
c2	3	8 nm
d	4	11 nm
w	10	27 nm
n_{silica}	1	.01
n_{hafnia}	1	.02
$n_{zirconia}$	3	.07

travels during one cycle of the resonating fields does not match the wavelength of the resonance. As a result, the phase of the standing wave that the electron encounters at the beginning of each resonant cycle changes linearly with time. To accrue at least 50 keV of energy gain over 1mm of travel (and thus have an detectable energy gain), the resonant frequency must be within a 0.5 THz (0.13 %) range about $\frac{c}{\lambda_s}$. A parameter scan of the different layer thicknesses and refractive indices then yields a much stricter tolerance than what a consideration of only resonant quality provides.

3.4 Acceleration and Dynamics in the Relativistic Design

3.4.1 Acceleration due to Standing Wave Resonance

The standing wave resonance in the MAP imparts energy to electrons via synchronous acceleration. VORPAL is used to confirm that synchronous acceleration occurs in the MAP via simulations. The MAP design described in Table 3.4 is illuminated by a gaussian-enveloped laser pulse with a standard deviation equal to the fill time of the structure, calculated in section 3.3.6.2. Once the vacuum cavity is filled with the accelerating mode and the amplitude of the accelerating mode is maximal, an electron bunch with an initial energy of 60 MeV that fills the cavity in the y-dimension (to match experimental parameters detailed in Table 4.4) is injected at an accelerating phase of the standing wave resonance. The length of this bunch is 1/40th of the wavelength of the standing wave to ensure that no part of the bunch sees decelerating phases. The electron energy is monitored while the electrons travel for 1mm along the accelerating mode of the MAP. The result of this simulation is given in Figure 3.16.

Electrons gain 1 MeV of energy after traversing the cavity for 1 mm (indicating a 1 GeV/m accelerating gradient). The accelerating mode peak amplitude in the simulation is 2 GV/m. The analysis of longitudinal dynamics in section 2.2.1 indicates that for a 2 GV/m peak field gradient, the accelerating gradient should indeed be 1 GeV/m. Thus, this VORPAL simulation confirms that the MAP's accelerating mode effectively accelerates electrons in the manner described in sections 1.1.2 and 2.2.1.

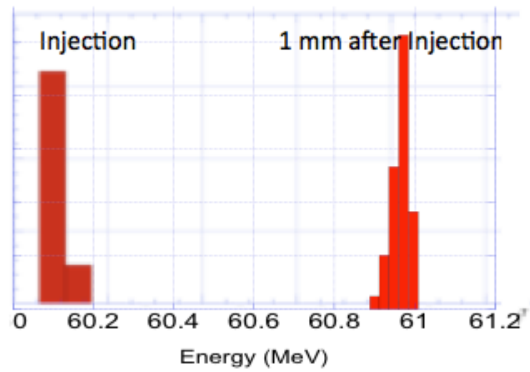

Figure 3.16: The energy profile of an electron bunch at injection (injected at 60 MeV) and 1mm after injection. The maximum field gradient in the accelerating cavity is 2 GV/m. The energy profile broadens slightly due to different electrons in the bunch encountering different amplitude fields. The electron bunch length is 1/40th the length of the wavelength of the accelerating mode in the MAP.

3.4.2 The Expected Accelerated Signal

The electron beam used to test the MAP is significantly larger than the vacuum channel and longer than the wavelength of the standing wave resonance (see Table 4.4). As a result, two physical phenomena account for the energy spectrum of the beam downstream of the MAP structure: coulomb scattering of those electrons that traveled through the MAP's substrates and dielectric layers (described in section 4.1) and the energy modulation of those electrons that traverse vacuum channel after it has been filled with the accelerating mode. G4beamline and "elegant" were used to model the former and VORPAL the latter.

The software "elegant" was used to model the electron beams trajectory through the beam-line that is used to experimentally test the MAP. Once the electron beam reaches the MAP's location along the beam-line, the electrons' momenta and positions as simulated by "elegant" are used as the initial param-

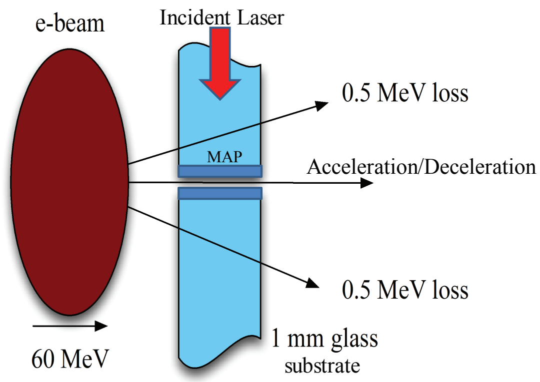

Figure 3.17: Illustration demonstrating the means of energy modulation as the NLCTA electron beam travels through the MAP.

eters in a separate G4beamline simulation. The scattering model in G4beamline includes two flat glass substrates separated by a vacuum channel with the same height of the vacuum cavity in the MAP, effectively mimicking the MAP. Note that even though the different dielectric materials that normally compose the MAP are not included in the G4beamline simulation, their radiative distances are similar to that of Fused Silica and thus the model accurately reflects the electrons' energy losses due to scattering within the dielectric layers. An energy profile of the electron beam is taken downstream of the substrates and is shown in Figure 3.18.

The larger, lower energy peak on the left of the spectrum in Figure 3.18 corresponds to those electrons that lost energy due to scattering through the substrates (hereafter referred to as the "straggled distribution"). The second smaller peak corresponds to the electrons that passed through the MAP vacuum channel without losing energy due to scattering within the glass (hereafter referred to as the "transmitted population").

Fig 3.19 shows the resulting energy distribution (and Figure 3.20 the energy

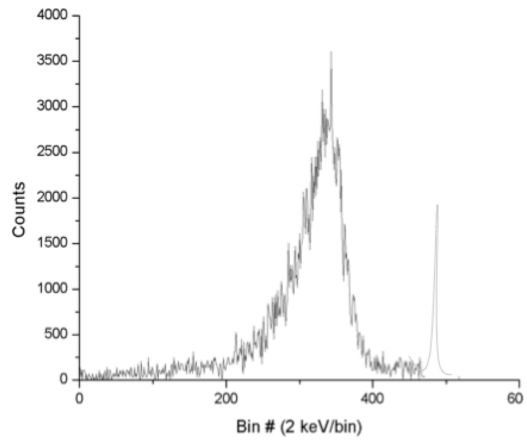

Figure 3.18: Energy distribution of electron bunch after having traveled through the MAP in G4beam-line. The initial energy distribution matches the initial energy distribution of Figure 3.16.

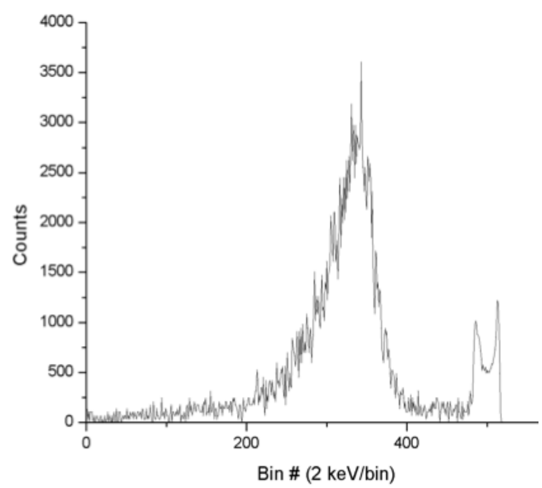

Figure 3.19: Energy distribution of electron bunch after having traveled through the MAP in with a 0.4 GV/m accelerating mode excited (a field amplitude chosen to reflect modest experimental goals). The zeroth bin corresponds to 59 MeV and the bin size is 2 keV/bin.

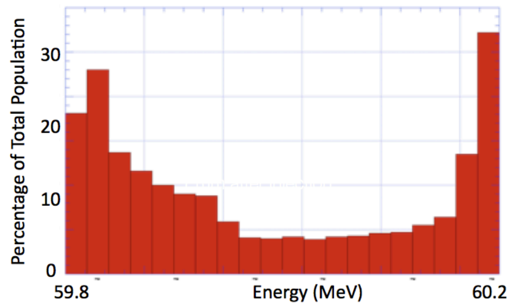

Figure 3.20: Energy distribution of the transmitted electron bunch after having traveled through the MAP in with a 0.4 GV/m accelerating mode excited. The vertical axis shows the percentage of the electron bunch with a certain energy relative to the total transmitted population.

distribution of only the transmitted population) when the transmitted peak is sent through the MAP with the accelerating mode excited.

In order to model the interaction of the electrons with the electromagnetic fields within the vacuum gap, the distribution of the second peak is sent through model of the MAP in VORPAL with both the laser on and the laser off. Since the electron beam used in the MAP (see Table 4.4 experiment is larger than the wavelength of the standing wave, some electrons will be decelerated due to entering the MAP's cavity at a decelerating phase of the mode. As a result, the energy profile of the electrons that traverse the vacuum cavity widens, with some electrons being accelerated and others decelerated. More specifically, the energy profile exhibits a 'double-horned' shape centered around the injection energy, 60 MeV. Figure 3.19 exhibits a 200 keV energy gain, consistent with the 400 MV/m accelerating mode excited in the vacuum cavity.

3.4.3 Phase Stability

For synchronous acceleration to occur, the phase of the standing wave that an electron interacts with every optical cycle must remain the same. If the electron slips in phase as it traverses the vacuum cavity of the MAP, it will eventually lose energy due to encountering decelerating fields, even if the electron were injected at an accelerating phase. To monitor whether phase slippage occurs for electrons propagating along the standing wave accelerating mode of the MAP, two models were created and then compared. In the first, a particle pusher code made in Mathematica simulates the propagation and energy modulation of a single electron traveling along the ideal resonant fields in Equation 2.28 and Equation 2.31. In this code, no potential sources of phase slippage(space charge, wakefield effects, etc.) are included. In the second model, VORPAL is used to monitor the energy of an electron bunch as it traverses the vacuum cavity of the MAP as described in section 3.4.1. Note that VORPAL includes all of the effects that may lead to phase slippage. Figure 3.21 shows the results of both models, Mathematica and VORPAL. The agreement of the energy versus injection phase between these models indicates that phase slippage is not a concern for the resonant accelerating mode in the MAP (note that the resonant frequency in both models is $\frac{c}{\lambda_s}$ and the resonant wavelength is λ_s so the concerns raised in section 3.3.6 do not affect the results).

3.4.4 Transverse Dynamics

As mentioned in the section 2.2.2, when the periodicity of the coupling slots of the MAP is equal to the incident laser wavelength (as is the case in the MAP design in Table 3.4), the transverse force in Equation 2.31 vanishes. As a result, the resonance should not contribute to any defocusing of the electron beam. This

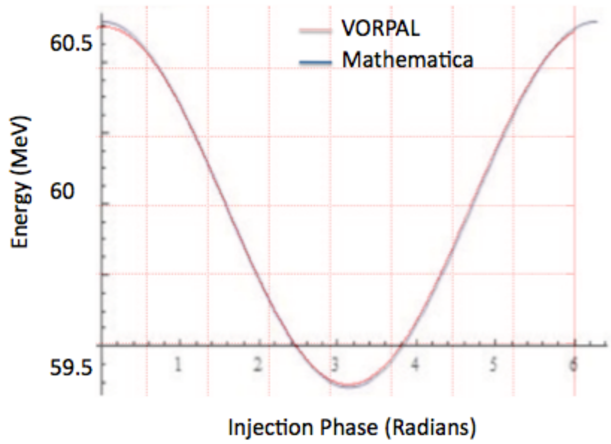

Figure 3.21: The energy distribution of an electron bunch after having travelled through the MAP's accelerating mode in Mathematica (with no phase slippage assumed) and in VORPAL (with all potential phase slippage causes accounted for) as a function of phase.

is confirmed in VORPAL simulations. In these simulations, a 60 MeV electron bunch with an initial transverse spot size of $\sigma_y = 50$ nm and a charge of 10 fC traverses the vacuum cavity of the MAP for 1 mm with the resonant fields excited and with no external fields excited. The initial transverse velocity of the electron bunch is 2 percent of the speed of light. The transverse spot size of the electron bunch as a function of its longitudinal position as it propagates along the MAP's vacuum cavity is given in Figure 3.22.

The similarity of spot size evolution indicates vanishing transverse forces for the accelerating mode. Furthermore, the growth of the spot size by 20 microns over a propagation distance of 1mm is due to the initial transverse velocity of the electron bunch. The ratio of 20 microns to 1mm is equal to the ratio of the initial transverse velocity to the longitudinal velocity of the electrons, indicating that the growth of the spot size is due to ballistic factors and not the resonant

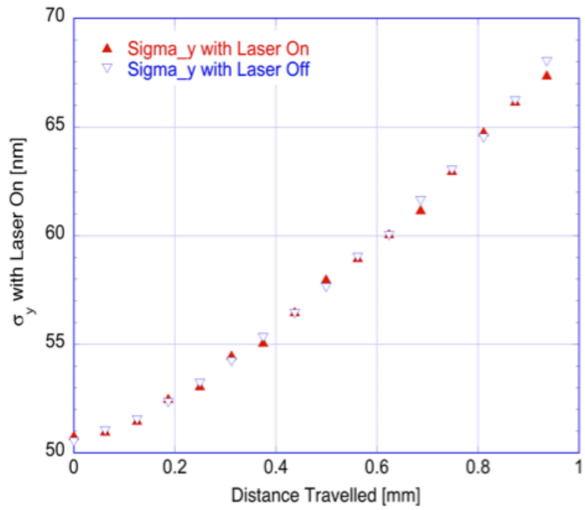

Figure 3.22: The transverse spot size of the electron beam as it traverses the cavity in two cases: with the accelerating mode excited and with the laser off.

fields. Other factors that could increase the spot size, including wake fields and space charge, do not contribute to the beam's growth either.

3.4.5 Wakefields

In general, when an electron beam passes through any structure with smooth inner walls, the wakefields generated by the electron beam are minimal. In the case of the MAP, the smooth inner walls combined with the small current that traverses the MAP in the experimental setting (less than 10 Amperes in Table 4.4) leads to minimal wakefield effects [35]. A VORPAL simulation in which a 10 fC electron beam with a bunch length of 10 fs traverses the MAP with no laser excitation is used to isolate the impact of wakefields within the MAP. A field overlay of the longitudinal component of the wakefields generated by this beam is given in Figure 3.23.

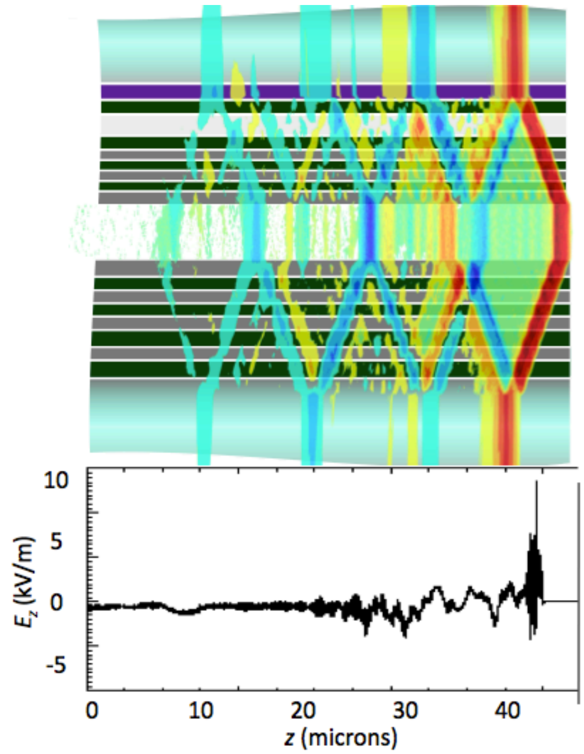

Figure 3.23: A color overlay and line out of the longitudinal component of the electric wake fields generated by a 10 fC beam passing through the MAP's accelerating cavity. The periodicity of the fields generated by the beam is a multiple of the longitudinal beam length.

The maximum amplitude of the longitudinal wakefield is 20 kV/m in the VORPAL simulation. The accelerating fields in the cavity when the MAP is illuminated exceed 100 MV/m, four orders of magnitude greater than the wakefields generated. Thus, the beam dynamics are dominated by the laser-generated fields.

3.4.6 Space Charge

In the experimental setting, tens of fC pass through the vacuum cavity of the MAP (note that in general, the low charge that passes through a DLA is compensated for by high rep rates). To examine whether space charge induced beam breakup occurs for electron bunches traversing the MAP, a series of VORPAL simulations in which a variety of electron bunches (with varying charge and transverse beam shape) travel through the MAP cavity with no accelerating mode excited. When a 50 fC beam with a transverse spot size (full-width half-maximum) of 50nm wide by 400nm tall (to fill the vacuum gap vertically) severe beam break up occurs, shown in Figure 3.24. Note that this beam break up instability is due to intra-bunch forces, as the bunch to bunch separation is roughly 0.1 seconds.

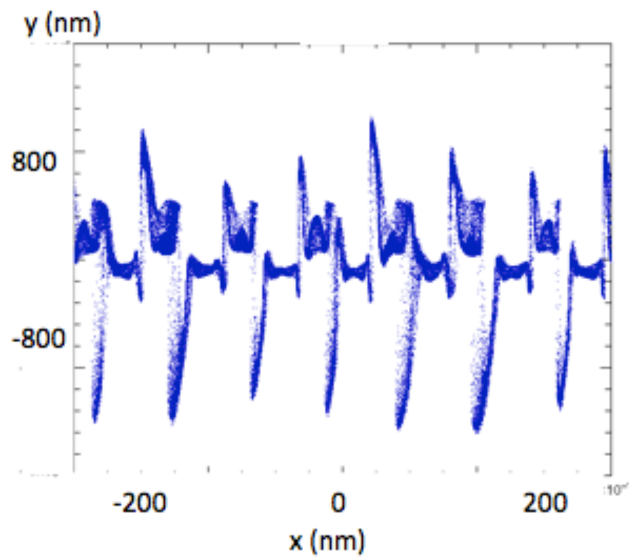

Figure 3.24: The transverse spot size of a 50 fC electron bunch after it has traversed the MAP's vacuum cavity for 1mm with no accelerating mode excited. The initial spot size is 400nm tall by 50nm wide.

The slab-symmetric geometry allows for the electron bunches that pass through it to be spread out in the transverse dimension x. These "ribbon beams" have a significantly lower charge density to reduce space-charge induced beam instabilities. For instance, a 50 fC beam with a transverse spot size of 10μm wide by 400nm tall shows no evidence of beam breakup after traveling through the

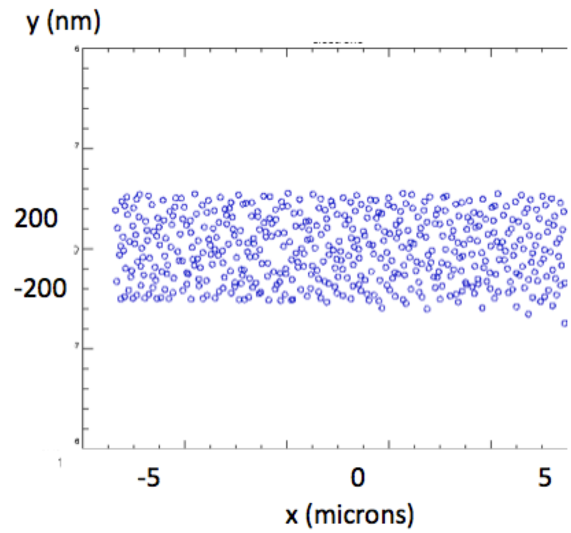

Figure 3.25: The transverse spot size of a 50 fC electron bunch after it has traversed the MAP's vacuum cavity for 1mm with no accelerating mode excited. The initial spot size is 400nm tall by 10μm wide.

vacuum cavity for 1mm, as shown in Figure 3.25. The electron beams that pass through the MAP in the experimental setting are tens of microns wide in the x dimension, so that space charge effects are minimal.

CHAPTER 4

Experiment

With the MAP fully designed and characterized via analysis and simulations, it can be built and tested experimentally. In this chapter, the MAP fabrication efforts and experimental settings, in which the resonant properties and acceleration capabilities of the MAP were investigated, are described.

4.1 Fabrication

Once a design of the MAP was finalized using zirconia, hafnia, and fused Silica with the dimensions specified in Table 3.4, the MAP was built. Though the description of fabrication work that follows is not the work of the author, it is critical in understanding how the MAP was tested and characterized experimentally.

4.1.1 Fabrication Processes

Fabrication was carried out at UCLA's two cleanroom facilities: the Integrated Systems Nanofabrication Cleanroom (ISNC) at the California Nanosystems Institute (CNSI) and the Nanoelectronics Research Facility (NRF). These facilities are equipped with the deposition, polishing, and patterning tools necessary to build the MAP.

4.1.1.1 Slot Lithography

The first step in the fabrication of the MAP is the deposition of the zirconia coupling slots and surrounding hafnia on top of a fused silica substrate. The fused silica substrate is chosen because it is transparent in the optical regime, with minimal losses [36]. To fabricate the coupling slots, the steps taken are [37]:

1. A positive polymer photoresist is patterned using optical lithography onto a polished substrate (A0 in Figure 4.1;

2. Zirconia is deposited on top of the patterned photoresist;

3. Photoresist is lifted off, leaving the zirconia slots on the substrate (A1 in Figure 4.1) ;

4. Hafnia is sputtered onto and in between remaining Zirconia slots (A2 in Figure 4.1, and

5. the excess Hafnia removed with chemical mechanical polishing (A3 in Figure 4.1).

4.1.1.2 DBR Fabrication

On top of the slot layer described in section 4.1.1.1, the matching layers of the coupler and the DBR for the top half of the MAP (consisting of Zirconia and Fused Silica) are deposited via sputtering deposition with a Denton Discovery Sputterer. The pressure and temperature in the sputtering machine determine the rate at which the alternating Zirconia and Silica layers are deposited. This rate is minimized to increase the precision of each layer in the DBR (high levels of precision are necessary due to the strict error tolerances in Table 3.7). Zirconia

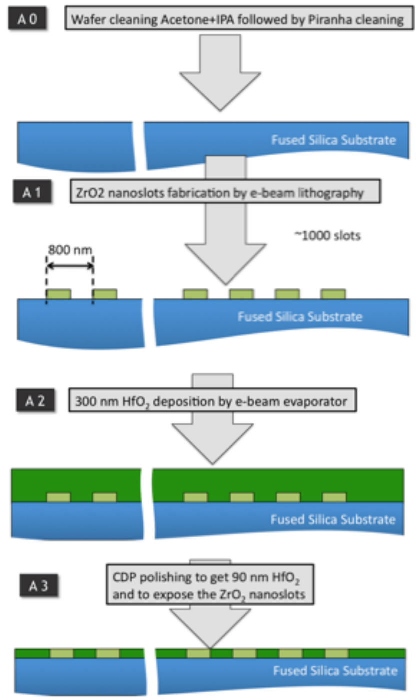

Figure 4.1: A series of fabrication steps summarizing how the coupling slots are patterned and deposited [38].

and Fused Silica are sputter deposited on a separate substrate to fabricate the bottom DBR.

4.1.1.3 Bonding and Gluing

Alluminum spacers are patterned and deposited onto the bottom DBR, as is shown in Figure 4.2. These aluminum pillars, 400 nm tall and separated by 3 mm, maintain a vacuum gap between the top and bottom halves of the MAP when the two halves are joined together. Before the top and bottom DBR are combined to form the full MAP design, the wafers on which the top and bottom halves were deposited are cut into 1mm long by 10mm wide pieces with a dicing saw. These dimensions are set in order for the MAP sample to fit into the DLA

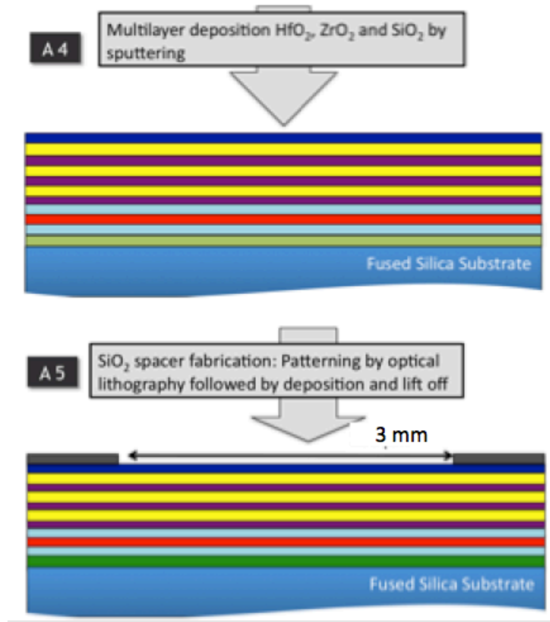

Figure 4.2: A series of fabrication steps summarizing how the DBR and metal spacers are deposited [38].

holder described in section 4.2.1.1. The top and bottom halves of the MAP are then placed, the former on top of the latter, in an Aluminum alignment/gluing jig. The metal pillars are used to align the two halves by eye with a precision of 10 microns in x and z. The "accelerating region" (i.e. the region between the metal pillars) is 3.4 mm wide and 1mm long, although misalignment may shorten these dimensions by roughly 10 microns. The diced and aligned structures are then glued together on their edges in x using Torr Seal, a vacuum-safe glue. The glue is greater than 3mm from the accelerating regions, so as to not interfere with acceleration in the experiment.

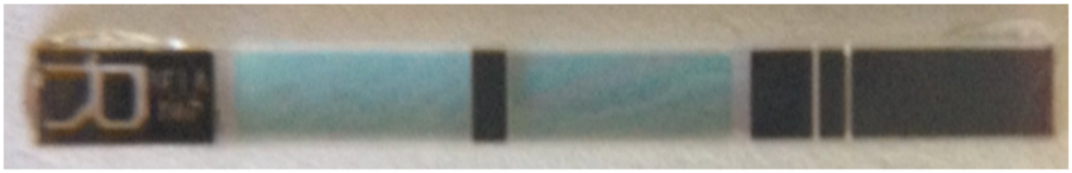

Figure 4.3: An optical image of the MAP after it has been fabricated, bonded, and diced. The blue regions correspond to the sections in which the top and bottom halves of the MAP are aligned. In the experiment described in section 4.2.2, electrons traverse these blue "accelerating regions" from the bottom of the figure to the top. The IR laser is incident into the page. The black regions correspond to the sections of the MAP sample onto which the metallic spacers were deposited.

4.1.2 Measuring Structure Parameters

A Dektek Profilometer was used to measure the total thickness of each half of the MAP structure. In regions of the substrate in which samples were chosen and diced, the measured thicknesses of the top and bottom halves (2.046 μm and 2.832 μm respectively) matched the designed thicknesses (2.050 μm and 2.830 μm respectively) to better than 1%. However, in order to determine whether the layer thicknesses of the fabricated MAP matched the ideal layer thicknesses of the designed and simulated MAP in Table 3.4, a Scanning Electron Microscope was used. As discussed in section 3.3.7, if the design parameters of the MAP do not match the ideal parameters, then the resonant frequency of the accelerating mode shifts and synchronous acceleration does not occur. It is therefore crucial that the fabricated MAP has design parameters within the error tolerance of the ideal design. A SEM works by impinging a sample with electrons and then measuring the scattering of those electrons as the beam is raster-scanned across the sample [39]. After using a Focused Ion Beam to cleanly dice a cross section of the MAP, a SEM imaged the layers of the MAP with a accuracy approaching 10 nm due to the combined effects of low-contrast and charge-induced blurring. One such image of the MAP is given in Figure 4.4.

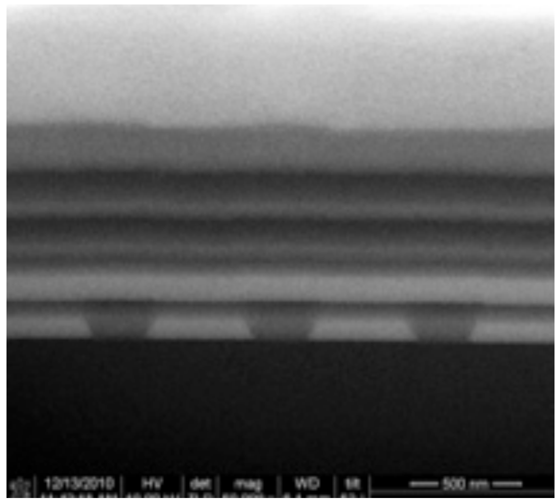

Figure 4.4: A SEM image of the top half of the MAP accelerator. Three coupling slots, as well as the DBR and matching layers are visible.

It should be noted that unfortunately, this imaging method is destructive. To see a cross-section of the structure like that shown above, the sample must be cut. Furthermore, when scanning an electron beam across the surface of the MAP, electrical charging tends to occur, which would destroy the structure and invalidate the image. To prevent this from happening, the structure must be coated in a conducting metal such as gold [39]. Nevertheless, cutting the structure and coating it in gold render it unusable. In the fabrication process, multiple samples are made simultaneously so that some can be experimentally tested and some can be imaged. Since the imaged structures and the experimentally tested structures are made in the same batch, It is assumed that they match each other in geometric dimension. The dimensions of imaged structures for two different

Table 4.1: Fabricated MAP Parameters.

Parameter	**Measured Value**	**Uncertainty**
g	400 nm	20 nm
ml	112 nm	5 nm
DBRl	143 nm	5 nm
DBRh	104 nm	5 nm
c1	155 nm	5 nm
c2	340 nm	5 nm
d	290 nm	5 nm
w	400 nm	2 nm
Hafnia Index of Refraction	1.98	0.002
Silica Index of Refraction	1.45	0.002
Zirconia Index of Refraction	2.12	0.003

designs of the MAP are given in Table 4.1 and Table 4.2 using the parameters labelled in Figure 3.8. The uncertainty in each parameter is generated by the resolution of the SEM as well as the uncertainty in determining visually where one layer in the MAP ends and the next begins.

With the exception of the parameters DBRh and DBRl, the measured layer thicknesses are within the error tolerances specified in Table 3.7. However, the uncertainty in the measured thicknesses of DBRh and DBRl exceed the error tolerances given in Table 3.7. However, those error tolerances are for systematic errors in the thicknesses of the DBR layers. If all of the Silica DBR layers are 5nm too thick, then the resonant frequency will shift outside of the window in which sufficient synchronous acceleration occurs. However, the uncertainty in Table 4.1 is a random uncertainty. One layer of the DBR may be 5nm too thick

Table 4.2: Fabricated MAP Parameters for First MAP Design.

Parameter	**Measured Value**	**Uncertainty**
g	800 nm	20 nm
ml	110 nm	5 nm
DBRl	138 nm	5 nm
DBRh	92 nm	5 nm
c1	110 nm	5 nm
c2	210 nm	5 nm
d	90 nm	5 nm
w	286 nm	20 nm
Hafnia Index of Refraction	1.98	0.002
Silica Index of Refraction	1.45	0.002
Zirconia Index of Refraction	2.18	0.003

but the next may be 5nm too thin, negating the resonant frequency shift resulting from the thicker layer. The simulations described in section 3.3.7 confirm that this type of random error does not significantly shift the resonant frequency. It should be noted that although the measured layer thicknesses match the design parameters to within the error tolerance, because the imaged structures are not the structures experimentally tested. Furthermore, structure to structure variation of layer thicknesses has been observed. As a result, before experimentally testing each structure, there is a large uncertainty in whether those structures can resonate and accelerate electrons. Future fabrication efforts of the MAP aim to improve upon this uncertainty with more repeatable deposition and lithography techniques.

4.1.3 Optical Testing

Once a sample is fabricated it is characterized optically before it is tested experimentally. In this fashion, the fabricated structure's ability to resonate is probed.

4.1.3.1 Experimental Setup To Find Resonance

To test whether the MAP can generate the standing wave resonance, an experimental setup involving a white light source, the MAP sample, and a photomultiplier tube photodetector was used [41]. In principle, if the MAP is resonating at a given wavelength, when light at that resonant wavelength is incident upon the MAP, a significant fraction of its energy will be "absorbed" by the accelerator and used to generate the resonance. As a result, the transmitted intensity will be lower at that resonant wavelength than at non-resonant wavelengths. By comparing the ratio of the transmitted intensity to the incident intensity (a ratio traditionally referred to as S21 in the accelerator community) as a function of wavelength with the simulated transmission spectra discussed in section 3.3.5, it can be deduced whether the fabricated MAP is resonating or not.

4.1.3.2 Spectrophotometer Measurements

A Shimadzu UV-3101 PC Spectrophotometer was used to measure the transmission spectra of the MAP samples. The measurements were done in the wavelength range of 400-1500 nm using a white light source and a PMT detector, as summarized in Figure 4.5.

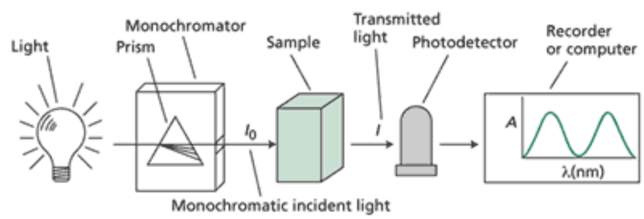

Figure 4.5: The set-up of a generic spectrophotometer [40].

A collimator is used to reduce the spot size of the white light source to 2mm by 2mm when it reaches the sample. After measuring the baseline spectrum of the white light source without any sample between it and the photodetector, the MAP sample is placed in the path of the white light and the transmitted intensity is measured as the wavelength of the white light source, as selected by a monochromator in 0.2nm wide ranges, is varied over a range of 400nm-1500nm. The baseline spectrum is subtracted from the transmission spectrum obtained with the sample in place to find the transmitted intensity as a function of wavelength.

4.1.3.3 Lack of Evidence for Resonance

The transmitted spectra for 3 fabricated MAP samples as well as the simulated transmitted spectrum for the design of the MAP specified in Table 4.1 are given in Figure 4.6.

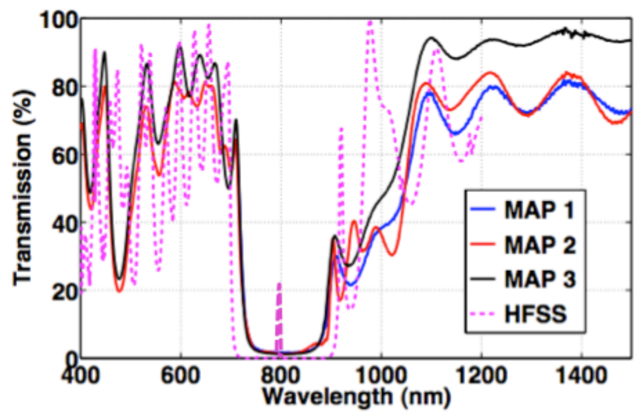

Figure 4.6: The transmitted light through the MAP as a function of wavelength for 3 fabricated MAP samples and the simulated MAP design.

The MAP sample spectra exhibit a characteristic 'valley' centered around 800nm that results from the quarter-optical-wavelength thick layers in the DBR in the MAP design. The bandwidth of this high reflectivity region is determined by the indices of refraction of the hafnia and fused silica that compose the DBR [45]. In Figure 3.9, there is a peak (relative to the surrounding high-reflectivity region) in the simulated transmitted spectrum at 800nm that corresponds to the absorption of electromagnetic energy by the accelerating mode in the vacuum cavity of the MAP, which does not appear in the transmitted spectra of the fabricated MAP samples. This negative result indicates that the samples did not resonate observably when illuminated by the white light source used in the set up described in section 4.1.3. Two factors contributed to not observing a resonance.

First, the white light source is incoherent. Since the filling of a resonant cavity depends on a coherent source and all of the simulations showing resonance were with coherent sources, an incoherent source would wash out the building up of the resonance with its varying incident phase, a fact that was not fully appreciated at the time that this characterization was designed. Unfortunately, facilities with coherent sources designed to make this kind of spectral measurement were not routinely available. When a set up with a coherent source was used at SLAC, the structure tested had flaws (i.e. its resonance was very weak) that made the resonant peak undetectable. Second, the spot size and location of the light source on the structure were difficult to control while performing the experiment. The spot size of the incident light on the sample was typically larger than 1mm in both x and z. As a result, a fraction of the incident light does not hit the sample and instead propagates to the photodetector unobstructed, increasing the detected transmission signal. It is possible that a small peak in the transmitted spectrum due to a resonance in the fabricated samples would be buried in this increased transmission signal. With this in mind, the MAP was placed in a holder to prevent light from leaking around the sample, yet no resonant peak was found in the resulting transmission spectra. Nevertheless, the incoherent light source in this experimental set-up renders the spectral measurements of the MAP inconclusive.

4.2 Experimental Setup

4.2.1 Test Facility

The experimental testing of the MAP (and any DLA for that matter) places numerous requirements on any facility to be considered as a setting for these experiments. To transmit electrons through the MAP's micron-tall by mm-long vacuum gap, an electron beam with a micron-scale spot size and emittance is required. Furthermore, the MAP is designed to accelerate relativistic electrons and the facility in question would need to provide electrons with sufficiently high energy to be synchronously accelerated in the MAP. To generate the accelerating fields in the vacuum cavity, an optical laser needs to illuminate the MAP structure. This laser needed to have a spot size that matches the width and length of the acceleration channel, a pulse length that is greater than the fill time of the structure, and a fluence sufficient to reach the breakdown threshold of the dielectric materials composing the MAP. Using the breakdown threshold of the oxides in the MAP measured by B. Stuart [12] and the MAP's enhancement factor given in Table 3.5, the fluence of the incident necessary to reach the breakdown threshold of the MAP is calculated to be 0.1 J/cm^2. Lastly, the facility used needs to have a staging set up that would be appropriate for running a DLA experiment. These requirements are summarized in Table 4.3. Note that the energy and emittance limits in these table are set in order to ensure minimal phase slippage and sufficient transmission through the vacuum channel respectively.

The Next Linear Collider Test Accelerator (NLCTA) at SLAC satisfies these requirements and was used as the location of the experimental testing of the MAP.

4.2.1.1 E-163 at the NLCTA

The NLCTA [42] is a multi-user accelerator facility that produces a high-brightness electron beam suitable for a wide variety of experiments ranging from THz generation to IFELs. A simplified schematic of the beamline is given in Figure 4.7. The beamline will be described sequentially starting from the cathode that gener-

Table 4.3: Requirements for A Facility in which MAP can be Tested.

Parameter	**Requirement (Order of Magnitude)**
Electron beam σ_y x σ_x	10μm x 50μm (maximum)
Electron beam transverse emittance	5μm-rad x 20μm-rad (maximum)
Electron beam energy	10 MeV (minimum)
Laser Spot Size	1mm x 1mm (maximum)
Laser Pulse Length	5 ps (minimum)
Peak Laser Fluence	0.5J/cm^2 (minimum)

ates the electron beam and ending with the diagnostics downstream of the MAP sample.

The electron beam at the NLCTA is produced when a 10 Hz UV pulse is incident upon a Copper cathode. These electrons are accelerated through an S-band Gun and X-Band LINAC until they reach an energy of 60 MeV. The energy spread of each electron bunch is quite small (see Table 4.4), but the shot-to-shot jitter can approach 50 keV when system conditions are poor. Since monitoring the energy profile of the electron beam is the way in which acceleration is observed in this experiment, energy jitter and energy spread are critical factors in determining the quality of the collected data.

To reduce the energy jitter and energy spread, collimating jaws are employed. After the LINAC, the electrons pass through a chicane in the middle of which these two remotely controlled collimating jaws are placed. As the jaws close, a restricted subset of the beam passes through the chicane and further down the beam-line. This beam, with a charge on the order of 100 fC has a reduced energy spread and energy jitter. Since the horizontal position of the electron beam in

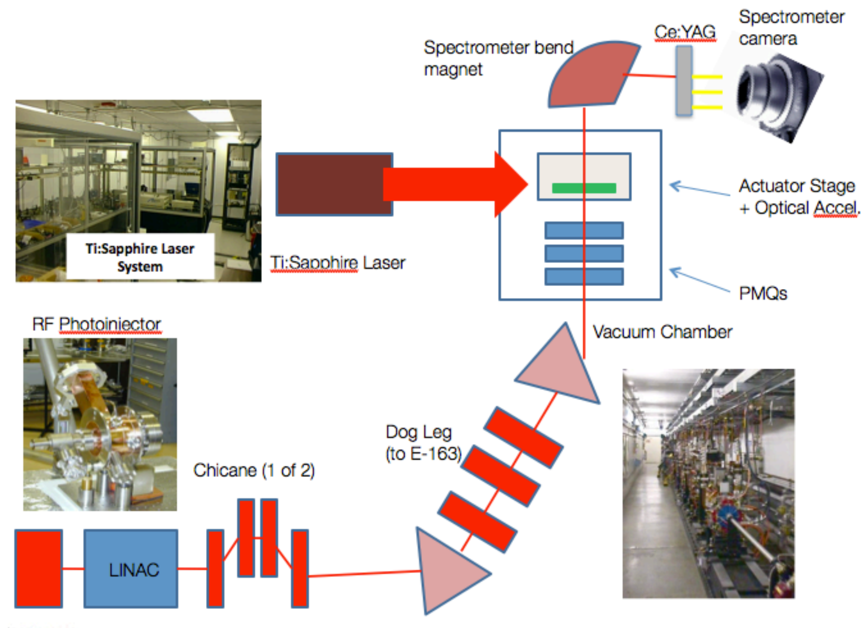

Figure 4.7: A simplified overview of the NLCTA beam-line. Although not all of the focusing/steering quadrupoles are accounted for, the overall schematic is correct.

the chicane is correlated with its energy, When the beam shifts in energy by more than a specified amount it hits the sides of the jaws and does not advance further. After passing through the chicane, the beam is sent through a dogleg and into the experimental hall. The strong bending magnets in the dogleg combined with the energy jitter of the electron beam result in a positional jitter downstream at the MAP interaction point. Additionally, the dogleg is a strong dispersive element that results in beam orbit deviation (and beam quality degradation) for electrons that are not exactly on tune (i.e. 60 MeV).

In the experimental hall, the beam passes through 6 final focusing quads and then through a triplet of permanent magnetic quadrupoles. A diagram of the final section of the experimental set up is given in Figure 4.9. By adjusting the strength of the final focusing quadrupoles and ensuring the electron beam passes

Table 4.4: NLCTA Nominal Electron Beam Parameters for E163 Operation.

Parameter	**Value**
Energy	60 MeV
Energy Jitter	50 keV (10 keV with collimating jaws in)
Energy Spread (FWHM)	10 keV (5 keV with collimating jaws in)
Charge Off Cathode	10 pC (100 fC with collimating jaws in)
Bunch Length	0.5 ps
Vertical Spot Size (FWHM)	50 μm
Horizontal Spot Size (FWHM)	100 μm
Emittance	1 μm-rad

through the PMQs on axis, the electron beam is brought down to a size of tens of microns in each transverse dimension. This strong focusing results in a beam that is very divergent, making the transmission of electron beam through the vacuum channel difficult.

The MAP is placed on a micro-structure holder that is situated on a 4-axis piezo actuator stage. The stage can move in the horizontal and vertical dimensions (x and y) as well as in the tip and tilt orientations. The ranges that can be traversed by the actuators are 10mm, 1mm, 10 degrees, and 30 degrees respectively. Within the sample holder is a Cerium doped YAG screen that is used to monitor the transverse profile of the electron beam and measure its spot size at the electron-MAP interaction point. An example of a transverse electron spot on the YAG screen is given in Figure 4.8.

By monitoring the beams spot size on a YAG screen as upstream quadrupole magnet strengths are varied is measured. As the strength of an upstream quadruple is varied, the beta function β of the electron beam is changed as well. The

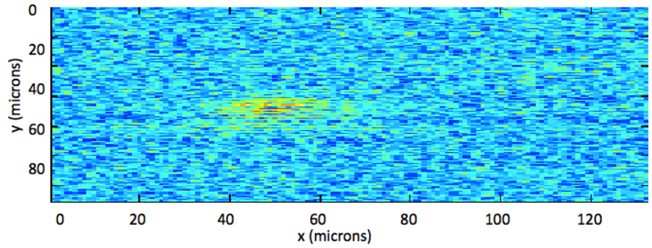

Figure 4.8: An image of the electron beam on the YAG screen at the same longitudinal position as the MAP sample. The beam, used in the data described in sections 5.2.1 and 5.2.2, is fitted to a gaussian in both x and y. The fitted FWHM is 25 microns in x and 15 microns in y.

emittance ϵ can be calculated by fitting the dependence of the spot size σ on β to a parabola, since the spot size depends on β and ϵ as is shown in Equation 4.1:

$$\sigma = \sqrt{\frac{\epsilon\beta}{\gamma}}. \tag{4.1}$$

The emittance of the electron beam used to collect the data in sections 5.2.1 and 5.2.2 is measured as 25 micron-radians horizontally (in x) and 3 micron-radians vertically (in y), within the requirements described in Table 4.3. A list of typical beam parameters is given in Table 4.4.

To monitor the beam after it has traversed the MAP, a 90 degree spectrometer bend magnet is situated downstream of the structure that sends the beam to a point-to-point Lanex phosphor screen imaged by an intensified camera (PI-MAX3). The PI-MAX3 camera has a system noise level rms of 20 e^-,a dark current of 4 e^-/pixel/second, and a HQf intensifier that provides a high signal to noise ratio for the transmitted population of electrons that make it through the vacuum cavity of the MAP. Since the bend radius of an electron traveling through the spectrometer magnet is dependent on its momentum, the horizontal position of the beam-image on the screen is linearly correlated with energy. The energy difference between horizontally adjacent pixels on the CCD (charge-coupled device) of the PI-MAX3 is 1.4 keV. This image of the electron beam on the Kodak Lanex phosphor scene, imaged by the CCD of the PI-MAX3, is used as an energy diagnostic downstream of the MAP.

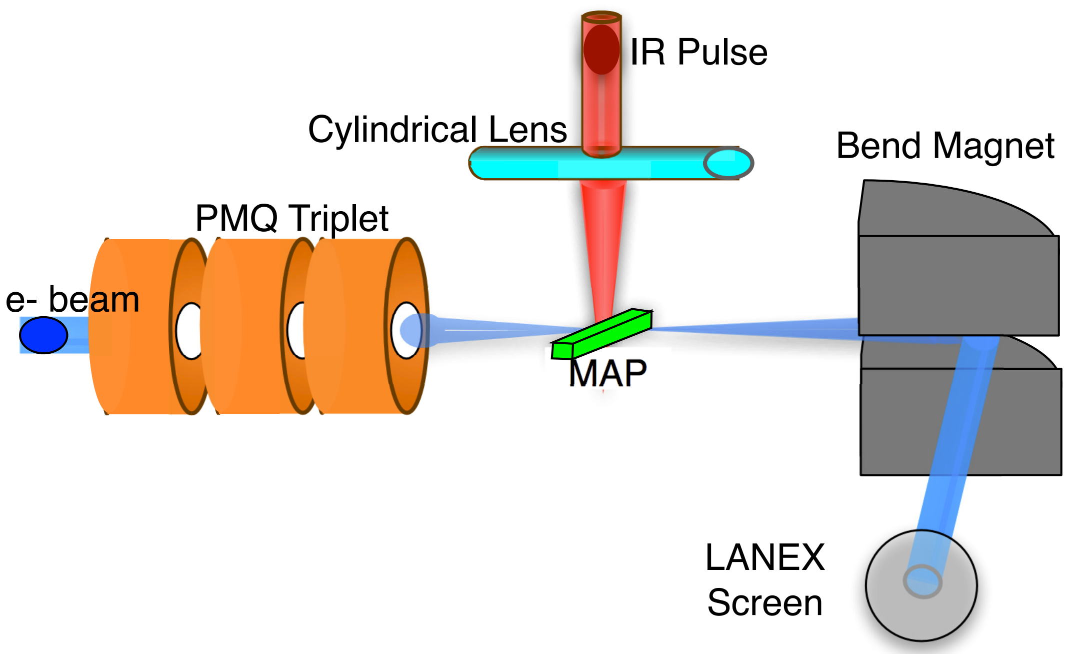

Figure 4.9: A diagram of the final section of the E-163 beam-line, including the interaction with the MAP itself. Ideally, the electron beam is focused to a small spot at the MAP's location, where an IR laser pulse has excited the accelerating mode. Downstream of the MAP, the beam traverses a 90 degree bend magnet that serves as an energy profile diagnostic.

4.2.1.2 The Ti:Sapphire Laser

A Ti:Sapphire laser system in a room adjacent to the experimental hall generates a 800nm wavelength pulse with a variable pulse length and energy (usual operating values are 1ps and 1mJ respectively). The class IV system available at NLCTA uses a crystal of sapphire doped with titanium ions that is pumped with a frequency doubled Nd:YAG laser, The pulse then traverses a mode-locked oscillator and a stretcher. The pulse length of the IR can be altered by adjusting the location where the IR exits the stretcher and is sent to the experimental hall. However, if the pulse length of the IR is stretched beyond 6ps, a correlation develops between the longitudinal coordinate of the IR pulse and energy. This "chirp" manifests itself as the front of the IR pulse having a higher energy than the back of the pulse, and is minimized in the experiment. After exiting the stretcher, the IR is transported along a series of simple NIR optical elements into the experimental hall and is directed downward onto the MAP from above. The spot size of the laser is controlled by adjustably positioned lenses above the MAP stage and is matched to the longitudinal length of the MAP acceleration channel (1 mm) in the z-direction and slightly larger (40 μm than the transverse spot size of the electron beam (25 μm) in the x-direction.

4.2.2 Experimental Procedure

To observe acceleration, a series of procedural steps first need to be executed. These steps have a direct impact on the data collected during the experiment as well as its analysis, so for reference purposes, the procedure is outlined here.

4.2.2.1 Electron Beam Tuning

Before the electron beam reaches the MAP structure, it must first traverse the series of quadrupole magnets, steering magnets, accelerating cavities, and chicanes that comprise the NLCTA beam-line. A summary of the beam-line is given in the Figure 4.7, though not every magnet in the beam-line is accounted for in this image.

To minimize the spot size and emittance of the beam when it reaches the sample in the experimental hall vacuum chamber, user adjusts the phase and amplitude of the RF klystron powering the accelerating cavity while the electron bunch traverses the linac, the strength (currents) of the quadrupoles composing the beam-line, and the position of the beam (by adjusting various steering magnet strengths) as measured on various beam position monitors (BPMs) placed along the line. Additionally, there are a series of profilometer screens (and corresponding devoted cameras) that can be used to measure the beam spot size and position at various points along the line [42]. However, even at optimal conditions, the electron beam is much larger than the vacuum cavity of the MAP (see Table 4.4) and so only those electrons that traverse the cavity will be accelerated.

4.2.2.2 Laser-Electron Timing Overlap

To achieve acceleration in the MAP, the IR pulse and the electron beam need to arrive at the MAP sample at the same time and at the same spot on the structure. To ensure temporal overlap, a method created by the E-163 group at SLAC [28] was employed. The IR pulse is directed towards a fast photodiode downstream of the accelerating structure. The OTR signal generated when the electron bunch striking the glass substrate of the MAP is also steered towards this fast photodiode and then overlapped with the IR signal to ensure timing overlap within the resolution of the fast photodiode, 50 ps. The layout of the fast photodiode relative to the MAP sample is given in Figure 4.10. Since the fill time of the structure is 5 ps, the electron beam and IR need to be overlapped with a precision finer than 50 ps if the electrons are to traverse the MAP while the resonating mode is excited. This overlap is achieved by varying the path length

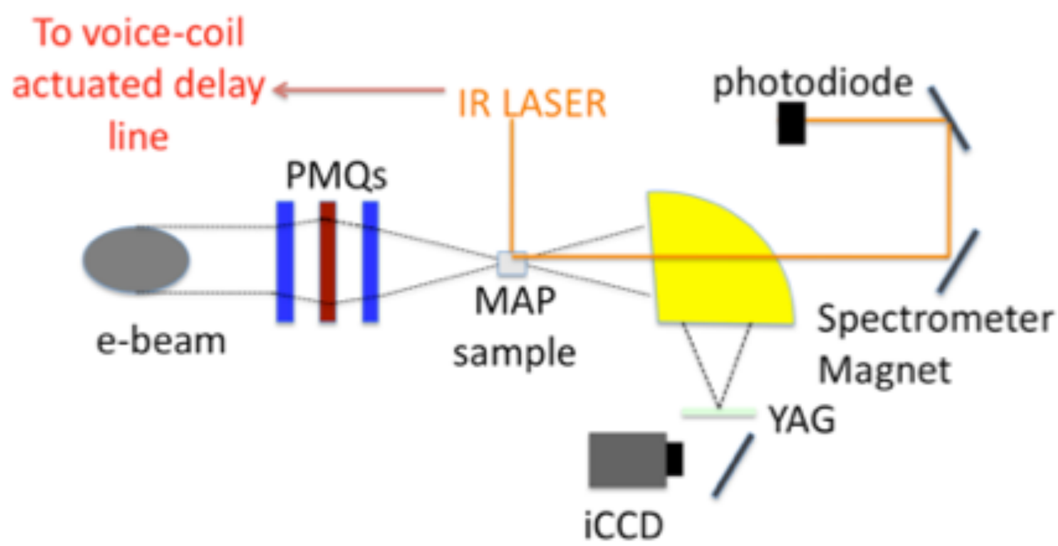

Figure 4.10: A schematic of the final section of the experimental hall, with the fast photodiode's position indicated. Note that the OTR and IR signals travel straight through the spectrometer bend magnet.

of the incident IR while data is being collected and is described in more detail in section 4.2.2.6.

4.2.2.3 Laser-Electron Spatial Overlap

Acceleration will not occur if the laser spot (approximately 100 microns wide) is illuminating a different part of the MAP than that which the electron beam is traveling through. To ensure spatial overlap of the two beams, a camera focused on the back of the MAP sample is used to detect the spatial position of the electron beam (from Optical Transition radiation [44]) as well as the spot where the IR strikes the sample. This image is shown in Figure 4.11.

Spatial alignment of the electron beam and the IR pulse is achieved by adjusting mirrors in the IR beam path until the IR reflections are overlapping the OTR

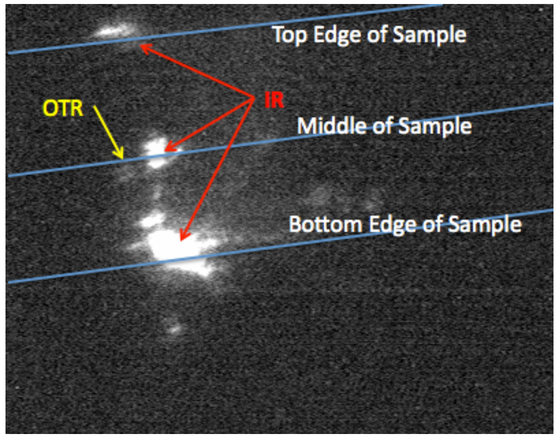

Figure 4.11: An Image of the back of the MAP sample while it is both illuminated by the IR laser and struck by the electron beam. The reflections of the IR beam are visible on the top edge of the top half of the MAP sample, the middle surface where the top and bottom halves meet and the surface where the bottom half touches the DLA holder. The optical transition radiation generated by the electron beam hitting the sample is visible on the middle surface, next to the IR reflection.

signal. This only ensures spatial overlap within one beam width of the larger of the two signals. To achieve better overlap, the spatial position of the incident IR is varied by an amount less than the spot size of the electron beam between data collection runs.

4.2.2.4 Laser Perpendicularity

Achieving acceleration in the MAP not only requires spatial and temporal overlap of the IR and electron beams, but also that the IR beam is perpendicular to the structure. If the IR laser is not perpendicular to the MAP sample, then the phase of the resonance (φ_0 in Equation 2.6) will have a dependence on the longitudinal coordinate z, as illustrated in Figure 4.12. A calculation of the energy imparted

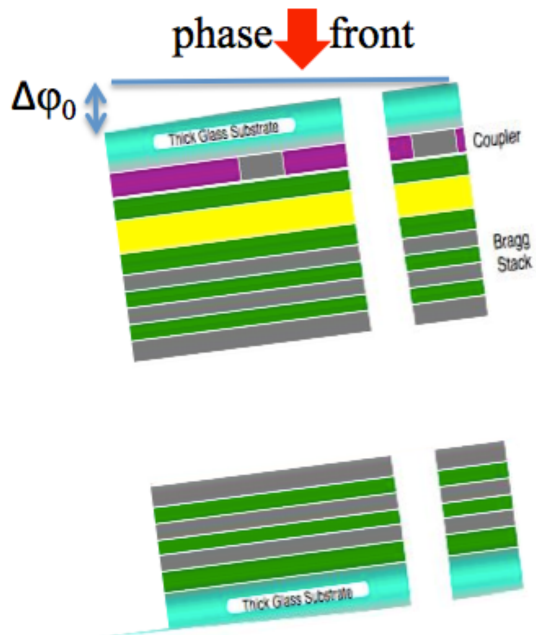

Figure 4.12: An Image of the MAP in which the top surface is not perpendicular to the propagating direction of the incident laser source.

to an electron traversing a standing wave electric field with a phase that changes as the electron traverses the cavity shows that the IR needs to be perpendicular to the top edge of the sample to within 0.01 degrees for 100 keV of energy gain to occur [43]. The equation for the average accelerating force per period encountered by an electron after having travelled through N periods of the MAP with a tilt of θ with respect to the incident laser phase front is

$$< F_z >= \frac{q}{N\lambda} \int E_z e^{ikz \sin\theta} dz. \tag{4.2}$$

After substituting E_z from Equation 2.6 into this equation, it is found that for appreciable energy gain, θ must be less than 0.01 degrees. In fact, if $\theta = 0.02$ degrees, the total energy gain is 0 keV. To ensure the perpendicularity of the IR beam path and the top surface of the MAP, a camera and set of mirrors, lenses and a partial pick-off mirror are set up above the sample to observe both the incident and reflected IR spots on a screen. The set-up for this perpendicularity measurement is shown in Figure 4.13 When these spots overlap on the screen, perpendicularity is achieved to within 0.01 degrees.

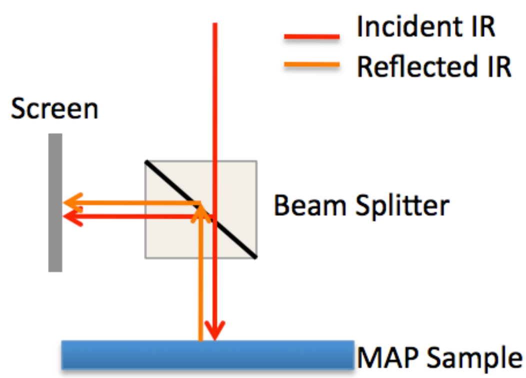

Figure 4.13: The setup used to confirm that the IR is perpendicular to the top surface of the MAP surface. When perpendicularity is achieved to within .01 degrees, the incident (red) and reflected (orange) spots overlap on the screen.

4.2.2.5 Electron Transmission

Since the spot size of the electron beam is larger than the vacuum gap, most of the electron beam travels through and loses energy to dielectric material. When the electron beam strikes the substrate that the MAP is built upon, the spectrometer camera detects a large straggled population of electrons corresponding to those electrons that have scattered through the substrate. When the electron beam passes entirely above the structure, a much thinner (in energy spread) distribution is observed. By moving the actuator stage until both the thinner population and the straggled (lower energy) population are present, the actuator position at which the electron beam is striking the top edge of the top substrate can be located.

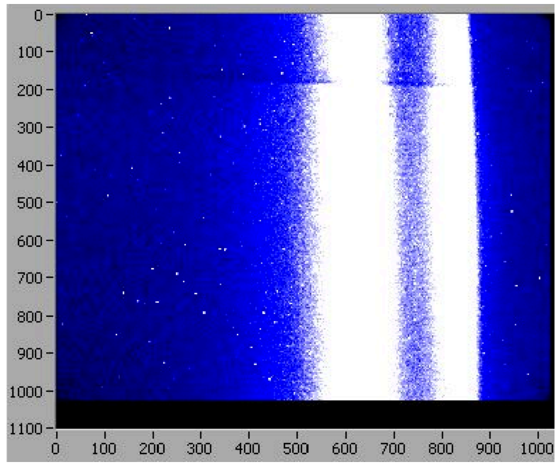

Figure 4.14: An image of the Lanex phosphor screen downstream of the spectrometer bend magnet when the electron beam is straddling the top edge of the MAP sample. The x-axis of this screen is correlated with energy. The broader, lower energy distribution to the left corresponds to the electron population that has scattered through the glass and lost energy to the glass. The thinner higher energy population corresponds to the electrons that have passed over the top of the glass.

Using the top edge of the sample as a reference point, the stage is then moved so that the electron beam is striking where the acceleration channel should be located. By adjusting the vertical position and tip angle of the stage while monitoring the energy profile of the electron beam on the Lanex phosphor screen downstream of the spectrometer bend magnet, transmission is achieved when the thinner transmitted population is found in addition to the lower energy straggled population.

The profile of the transmitted population (to the right in Figure 4.15 is expected to change when the MAP is illuminated by the Ti:Sapphire laser and the resonance is excited, since the energy of the transmitted electrons will be mod-

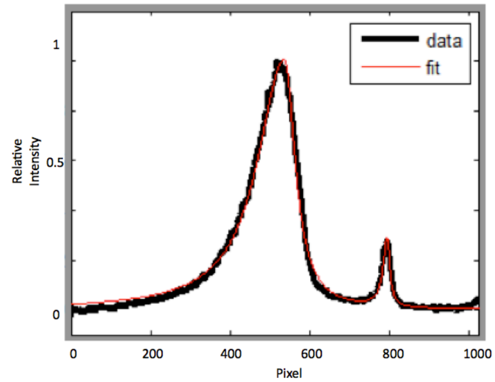

Figure 4.15: A line out of the energy spectrum of the NLCTA beam after having traversed the MAP. The thinner population to the right (higher energy) corresponds to those electrons that were transmitted through the acceleration channel. The broader peak on the left corresponds to those electrons that scattered through the glass/dielectric materials of the MAP.

ified. By monitoring how the shape and width of this population changes when the MAP is illuminated compared to when the MAP isn't illuminated, evidence of acceleration can be detected. To aid in the search for the change in the profile of the transmitted population, a fitting algorithm is employed. The energy spectra are fitted to curves containing the two distinct, scattered and transmitted, electron distributions. Multiple functions (including Lorentzian distributions, gaussian distributions and hyperbolic secant squared distributions) were fitted to these two distributions. The scattered distribution was fitted to a half Lorentzian on its low-energy side and a half sech^2 on its high-energy side. The transmitted population was fitted to a gaussian. These functions were found to minimize the χ^2 of the fits to the data [28]. The r.m.s. of the gaussian fitted to the transmitted population serves as a figure of merit for acceleration; if the transmitted population is accelerated, the width of the forward gaussian increases.

4.2.2.6 Searching for Acceleration via Timing Scans

The timing overlap of the electron beam and the IR beam on the fast photodiode has a precision of 50 ps, whereas to ensure that the electron beam traverses the cavity while the accelerating mode is excited, a timing overlap of less than 5 ps is necessary. To achieve this level of simultaneity, a voice coil in the laser path randomly varies the IR path length over a range of 18mm (corresponding to varying the arrival time of the IR over a 50 ps window) during the data collection phase of the experiment. Thus, the electron beam and IR beam are overlapped temporally on a subset of the shots. These results are detailed in the following chapter.

CHAPTER 5

Acceleration Testing: Results and Analysis

Multiple MAP samples have been experimentally tested at the NLCTA facility, described in section 4.2.1.1. The goal of the testing was to observe and maximize acceleration in the MAP, thus proving the principle of acceleration in a resonant DLA. There have been 2 distinct MAP designs and 8 samples tested during 8 experimental runs, summarized in Table 5.1.

In Table 5.1, Design 1 refers to the design in Table 4.2 and Design 2 refers to the design in Table 3.4. After Run 1 failed to find transmission of the NLCTA electron beam through the MAP's vacuum cavity, alignment channels were added to the MAP's substrate. These alignment channels, tens of microns tall each, aided in the location of the accelerating region vacuum channels. After optimizing the bonding process of the top and bottom halves of the MAP, described in section 4.1.1.3, the "double-horned" electron energy distribution indicative of acceleration in the MAP (described in section 3.4.2) appeared during Run 6. In order to gain further confidence in the MAP's ability to accelerate electrons, a new MAP design with the dimensions given in Table 4.1 was tested and acceleration was once again found. The data collected during Runs 6 and 9 is detailed and analyzed in what follows.

Table 5.1: Summary of Experimental Testing of the Micro-Accelerator Platform.

Run	**Date**	**Design**	**Comments**
1	4/12	1	Transmission Not Found, Gap collapsed
2	6/12	1	Transmission Found, Alignment Channels added
4	8/12	1	Adhesive Damaged Due to Beam Exposure
5	10/12	1	Voice-Coil Failed
6	12/12	1	Structure Damaged via Breakdown; Double Horn Found
7	4/13	1	Fabricated Gap Too Large
8	6/13	1	Transmission, No Acceleration
9	11/13	2	Acceleration Found

5.1 Analysis Methods

The data collection process begins with the recording of electron bunch energy profiles after the bunches have traversed the MAP while the MAP is either laser-illuminated or not. The non-illuminated spectra serve as baseline references to be compared with the potentially accelerated energy spectra of electron bunches having traversed the MAP with the sample illuminated. While the energy spectra are being recorded (using the spectrometer-screen-camera set up described in section 4.2.1.1), the path length of the IR pulse is varied over a 50 ps window (to ensure synchronicity between the time of arrival of the IR pulse and the electron beam on a subset of the collected data), as described in section 4.2.2.6. For each set of spectra, the following analysis steps are taken.

1. A line-out of the energy spectra is taken, resulting in images such as Figure 5.1;

2. the fitting functions described in section 4.2.2.5 are fitted to the line-out spectra;

3. various figures of merit (e.g. gaussian widths, peak locations and amplitudes) are calculated for each fit; and,

4. these figures of merit are plotted as a function of the IR path length and statistical signs of acceleration are searched for.

5.2 Acceleration Tests

Two MAP sample designs, Design 1 and Design 2 in Table 5.1, were tested during the MAP's experimental program. The measured parameters of Design 1are given in Table 4.2. For future reference, the enhancement factor η (defined in section 3.3.1) of the Design 1 is 4, the fill time of the sample is 5 ps and consequently, the laser fluence at which the sample is damaged is 0.2 J/cm^2 .

The electron beam that reaches the MAP sample is much larger than the MAP's vacuum cavity. Each election bunch has a transverse full-width half-maximum (FWHM) of 45 μm in the y-dimension, 50 μm in the x-dimension (as measured on the YAG screen shown in Figure 4.8) and a transverse emittance of the electron beam of 3 micron-radians in the y-dimension and 25 micron-radians in the x-dimension. The pulse length of the Ti:Sapphire laser incident upon the MAP is matched to the fill time of the MAP sample, 5 ps. The transverse spot size of the IR-pulse ensures that the pulse illuminates the entire sample longitudinally and the entire size of the beam in the x-dimension: it is 1 mm large in the z-dimension and 50 μm large in the x-dimension.

5.2.1 Electron Energy Spectra

The first run showing signs of energy gain was Run 6. Figure 5.1 shows sample electron energy spectra from that run, with and without laser illumination.

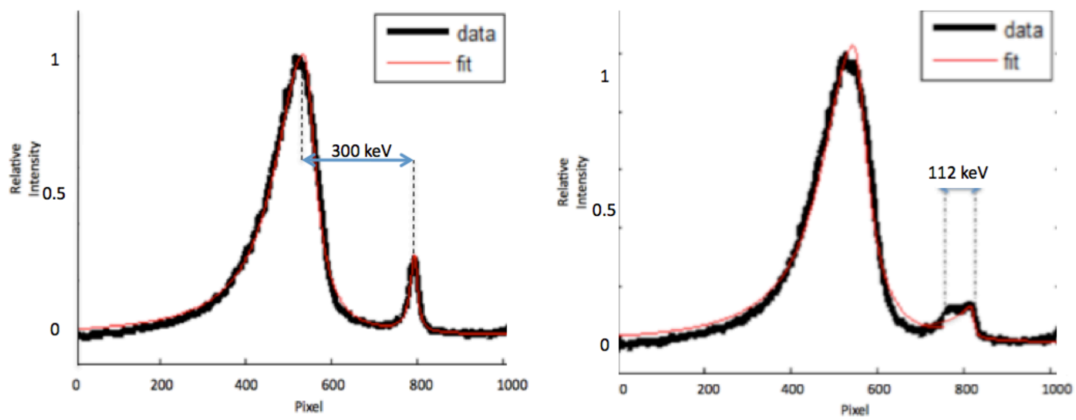

Figure 5.1: The energy profile of an electron bunch from the NLCTA after having traversed the cavity with no resonating mode excited (left) and with laser illumination (right).

The energy profiles in Figure 5.1 resemble the shape of the simulated energy profiles in Figure 3.18 and Figure 3.19 respectively. The energy separation between the center of the transmitted population and the straggled population is 300 keV in both the simulated and actual spectra. The transmitted population on the right in Figure 5.1 forms the double horned distribution indicative of acceleration by a standing wave. The peak-to-peak width of the double horned distribution is 112 keV, indicating an maximum energy gain of 56 keV by the transmitted population. Recalling the enhancement factor $\eta = 4$ and the breakdown fluence of 0.2 J/cm^2 for Design 1, the measured laser fluence during this test of 0.04 J/cm2 is seen to be only 20 percent of the damage threshold. Thus acceleration will be well below the maximum predicted values. The incident laser has a peak electric field amplitude of 31 MV/m and as a result, the accelerating mode has a peak amplitude of 124 MV/m. Simulations predict that the maximum energy gradient in the cavity is then 62 MeV/m. The discrepancy between this computed value of the energy gradient and the measured value of 56 MeV/m is likely due to errors in fabrication resulting in a reduced enhancement factor and/or shifted resonant frequency, as is discussed in section 3.3.7. Although the spectra in Figure 5.1 suggests that the MAP sample being tested was capable of accelerating electrons, no correlation between the acceleration signal and the path length of the incident IR (varied by the voice coil system described in section 4.2.2.6) was observed. In the absence of such an observed correlation, the demonstration of acceleration in Run 6 remains less than conclusive. In an effort to find such a correlation, a second set of MAP samples was fabricated using the steps outline in section 4.1 with parameters matching those in Table 3.4 and was first tested successfully in Run 9. Figure 5.2 shows sample energy spectra obtained during that run, with and without simultaneous laser illumination of the structure.

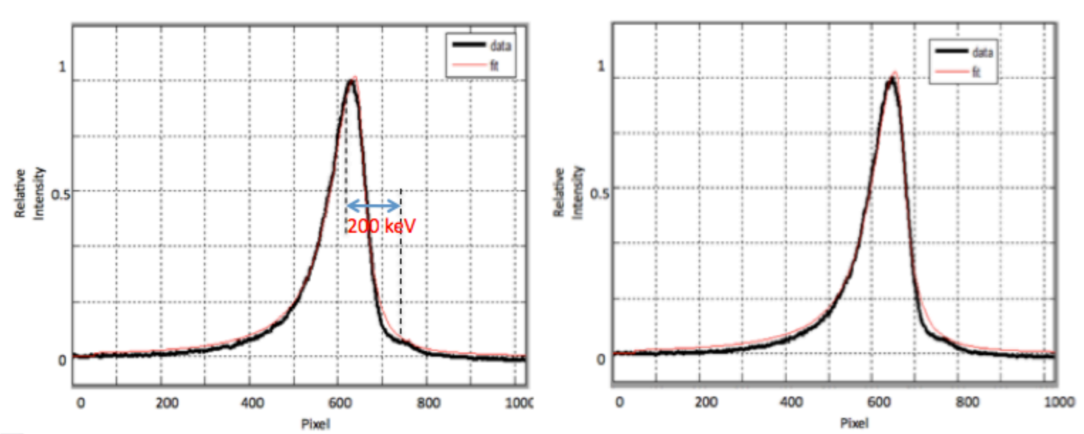

Figure 5.2: Energy profiles of electron bunches collected during Run 9 with no resonant mode excited (left) and with the resonant mode excited (right).

The transmitted electron populations in Figure 5.2 have smaller amplitudes relative to the straggled glass population and smaller energy separations from the straggled glass population when compared to Figure 5.1. The smaller amplitude is due to the 400-nm tall vacuum cavity of the MAP design in Table 4.1, half the size of the vacuum cavity of the MAP sample in Table 4.2. The smaller energy separations in Figure 5.2 are likely due to the partial occlusion of the vacuum cavity of the MAP sample by dielectric material that sagged into the cavity as a result of imprecise dicing, discussed in section 5.3. Since the transmitted population is small in amplitude and closer to the straggle glass population, observing a clear acceleration signal "by eye" (as is observed in Figure 5.1 is difficult and instead, the fitting algorithm described in section 4.2.2.6 is employed to monitor signs of acceleration in the spectra.

5.2.2 Cross-correlation of Energy Gain and Relative Timing in Run 9

The relative timing of the arrival of the Ti:Sapphire laser pulse and the electron beam was varied during data collection by modifying the IR path over a 18mm window, corresponding to a timing window of 50 ps, as is described in section 4.2.2.6. The width of a gaussian fitted to the transmitted energy distribution as a function of both the state of the laser (being on or off – corresponding to an accelerating mode excited or not excited) and the relative timing of the electron beam and laser pulse is measured. In order to find and optimize the acceleration signal, many parameters were varied.

1. The laser fluence is increased;
2. The tilt and rotation angles are varied;

3. The relative positioning of the electron beam and IR pulse is varied ;

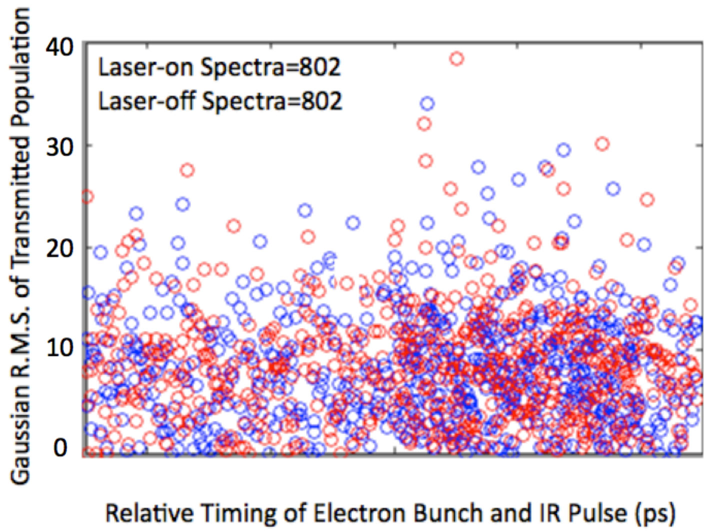

Figure 5.3: The width of the transmitted electron distribution as a function of the relative timing of the electron beam and the incident IR. Red dots correspond to the IR laser being on and blue dots correspond to the IR laser being off.

However, without filtering, the resulting data has a level of noise that can potentially bury any acceleration signal. Consider, for example, Figure 5.3. The laser-off (blue) shots show a variation in width of approximately 30 pixels (42 keV variation in width) in this data set. If there were an acceleration signal corresponding to a peak in Figure 5.3 that was smaller than 42 keV, it would be buried in noise and would likely go unobserved.

To reduce the noise level, the data is filtered by taking into account the sources of the noise. As the phase of the klystron-powered LINAC drifts over time while data is being collected, the energy spread of the beam increases. Using the width of the transmitted peak as a indicator of acceleration then becomes difficult. The electron bunches with increased energy spreads are indicated by their energy spectra, which have straggled glass populations with larger widths than usual when fitted to the hybrid Lorentzian-sech^2 discussed in section 5.2.1. An example of such a spectrum is on the left of Figure 5.4. By rejecting all of the data in which the width of the straggled glass population exceeds a user-specified threshold (typically 300 keV), the spectra with increased energy spread due to dephasing through the linac is eliminated from the data set.

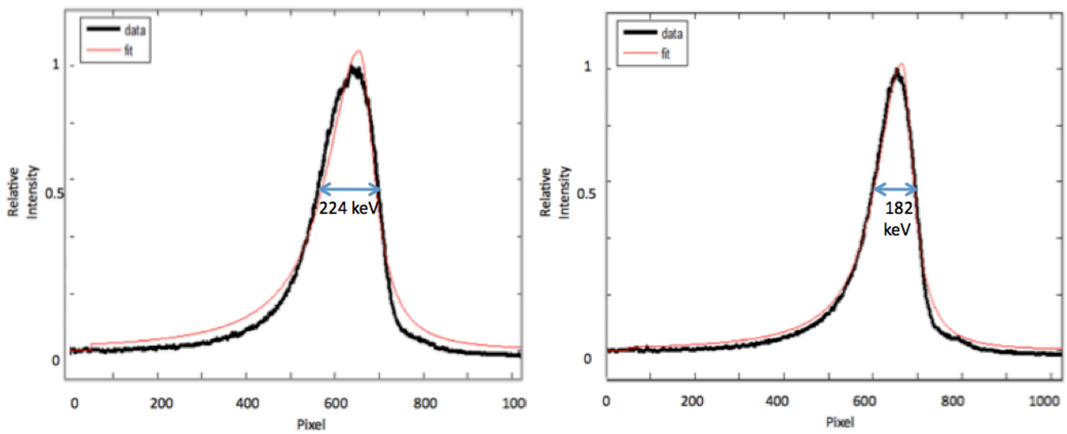

Figure 5.4: The energy spectrum of an electron beam that has traversed the LINAC upstream at a drifted phase (left) and at the optimal phase (right). Note that the straggled glass population in the left spectrum is wider than the same population on the right. These spectra are taken from Run 9.

Figure 5.5 shows that the peak position of the glass straggled peak varies by approximately 50 pixels, or 70 keV, while data is being collected, indicating an energy jitter of 70 keV. Due to the Dogleg described in section 4.2.1.1, there is a correlation between the energy of the electron beam and the location at which the electron beam hits the MAP. Moreover, the dispersion through the Dogleg leads to a low quality beam when the incident energy of the electron beam is not 60 MeV. As a result, when the energy jitters by large amounts, some of the electron bunches will degrade in quality and be steered away from the vacuum channel. The transmitted population is then lost. The peak position of the straggled glass

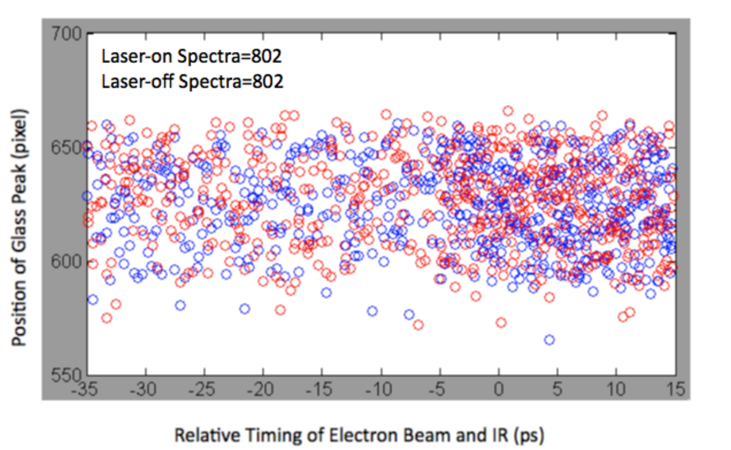

Figure 5.5: The peak of the portion of the electron distribution that has lost energy to the glass substrate as a function of the relative timing of the electron beam and the incident IR. Red dots correspond to the IR laser being on and blue dots correspond to the IR laser being off.

population serves as an indicator of the incident electron bunch energy, so that filtering the data based off of the position of the lower energy electron distribution removes this jitter-based source of noise. Typically, the spectra in which the peaks of the straggled population lie outside of a user-specified 15 keV-wide range are rejected.

With the spectra resulting from the dephasing and energy jitter of the electron beam filtered out of the data set, the noise level of the data set is reduced from a FWHM of 38 keV in Figure 5.3 to a FWHM of 20 keV in Figure 5.6. Figure 5.6 displays the width of the gaussian fitted to the transmitted population of the energy spectra for a series of data points (taken during Run 9) after filtering has taken place.

With this filtering included, there is a region in Figure 5.6 between -12 ps and -2 ps in which 7 laser-on spectra have wider transmitted populations than any other spectra in that region. With no laser illumination, the transmitted peak has an average width of 8 pixels, with a standard deviation of 8 pixels. Figure 5.6 shows the mean of the laser-off data and the widths corresponding to 1, 2, and 3 standard deviations above the mean. With the laser on, there are seven data points between -12 and -2 ps that are at least one standard deviation above the mean, with a maximum increase of more than 3 standard deviations (hereafter also known as 3σ).

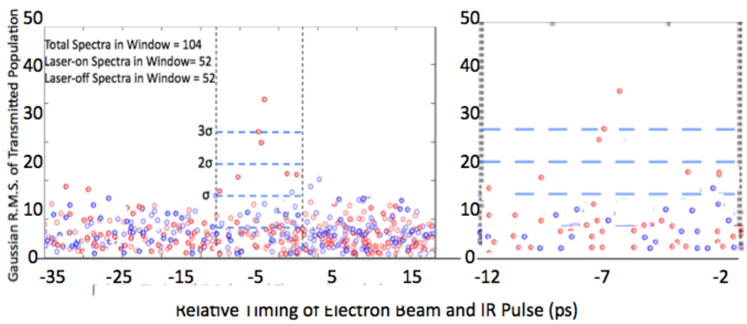

Figure 5.6: The width of the transmitted electron population versus the relative timing of the IR and electron beam. Laser-on data are red dots and laser-off data are blue dots. The lines denoted by σ represent the mean of the laser-off data plus 1, 2, and 3 standard deviations of the laser-off data. The zoomed in region of interest is highlighted in the image on the right. Data was collected during Run 9.

The maximum width of the transmitted population for this spectra is 42 pixels (more than 3 sigma higher than the laser-off mean value) and occurs at a relative timing of -6 ps. This pixel width corresponds to a transmitted population r.m.s of 59 keV. Subtracting the mean of the transmitted population widths of the laser-off data (8.4 keV) yields an energy broadening of 50.6 keV. The spectrum at which this broadening occured is given in Figure 5.7. The incident laser fluence at which breakdown is expected for the MAP Design 2 is 0.1 J/cm^2.

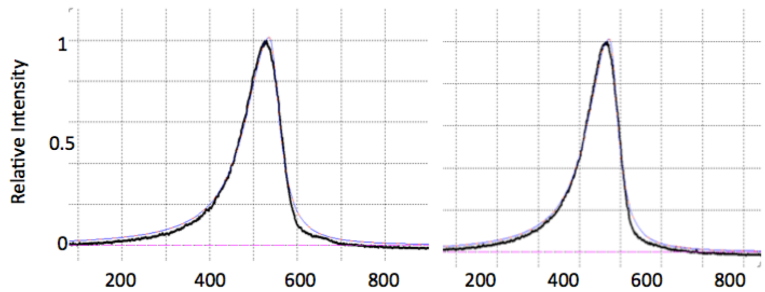

Figure 5.7: Energy profiles of electron bunches collected during Run 9 with no resonant mode excited (left) and with the resonant mode excited (right). The broadening of the transmitted population on the right is indicative of acceleration.

While the data in Figure 5.6 was being taken, the incident fluence of the IR laser was 0.027 J/cm^2, corresponding to an incident peak electric field amplitude of 25 MV/m. Since the simulated MAP design has an enhancement factor of 5.72 (see Table 3.5), the maximum electric field amplitude of the standing wave resonance is 142.4 MV/m and the resulting maximum energy gradient of accelerated electrons is 71.2 MeV/m. Discrepancies between the energy gradient of the fabricated sample and the simulated ideal design result from the reduced enhancement factor and shifted resonant frequency of the fabricated sample. The reduced enhancement factor and shifted resonant frequency are caused by differences between actual fabricated parameters and the ideal design parameters (see section 3.3.7). Moreover, the partial occlusion of the vacuum cavity, described in section 5.3, results in a reduction of the energy imparted to the passing electron beam.

Ideally, the region in Figure 5.6 suggestive of acceleration would have the profile given in Figure 5.8. In Figure 5.8, all of the laser-on data has larger widths than the laser-off data when the relative timing of the IR and electron beam is between 7.5 and 10.5ps. The laser-on data fits to a sech^2 function, as expected for electrons being accelerated by a standing wave [28]. However, the region between

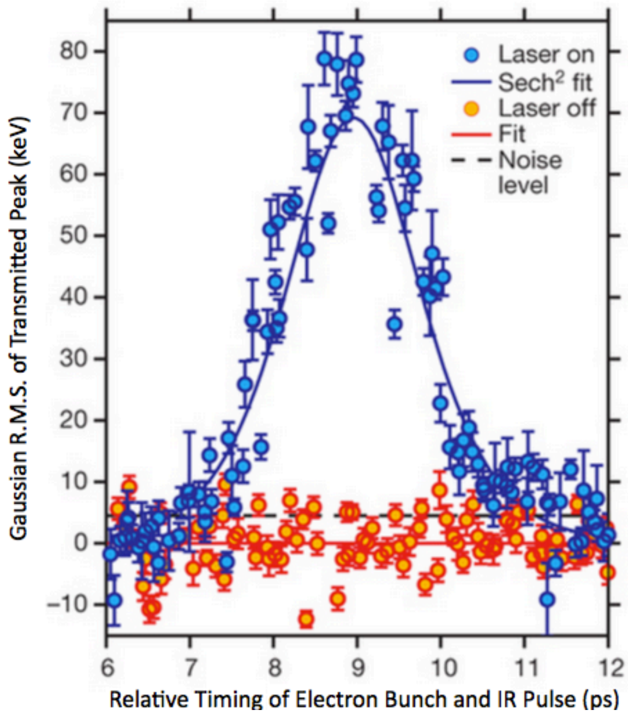

Figure 5.8: The gaussian r.m.s. of the transmitted population of electrons for an electron beam traversing the grating structure described in section 1.3.1.3 with the laser illuminating the structure (orange) and the laser off (blue). The laser on data fits to a sech^2 function, as is expected for electrons being accelerated by a standing wave [28]. This Figure is taken from Figure 3a of Ref. 21.

-12 ps and -2 ps in Figure 5.6 has many laser-on (red) data points that have transmitted population widths smaller than those of the 7 data points suggestive of acceleration in that region and as a result, a sech^2 function does not fit well to the laser-on data. To check whether this phenomenon could be caused by a flaw in the fitting algorithm, each spectrum was examined manually, yet there was no obvious flaw in the fitting algorithm that could explain the presence of laser-on shots with lower transmitted population widths in the region suggestive of acceleration. On the other hand, the 7 laser-on spectra were collected at nearby wall-clock times (before event 150 in Figure 5.9, while the lower width laser-on spectra were recorded minutes later during the data collection. It is possible that degradation of beam quality over time, evident in Figure 5.9, resulted in the lower widths of transmitted populations in laser-on spectra. Therefore, the data set in

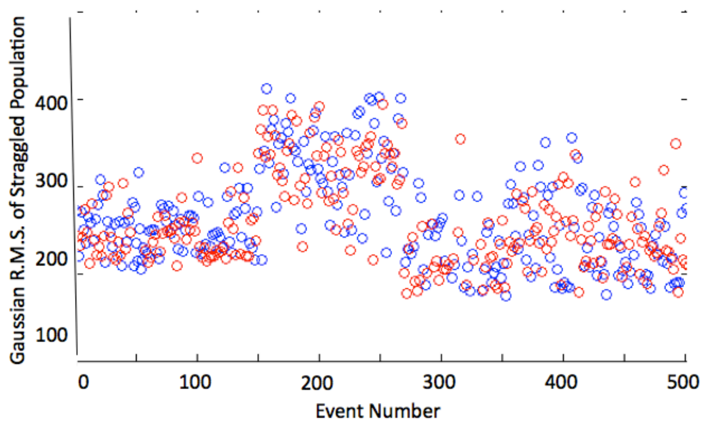

Figure 5.9: The gaussian r.m.s. of the straggled populations of electrons (that had lost energy to the glass). As data was collected the event number increased from 1 to 528 in this data set. Between event numbers 150 and 250, the width of the straggled population increases, indicating a degradation in beam quality. Although this is corrected after event 250 through beam tuning, there are many events with widths indicative of beam degradation after event 250.

Figure 5.6 is suggestive of acceleration with a confidence of 99%.

5.2.3 The Spatial Overlap of the Electron Beam and the IR Pulse

Spatial overlap of the laser and electron beam strongly affects the effective accelerating gradient and was investigated as a possible means to strengthen the signal of acceleration. As is described in section 4.2.2.3, the reflections of the

IR pulse on the MAP sample, as viewed by a camera focused on the back of the MAP sample, are spatially overlapped with the OTR signal generated when the electron beam strikes the MAP. Spatially overlapping these two signals via the camera image shown in Figure 4.11 ensures that the spatial overlap of the electron beam and IR pulse is accurate to within the spot size of the IR pulse, 100 microns. To find an optimal spatial alignment of the election beam and the IR, the position where the IR pulses hit the MAP was discretely varied over a range matching the uncertainty of the spatial overlap (100 μm) in increments of 25 microns. For each laser position, the mean ($\overline{blue}$) and r.m.s. (σ) of laser-off transmitted population widths in the window between -12 and -2 ps as well as the mean of the laser-on transmitted population widths ($\overline{red}$) in that same window are recorded. The parameter K is defined as:

$$K = \frac{\overline{red} - \overline{blue}}{\sigma} \tag{5.1}$$

The parameter K serves as a figure of merit for each set of data insofar as it indicates if the transmitted population widths in the electron energy spectra are significantly larger when the laser is on compared to when it is off, relative to the noise level of the laser off data. If acceleration causes an increase of transmitted population widths in a specific time range, an increase in the calculated K in that range will reflect that increase in population width.

As seen in Figure 5.10, the figure of merit K was only significantly greater than zero for one position of the laser: the position at which the cross-correlation data in Figure 5.6 was taken. Changing the relative position of the laser and the electron beam weakened the acceleration signal by an order of magnitude. Since both the electron beam and the laser spot have a transverse σ of 21 microns in the x-dimension, the acceleration signal is expected to be reduced by a factor of

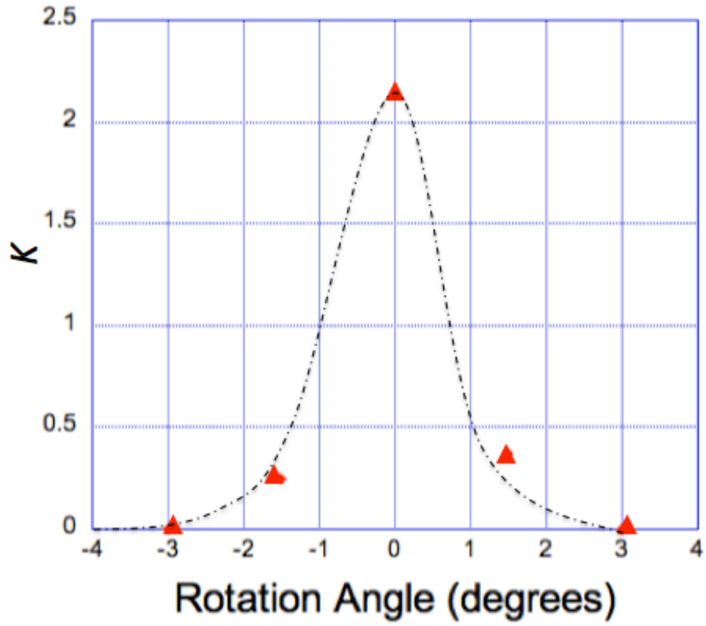

Figure 5.10: The figure of merit K as a function of the relative spatial overlap of the laser and electron beam. At an overlap of 0 microns, the strongest acceleration signal is seen. This corresponds to the data set in Figure 5.6

1.4 when the laser is misaligned with the electron beam by 20 $/microns$. The experimentally observed reduction is larger than he expected reduction due to potential beam degradation as well as the method in which the laser was steered onto the sample. By rotating the mirrors above the sample so that the IR hit the sample at a different spot, perpendicularity of the IR path and the sample surface is compromised. This will reduce the acceleration signal more than a spatial misalignment of the IR and electron beams would alone.

5.2.4 Rotation and Tip of the the MAP Sample

The angular orientation of the MAP has a significant impact on the ability of the standing wave resonance generated in the MAP to accelerate electrons. If the rotation of the sample is misaligned so that the electron beam does not travel perpendicularly to the coupling slots, the effective wavelength of the standing wave resonance is longer than 800nm and synchronous acceleration does not occur. To achieve 50 keV of energy gain for an incident laser with a fluence of 0.027 J/cm^2, the MAP sample cannot be misaligned by more than 3 degrees in rotation. The MAP is aligned by eye when the sample is first installed onto the actuator stage described in section 4.2.1.1. During data collection, the rotation of the actuator stage is varied over a window of 6 degrees in steps of 1.5 degrees to ensure that optimal alignment is achieved. Varying the rotation value of the stage 1.5 degrees away from the the value it was at when the data in Figure 5.6 was taken reduces K by a factor of 5 in Figure 5.11. The optimal orientation of the sample is thus confirmed to be its rotation in Figure 5.6

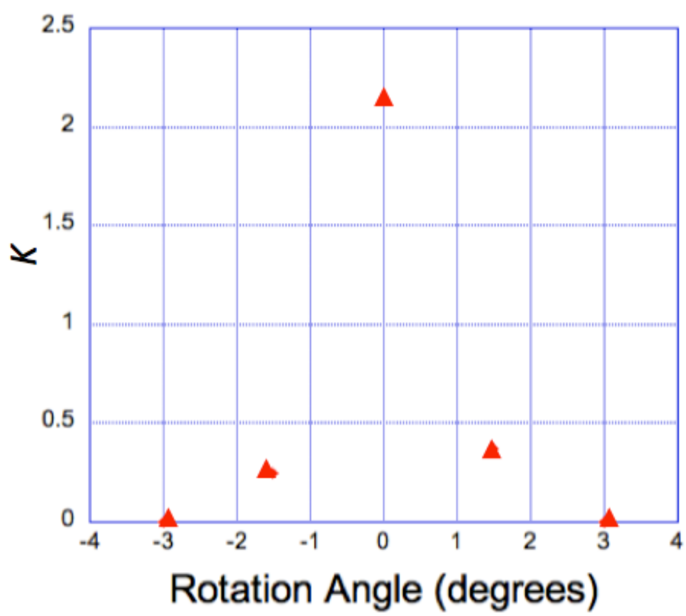

Figure 5.11: The figure of merit K as a function of the rotational orientation of the MAP sample. At an rotation of 0 degrees, the strongest acceleration signal is seen. This corresponds to the data set in Figure 5.6

Additionally, aligning the tip angle of the MAP sample relative to the incident IR and electron beam is crucial for achieving acceleration. For reasons elaborated on in section 4.2.2.4, if the top surface of the MAP sample is misaligned by 0.01 degrees or more so that it is not perpendicular to the incident IR, acceleration does not occur. To measure whether perpendicularity of the MAP sample to the incident IR is achieved to within tolerance, the incident IR is sent through a beam splitter and onto a screen where it is aligned with the IR reflected from the top surface of the MAP, as is described in section 4.2.2.4. The two spots are aligned by adjusting the orientation of mirrors in the IR path, ensuring perpendicularity to within tolerance. When the tip angle was varied, Figure 5.12 shows that K was essentially zero except at the nominally perpendicular position found during initial alignment, at which the cross-correlation data in Figure 5.6 was taken. As expected, the strength of the acceleration signal is sensitive to a tip variation of as little as 0.01 degrees. Moreover, the acceleration signal's strength drops off as quickly as predicted by the analysis in section 4.2.2.4, indicated by the dotted line in Figure 5.12.

5.2.5 Fluence of the Incident IR

Increasing the fluence of the laser should increase the width of the transmitted population in the electron energy spectra downstream of the MAP sample, since the amplitude of the accelerating mode increases with the increased fluence. However, there was no suggestion of acceleration in the energy spectra in Figure 5.13 when the IR fluence was increased from 0.027 to 0.071 J/cm^2, even though the amplitude of the accelerating mode should have increased by a factor of 9 since the electric field scales as the fluence squared. The mean and r.m.s. of the widths of the transmitted populations in the laser-off spectra in Figure 5.13 are

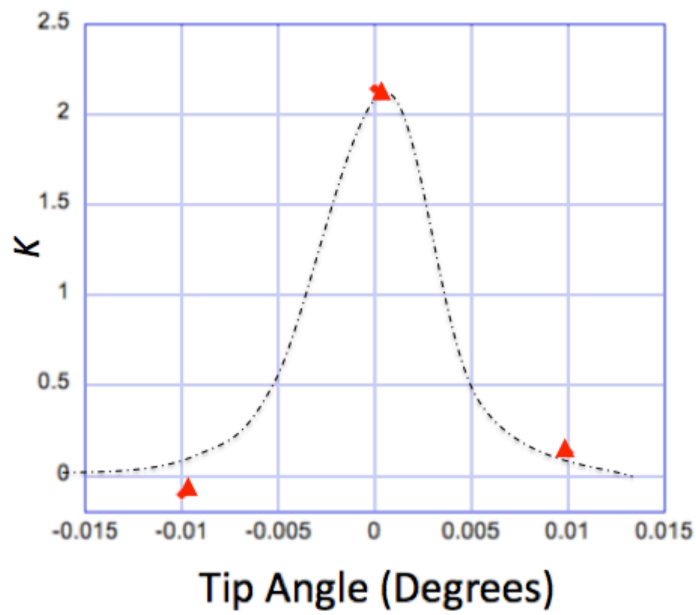

Figure 5.12: The figure of merit K as a function of the tip orientation of the MAP sample. At an tip of 0 degrees, the strongest acceleration signal is seen. This corresponds to the data set in Figure 5.6. The dotted line shows the calculate acceleration signal strength based on the analysis in section 4.2.2.4.

12 and 15 respectively. No laser-on spectrum has a transmitted population width more than one sigma greater than the mean of the laser-off spectra transmitted population widths.

The data in Figure 5.13 was performed hours after the data in Figure 5.6 was taken and the beam quality degraded during this time, as indicated by the increase in the mean of the transmitted population widths for the laser-off spectra. Furthermore, increasing the fluence of the incident IR may have damaged the dielectric materials composing the MAP sample, rendering the resonance (and thus any acceleration) nonexistent. Although the breakdown threshold of the sample was calculated to be 0.1 J/cm^2 based on simulations, deformities in the deposited layers may have resulted in field enhancement and breakdown around these irregularities. Post-run inspection of the MAP sample revealed evidence of breakdown near the horizontal region of the MAP where the data was taken in Figure 5.13. This breakdown is evident in the Figure 5.14.

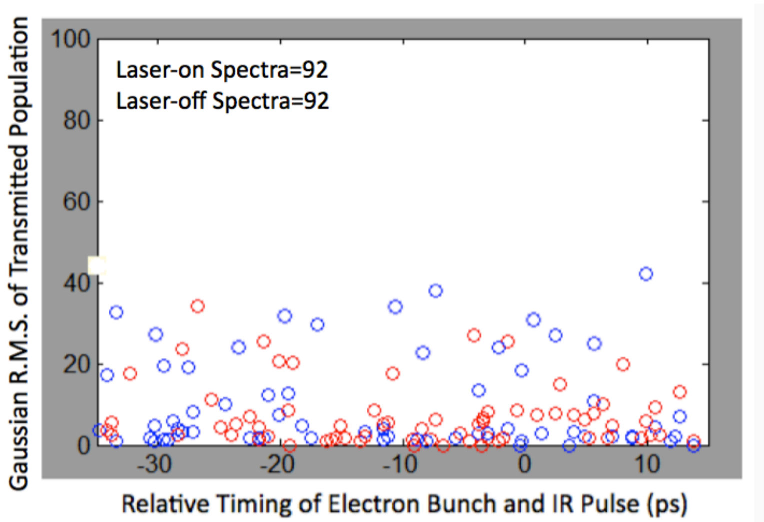

Figure 5.13: The width of the transmitted electron population versus the relative timing of the IR and electron beam. Laser on data are red dots and laser-off data are blue dots. The fluence of the incident IR is .071 J/cm^2.

5.3 Summary and Discussion

Indications of acceleration were observed with two different MAP samples. The sample used in Run 6 in Table 5.1 had multiple electron energy spectra (an example of which is shown in Figure 5.1) with transmitted populations exhibiting the "double-horn" distribution characteristic of acceleration due to a standing wave (see section 3.4.2). Regardless, no correlation between evidence of acceleration in the electron energy spectra and the voice coil stage position (i.e. the relative timing of the IR and the electron beam) was found for this MAP sample.

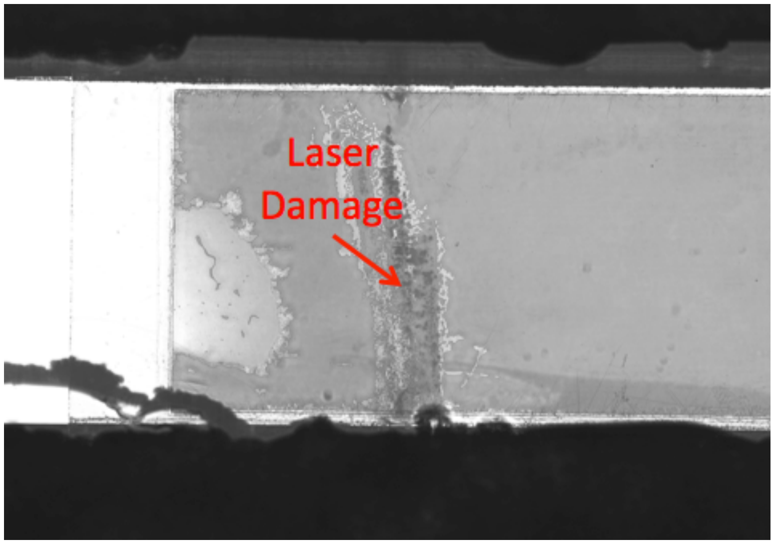

Figure 5.14: An optical microscope image of the top surface of the MAP sample tested in Run 9. Damage due to high-fluence IR exposure is evident.

This is accounted for by two effects. First, as data was being taken, the quality of the beam degraded as its energy upstream of the MAP drifted. Recall that the strong dispersion in the dogleg of the NLCTA leads to emittance growth and pathological beam behavior as the energy of the electron beam exiting the LINAC drifts away from 60 MeV. Second, as the MAP sample is subjected to many IR pulses, the probability that dielectric layers of the MAP break down increases [46]. A MAP sample with ablated dielectric layers cannot generate a resonance and thus cannot accelerate electrons. It is likely that while a correlation between an acceleration signal and the relative timing of the laser and electron beam was searched for, beam degradation and laser-induced ablation had already occurred, rendering the search futile.

In an effort to find a correlation between an indication of acceleration in the electron energy spectra and the relative timing of the IR pulse and electron beam, a the MAP sample used in Run 9 in Table 5.1 (with the parameters specified in Table 4.1) was tested at the NLCTA. In Figure 5.6, it is evident that there is a region of voice coil stage positions in which the width of the transmitted population in the electron energy spectra was larger when the MAP was illuminated with IR than when it was not illuminated. The broadening of the transmitted population in this region (evident in Figure 5.7 suggests a maximum accelerating gradient of 50.6 MeV/m, whereas simulated results taking into account the incident laser fluence and enhancement factor of the structure suggest a maximum accelerating gradient of 71.2 MeV/m. This deviation, like with the previous sample, can be partially accounted for by differences in the fabricated MAP sample and the ideal design in Table 3.4 and the resulting shift of the sample's resonant frequency and reduction in enhancement factor.

Additionally, the occlusion of the vacuum cavity reduces the energy gradient. The energy spectra of the electrons traversing the MAP sample in Figure 5.2 exhibit an energy difference of 200 keV between the transmitted and glass-straggled populations, less than the energy difference of 300 keV that is predicted by Geant 4 simulations for an electron bunch scattering through 1mm of Fused Silica (see section 3.4.2). This discrepancy is likely due to partial occlusion of the vacuum cavity of the MAP in z. As the MAP is diced to form the samples described in Section 4.1.1.3, the dicing saw can tear part of the dielectric layers resulting in partial blockage of the vacuum channel. As a result, electrons traversing the vacuum cavity will lose energy to the dielectric blocking the cavity and the energy separation between the transmitted population and the straggled glass population is reduced. This vacuum cavity blockage is evident in post-run images of the sample, one of which is shown in Figure 5.15.

The region over which the transmitted electrons see an accelerating mode is reduced to the section of the MAP without dielectric material blocking the cavity,

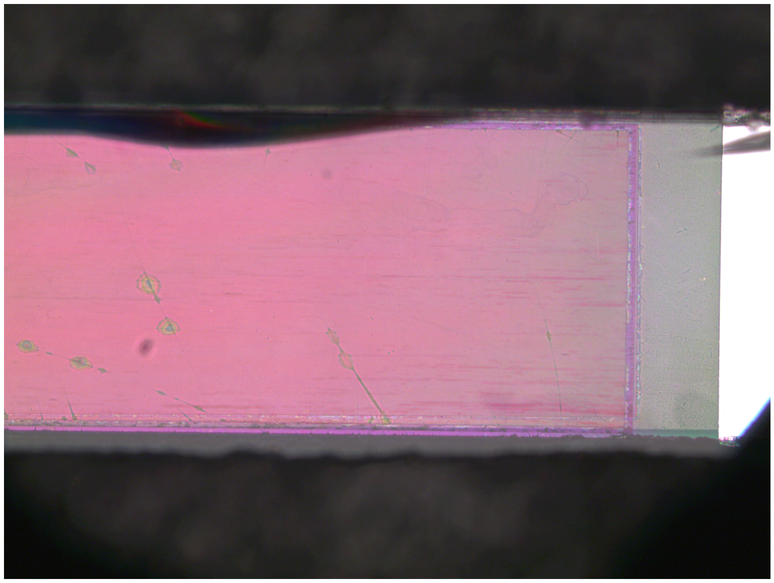

Figure 5.15: An optical microscope image of the top surface of the MAP sample tested in Run 9. The missing DBR (the top section of the sample in which only a transparent substrate is visible) and darkened region to the left are indicative of the occlusion of the vacuum cavity caused by the dicing process.

resulting in a reduced energy modulation of the electron beam. The energy difference of 200 keV between the transmitted and glass-straggled populations suggest that roughly 350 μm of the 1 mm long accelerating cavity is blocked by dielectric. For a 650 μm long MAP (corresponding to the length of the accelerating channel not blocked by dielectric) illuminated by a incident laser with a fluence of 0.027 J/cm^2 and a pulse length of 5 ps, VORPAL predicts that electrons traversing the vacuum cavity see a maximum energy gain of 46.3 keV. This simulated energy gain is 7.5 % different than the measured energy gain, a discrepancy that can be accounted for by the uncertainty in the length of the cavity that is occluded (15 %).

Attempts to increase the accelerating gradient by varying the spatial overlap of the laser and electron beam, and the angular orientation of the sample demonstrated that the initial alignment of the MAP sample in Run 9 was optimal. The strong dependence of the accelerating gradient on the tip of the sample is expected due to the induced dependence of the standing wave phase on the longitudinal coordinate z that a tip introduces. The dependence of the accelerating gradient on the spatial overlap can be explained by noting that if the laser and electron beam are misaligned, the amplitude of the resonance in the region that the electron beam passes is reduced. Though this is not modeled in simulation, the fact that the accelerating gradient is only 50 MeV/m when the two beams are aligned suggests that any reduction in this gradient could "bury" the accelerating signal in the noise of data plots such as that in Figure 5.3. The dependence of the accelerating gradient on the rotation angle can be similarly explained by a reduced energy imparted to electrons.

Varying the fluence of the incident IR did not increase the number of data points suggestive of acceleration or the energy gain of those spectra indicative of acceleration. The higher laser fluence spectra were collected hours after the spectra in Figure 5.6 were recorded, after the electron beam phase had slowly drifted for hours and the MAP sample had been exposed to thousands of IR pulses. Thus, the lack of broadening in the high fluence spectra is likely accounted for by beam quality degradation due to the strong dispersion in the dogleg (shown in Figure 5.9) as well as ablation of the dielectric layers due to laser-induced breakdown (shown in Figure 5.14).

5.4 Conclusion

The simulation, analytical, fabrication and experimental efforts described in this dissertation led to the first observation of acceleration in a resonant DLA. This encouraging result furthers confidence in the viability of DLA's as vehicles for compact high-gradient acceleration.

Extensive analytical and computational work led to the fabrication of a MAP design that was tested at the NLCTA facility at SLAC. An extensive iterative interaction between simulation and fabrication efforts led to a design of the MAP that had a strong resonance and a design that was practical to fabricate. Though early signs of acceleration with an energy gradient of 50.6 MeV/m, described in section 5.2, were encouraging, much work remains to increase the accelerating gradient of the MAP as well as the confidence in the acceleration signal. Several specific areas for future work are described below.

As is mentioned in section 3.3.7, the error tolerances on the thicknesses of the various MAP layers are on the order of a few nanometers and the error tolerances on the indices of refraction for the materials composing these layers is on the order of one hundredth. Fabricating a structure with dimensions within these error tolerances with the sputtering techniques described in section 4.1 is challenging and in the future, atomic layer deposition may need to be used instead. Alternatively, a variant of the MAP that is not as sensitive to deviations in layer thicknesses and material indices can be designed. For instance, if the number of dielectric pairs in the DBR's of the MAP is reduced, the sensitivity to deviations in their thicknesses will be reduced, although the confinement of the accelerating mode (and thus the enhancement factor) will also be reduced.

However, even with the current MAP design and fabrication techniques, the ability to measure the frequency at which a given MAP sample resonates would be both informative and helpful. As is described in section 5.1.1, the resonance of the MAP was not detected using the spectrophotometer set-up at UCLA. If this experimental set up was changed so as to include a coherent source (e.g. a small bandwidth laser with a tunable central wavelength) and a spot size that is better suited to a sub-mm scale sample, the potential to measure the resonance in the MAP would increase. If the resonant frequency of the MAP were observable, not only would the confidence in the MAP's ability to resonate be increased, but MAP samples that resonate at frequencies that are better suited for synchronous acceleration (i.e. frequencies close to the speed of light divided by the structural period) could be selected for acceleration tests.

Finally, improving the quality of the electron beam that is used to look for acceleration in the MAP would increase the probability of observing a strong sign of acceleration for electrons traversing a MAP sample. Although the electron beam at the NLCTA made the experimental search for acceleration in the MAP possible, if there were a facility capable of producing a beam small enough and with a low enough emittance to traverse the 400nm tall vacuum cavity of the MAP without scattering through the surrounding DBR and short enough to see only accelerating phases (i.e. shorter than 200nm), the signal to noise ratio of the potentially accelerated transmitted population would increase as the transmitted population would no longer be on the tail of the straggled glass population in the energy spectra (as it is in Figure 5.2).

Though there are many ways to improve the accelerating gradient of the MAP, experimental evidence that the MAP can accelerate electrons is nonetheless encouraging. This result, combined with the experimental evidence of acceleration shown in the grating structure described in section 1.4.4, indicates that Dielectric Laser Accelerators are indeed candidates for compact high-gradient acceleration. By combining DLA's with subrelativistic capture sections and electron sources such as those described in section 1.3.3 can lead to the use of DLA's as stand-alone particle sources. The new regime that these structures will make available may lead to new scientific discoveries in attosecond sciences, particle physics and medical physics.

CHAPTER 6

Addendum

The monolithic MAP (described in section 1.3.3) makes many of the applications discussed in section 1.5 possible. The region of the monolithic MAP that captures electrons emitted from the wedge emitter and accelerates these electrons to relativistic energies (hereafter referred to as the sub-relativistic region introduces a few problems that must be addressed in order to finalize its design.

6.0.1 Particle Dynamics in the Sub-Relativistic Regime

6.0.1.1 Transverse Defocusing

When an electron is traveling along the standing wave resonance (described in section 1.3.2) in a longitudinally stable phase that is also accelerating ($k_z z \in [0, \pi/2]$) then it is at a phase where the transverse forces defocus electrons away from the beam axis (see section 2.2.2). A scheme that addresses this issue and attempts to counteract it is now presented.

6.0.1.2 Phase Dithering

To remedy the transverse defocusing of electrons in the accelerating cavity of the MAP, a scheme is proposed in which the positions of the coupling slots are modulated in the direction of electron propagation.

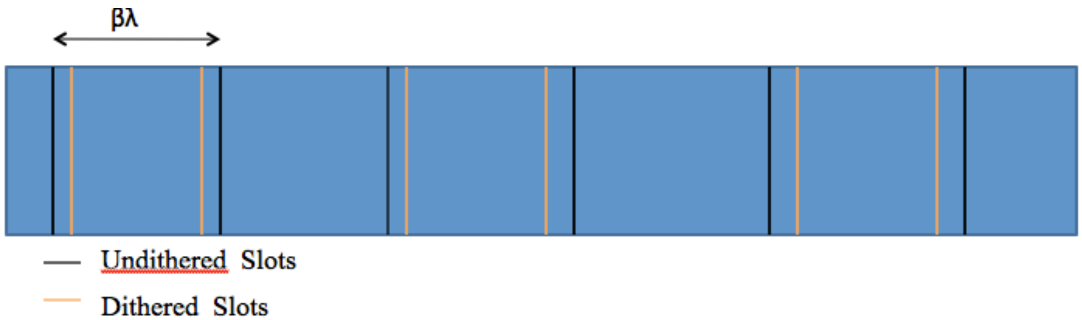

Figure 6.1: A top-down image of the sub-relativistic map. The black lines correspond to the slot positions in the original design, placed $\beta_s\lambda$ apart, where β is v/c and λ is 800 nm. The orange lines correspond to the new dithered positions.

This modulation has a periodicity denoted by λ_p. In the figure below, this periodicity corresponds to $2\beta_s\lambda$ (note that the coupling slot periodicity in the unmodulated design is $\beta_s\lambda$). The intended effect of the modulation is that the on-crest "phase" of the standing wave oscillates about a central phase as formulated in Equation 6.1:

$$\phi_s = \phi_0 + \phi_m \sin[k_p z]. \tag{6.1}$$

In the above equation, ϕ_s is the phase of the crest of the standing wave at times that are multiple of the optical cycle of the incident laser. For instance, if the slot modulation causes the position of the crest to shift backwards in z by 10 nm, then $\phi_s = 2\pi\frac{-10nm}{800nm}$. ϕ_0 is the central phase, ϕ_m is the oscillation amplitude and $k_p = 2\pi/\lambda_p$.

The transverse force seen by the electron is

$$F_y = \frac{qE_0}{\gamma}\sinh[\frac{k_z y}{\gamma}]\sin[\phi]. \tag{6.2}$$

Here, ϕ is the phase of the standing wave seen by the electron. Assuming that

$\frac{d\beta}{dz} \approx 0$, the Equation of motion in the transverse direction becomes

$$y'' = \frac{qE_0}{\gamma^2 mc^2 \beta^2} \sinh\left[\frac{k_z y}{\gamma}\right] \sin[\phi], \tag{6.3}$$

where ” denotes the second derivative with respect to time. For an electron near the axis ($k_p y \ll 1$) Equation may be simplified to

$$y'' = \Lambda \sin[\phi_0 + \phi_m \sin[k_p z] + \Delta\phi] y; \tag{6.4}$$

$$\Lambda = \frac{qE_0 k_z}{\gamma^3 mc^2 \beta^2}; \text{and} \tag{6.5}$$

$$\Delta\phi = \phi - \phi_s. \tag{6.6}$$

Trignometric expansion yields

$$y'' = \Lambda[\sin\phi_p \cos[\phi_m \sin[k_p z]] + \cos\phi_p \sin[\phi_m \sin[k_p z]]] y; \text{with} \tag{6.7}$$

$$\phi_p = \phi_0 + \Delta\phi. \tag{6.8}$$

The transverse displacement y can be decomposed into a quickly oscillating part y_{osc} and slowly evolving secular part y_{sec}, with $\|y_{osc}\| \ll \|y_{sec}\|$:

$$y''_{sec} + y''_{osc} = \Delta[\sin\phi_p \cos[\phi_m \sin[k_p z]] + \cos\phi_p \sin[\phi_m \sin[k_p z]]] y_{sec} \tag{6.9}$$

Additionally, $\Delta\phi$ can be decomposed into secular and oscillating parts such that $\|\phi_{osc}\| \ll \|\phi_{sec}\|$:

$$\phi_p = \phi_0 + \Delta\phi_{sec} + \Delta\phi_{osc} \approx \phi_0 + \Delta\phi_{sec}. \tag{6.10}$$

Define the term on the far right of Equation 6.8 as $\widetilde{\phi}$. Over suitable time scales $\ll y''_{osc} \gg= 0$, so y_{osc} can be identified with the second term in Equation 6.7:

$$y''_{osc} = \Lambda[\cos[\widetilde{\phi}] \sin[\phi_m \sin[k_p z]]] y_{sec}. \tag{6.11}$$

ϕ_m^3 is assumed to be negligibly small, and so the sin in Equation 6.9 is expanded to second order in ϕ_m:

$$y''_{osc} = \Lambda \phi_m y_{sec} \cos[\widetilde{\phi}] \sin[k_p z] + \Theta[\phi_m^3]. \tag{6.12}$$

Here, $\Theta[\phi_m^2]$ refers to all terms third order and above in ϕ_m. The solution to this equation can be found by making the reasonable assumption that y_{sec} remains constant over one period of oscillation of the much more quickly varying y_{osc}:

$$y_{osc} = -\Lambda \phi_m \cos[\widetilde{\phi}] \frac{\sin[k_p z]}{k_p^2} y_{sec}. \tag{6.13}$$

This result can be substituted into Equation 6.7, which can then be expanded to 2nd order in ϕ_m and averaged over one cycle of y_{osc}:

$$y''_{sec} = [\Lambda(1 - \frac{\phi_m^2}{4}) \sin[< \widetilde{\phi} >] - \frac{\Lambda^2 \phi_m^2}{2k_p^2} \cos[< \widetilde{\phi} >]^2] y_{sec}. \tag{6.14}$$

Note that $< \phi > = < \widetilde{\phi} >$ over one cycle of y_{osc} and henceforth the averaging brackets will be dropped.

$$y''_{sec} = [\Lambda(1 - \frac{\phi_m^2}{4}) \sin[\phi] - \frac{\Lambda^2 \phi_m^2}{2k_p^2} \cos[\phi]^2] y_{sec} \tag{6.15}$$

This equation can be evaluated using parameters relevant to the MAP's regime of operation. Note that:

$$\Lambda = \frac{\alpha k_z^2}{\gamma^3 \beta^2}. \tag{6.16}$$

In the above Equation, $\alpha = \frac{qE_0}{mc^2}$, typically on the order of 10^{-4}. For sub-relativistic electrons, typical energies of 25 keV lead to $\gamma \approx 1$ and $\beta \approx 0.3$. As a result, $\Lambda \approx 10^{-3}$. Equation 6.13 is then transformed into Equation 6.15.

$$y''_{sec} = [10^{-3}(1 - \frac{\phi_m^2}{4}) \sin[\phi] - \frac{10^{-6} \phi_m^2}{2k_p^2} \cos[\phi]^2] y_{sec} \tag{6.17}$$

$$= \Omega y_{sec} \tag{6.18}$$

As a numerical example, if $k_p = .037 * k_z$ and $\phi_m = 1\text{radian}$, then $\Omega = -1\mu m^{-2}$, so focusing occurs. Thus, the phase dithering scheme is a potential manner in which to compensate for phase defocusing in the sub-relativistic MAP.

6.0.2 Resonance in the Subrelativistic MAP

The resonance that can synchronously accelerate relativistic electrons has a wavelength matching the incident wavelength of the near-optical laser. However, this resonance cannot accelerate sub-relativistic electrons. As an example, consider an electron with a kinetic energy of 25 keV traveling through a MAP illuminated by a 800 nm laser (matching the wavelength of the Ti:Sapphire laser discussed in section 4.2.1.2). During one optical cycle of the incident laser ($2.\overline{6}$ fs), a 25 keV electron travels 240 nm. The electric field encountered by this electron during transit is illustrated below.

Since the electron encounters both accelerating fields and decelerating fields of the same magnitude, it's net energy gain is 0 over one optical cycle and no net acceleration occurs. To achieve ideal synchronous acceleration, a standing wave with a wavelength that matches the distance travelled by the electron in one optical cycle (240 nm) must be excited. However, efforts to create such a resonant mode have been unsuccessful, since HFSS simulations have repeatedly shown that when the coupling slots have a longitudinal periodicity of 240 nm, a standing wave accelerating mode is not excited. More generally, sub-wavelength diffraction is difficult to achieve, particularly with a partially transmissive phase mask such as the coupling slots in the MAP. Instead, only Fabry-Perot modes (such as those described in section 3.3.5) are excited. As a result, an alternative acceleration scheme was considered.

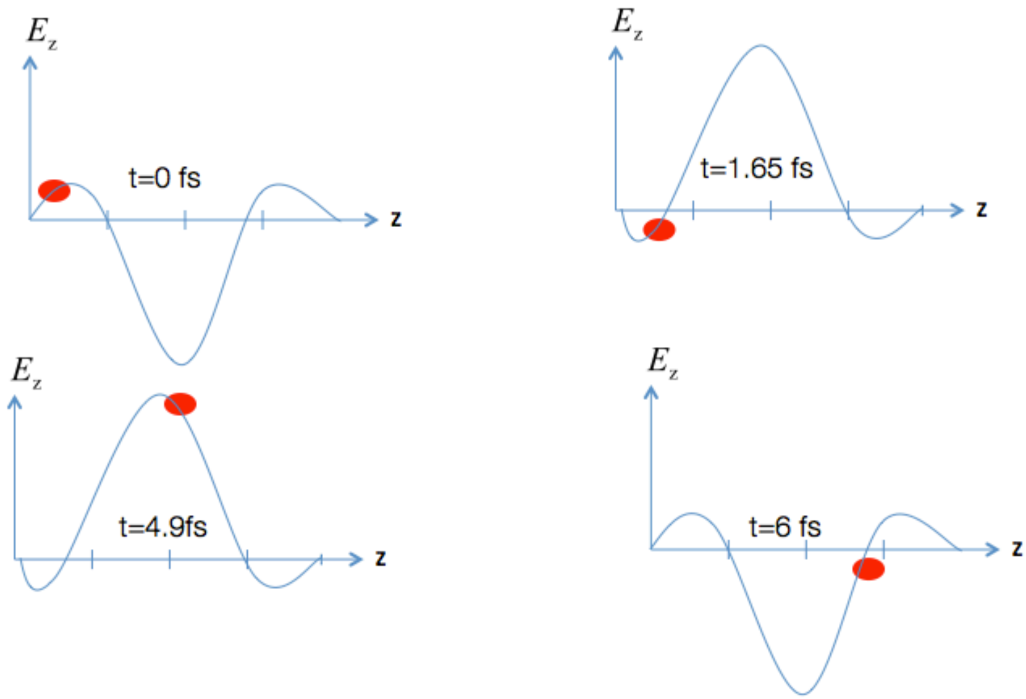

Figure 6.2: Four snapshots of the on-axis electric field seen by a sub-relativistic electron bunch when the standing wave accelerating mode has a 800 nm wavelength.

6.0.2.1 Period Skipping Scheme

This difficulty of exciting a sub-wavelength resonance can be avoided by considering a MAP structure whose coupling slot periodicity is a multiple of both λ and $\beta_s\lambda$. Since the coupling slot periodicity is a multiple of the incident wavelength, the structure can support a standing wave resonance with a wavelength matching the coupling slot periodicity. For the case in which the electrons have a kinetic energy of 25 keV, a 2.4 micron coupling slot periodicity is 10 times $\beta\lambda$ and 3 times λ. The key aspect of this standing wave resonance is due to the coupler periodicity being significantly larger than the wavelength of the incident laser. As a result, the field strength in the vacuum gap directly beneath the coupling slot is stronger than the field strength away from the slot as shown in the Figure 6.4.

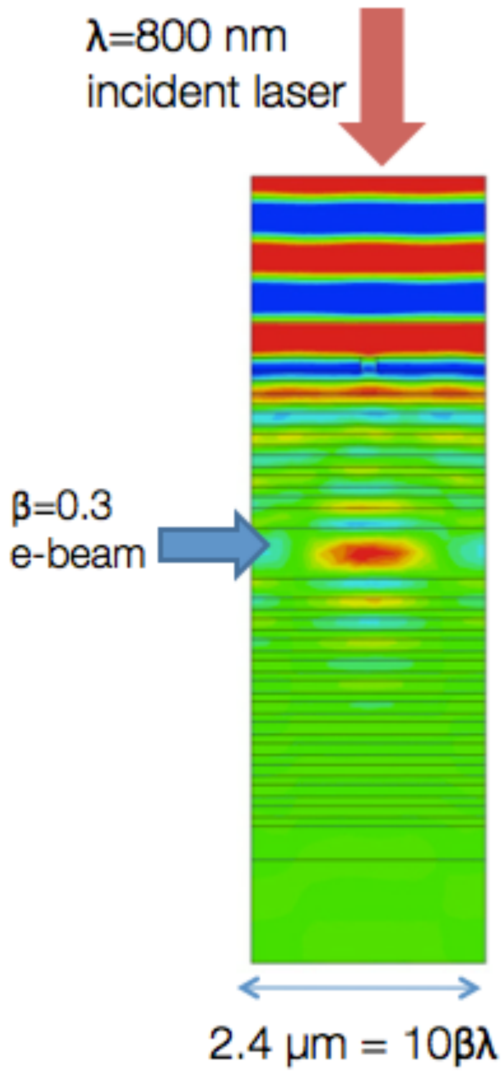

Figure 6.3: Cross sectional field overlay of fields excited in 2.4 micron period structure.

This mode shown in Figure 6.3 can be utilized to achieve net acceleration for a sub-relativistic beam. If injected electrons are phased in such a manner that they

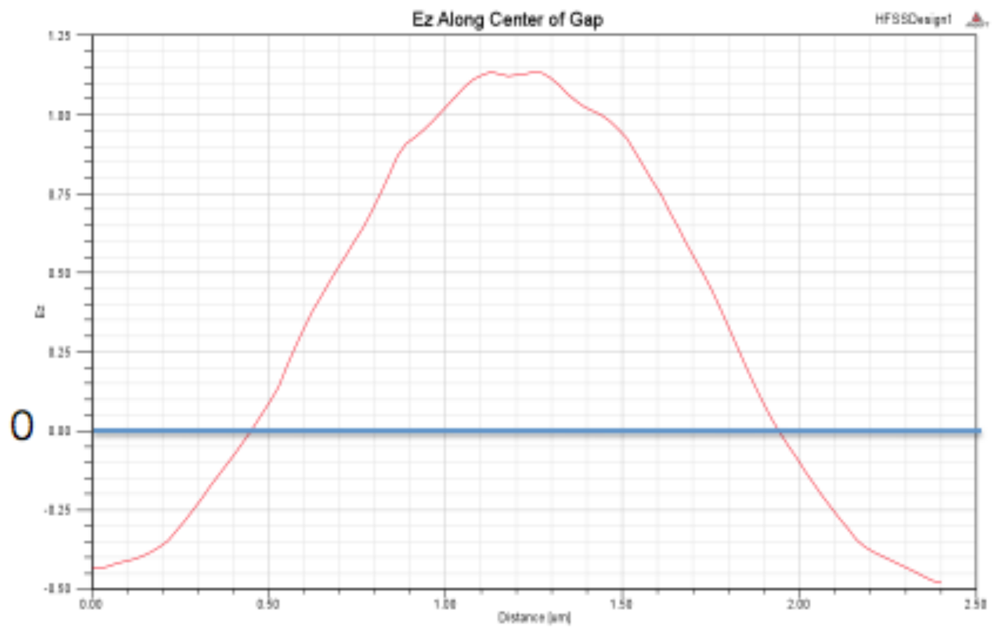

Figure 6.4: On axis fields for the newly proposed sub relativistic scheme.

pass under the coupling slots in each period when the resonating field is strongly accelerating, a net energy gain will occur. This is true even though the electrons will see decelerating fields away from the coupling slot, where the field strength is weaker. In fact, the energy gained when the particle sees an accelerating electric field is greater than the energy lost when the particles sees a decelerating field and as a result, there is a net gain of energy. This scheme, motivated by work by Ming Xie [11], is illustrated below.

VORPAL (a simulation program described in Chapter 3) was used to simulate energy gain in this scenario, in which an energy gain of 100 keV was found after an electron bunch travelled 250 microns in the capture section, illuminated by a 1 GV/m peak amplitude Ti:Sapphire laser. Energy histograms showing this energy gain are given below.

Though work remains to implement this scheme into a fabricated device,

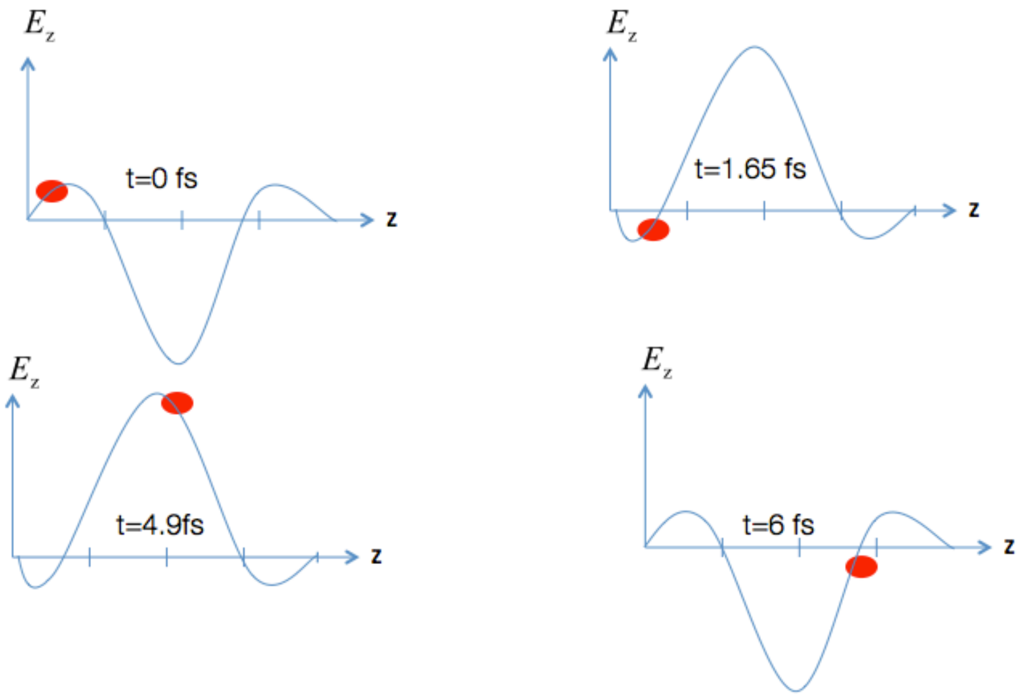

Figure 6.5: Snapshots in time showing method in which electrons are accelerated by the distorted standing wave resonance.

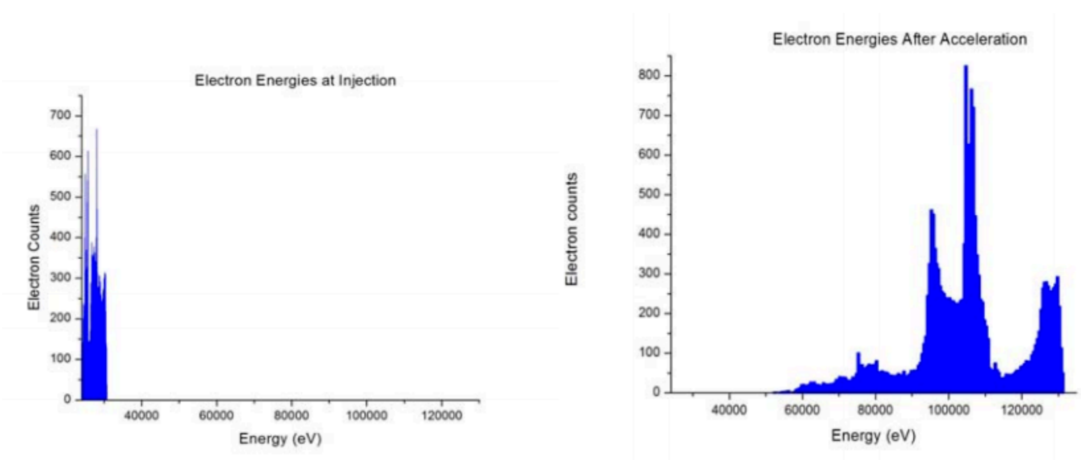

Figure 6.6: Energy spectrum of electrons before and after having travelled through 250 microns of a structure designed to accelerate 25 keV electrons.

this VORPAL result, showing an energy gradient of 0.4 MeV/m, suggests that acceleration in the sub-relativistic capture section is possible.

References

[1] "CERN faq: LHC The Guide." cds.cern.ch/record/1165534/files/CERN-Brochure-2009-003-Eng.pdf. Accessed 12/01/13.

[2] J. Skrabacz, "Optimizing Cost and Minimizing Energy Loss in the Recirculating Race-Track Design of the LHeC Electron Linac," CERN REU, 2008.

[3] T. Tajima and J. M. Dawson, "Laser Electron Accelerator," Phys. Rev. Lett. 43, 267270 (1979).

[4] B.Ghosh and K.P.Das,"Modulational instability of Electron Plasma Waves in a Cylindrical Wave Guide," Plasma Phys. Control. Fusion 27, pp.969 (1985).

[5] R. J. England et al., "Dielectric Laser Accelerators," Review of Modern Physics (to be published).

[6] Widere, R. (17 December 1928). "On a New Principle to Produce High Voltages." Archive for Electronics and Uebertragungstechnik Vol.21, No.4, 387(1928).

[7] E. L. Ginzton, W. W. Hansen, and W. R. Kennedy, "A Linear Electron Accelerator", Rev. Sci. Instrum.19, 89-108 (1948).

[8] M. Chodorow, E. L. Ginzton, W. W. Hansen, R. L. Kyhl, R. B. Neal, W. K. H. Panofsky et al., "Stanford High-Energy Linear Electron Accelerator (Mark III)", Rev. Sci. Instrum.26 ,134-204 (1955).

[9] D. E. Nagle, E. A. Knapp, and B. C. Knapp, "Coupled Resonator Model for Standing Wave Accelerator Tanks", Rev. Sci. Instrum. 38,1583-1587 (1968).

[10] D.H. Whittum, "Introduction to Electrodynamics for Linear Particle Accelerators." SLAC-PUB,-7802 (1998).

[11] M.Xie, "Principle of Alternating Gradient Acceleration," Proceedings of the European Particle Accelerator Conference, IEEE, Vienna (2000).

[12] B.C. Stuart et al. "Nanosecond-to-femtosecond laser-induced breakdown in dielectrics." Phys. Rev. B 53(1996).

[13] V.A. Dolgashev, S.Tantawi, "RF Breakdown In X-Band Waveguides," Presented at the 8th European Particle Accelerator Conference (EPAC 2002), 6/3/2002 - 6/7/2002, Paris, France.

[14] "TI Sapphire Laser Kits." www.dmphotonics.com/TiSapphire-Laser-Kits/TiSaKits.htm, Accessed 12/2/2013.

[15] G. Caryotakis. "ILC Klystron Design Options." Snowmass Workshop. Snowmass, CO. August 15, 2005.

[16] F. Jones, "High-rate reactive sputter deposition of zirconium dioxide," Journal of Vacuum Science and Technology A: Vacuum, Surfaces, and Films(1988).

[17] A. Tremaine, J. B. Rosenzweig, and P. Schoessow. "Electromagnetic wake fields and beam stability in slab-symmetric dielectric structures", Phys. Rev. E 56, 7204 (1997).

[18] R.Yoder and J.B.Rosenzweig. "A Slab-Symmetric Dielectric-Loaded Structure for High-Gradient Acceleration at THz," Phys. Rev. ST Accel. Beams 8, 111301 (2005).

[19] C.K. Ng et al., "Transmission and radiation of an accelerating mode in a photonic band-gap fiber," Phys. Rev. ST Accel. Beams 13, 121301 (2010).

[20] X.E. Lin, Photonic band gap fiber accelerator, Phys. Rev. ST Accel. Beams 4, (2001).

[21] R.J. England et al., "Experiment to Detect Accelerating Modes in a Photonic Bandgap Fiber," Proc. of the Thirteenth Advanced Accelerator Concepts Workshop, Santa Cruz, California, USA,550-555 (2008).

[22] Cowan, B. M. , Phys. Rev. ST Accel. Beams 11, 011301 (2008).

[23] Ho, K. M., C. T. Chan, C. M. Soukoulis, R. Biswas, and M. Sigalas, Solid State Commun. Vol.89 No.5, 413 (2008).

[24] Z. Wu et al. "Design of On-Chip Power Transport and Coupling Components for a Silicon Woodpile Accelerator," SLAC-PUB-14413 (2012).

[25] T.Plettner, P. P. Lu, and R. L. Byer, Phys. Rev. ST Accel. Beams 9, 111301 (2006).

[26] E. Peralta, in Proc. of the 2011 Particle Accelerator Conference, IEEE, 280 (2008).

[27] T.Plettner, R. L. Byer, and B. Montazeri , J. Mod.Opt. 58, 1518 (2011).

[28] E. Peralta, J. McNeur et al., Demonstration of Electron Acceleration in a Laser-Driven Dielectric Micro-Structure, Nature Vol.503 No.7474,91-94 (2013).

[29] T.Remetter, P.Johnsson, J.Mauritsson, K.Varju, Y.Nu, et al.,"Attosecond electron wave packet interferometry," Nat. Phys. 2,323326 (1994).

[30] G.Travish,"Dielectric Laser Accelerators: Are They Viable Advanced Accelerator Concepts?" Advanced Accelerator Concepts Workshop. Austin, TX. June 15, 2010.

[31] R.Yoder, "Theory of Slab-Symmetric Accelerating Structures," Internal Technical Note, October 2006.

[32] A. Mizrahi and L. Schachter, "Optical Bragg Accelerators," Phys. Rev. E 70, 016505 (2004).

[33] A.E. Vlieks, et al. Recent measurements and plans for the SLAC Compton X-ray source, SLAC-PUB-11689, 2006. 10pp. Published in AIP Conf.Proc.807, 481-490 (1994).

[34] T.Weiland, "Time Domain Electromagnetic Field Computation with Finite Difference Methods,"International Journal of Numerical Modelling: Electronic Networks, Devices and Fields, Volume 9, Issue 4, 295319 (1996).

[35] A.Tremaine, J.B.Rosenzweig and P. Schoessow. "Electromagnetic wake elds and beam stability in slab-symmetric dielectric structures," Physical Review E 56 6(1997).

[36] R.Kitamura, L.Pilon, M.Jonasz, "Optical Constants of Silica Glass From Extreme Ultraviolet to Far Infrared at Near Room Temperatures". Applied Optics 46 33,81188133 (2007).

[37] J. Zhou, et al, Fabrication of a Prototype Micro-Accelerator Platform, in Proceedings of 2011 Particle Accelerator Conference, IEEE (2011).

[38] E. Sozer, Internal Document, January 2013.

[39] D.McMullan, "Scanning electron microscopy 19281965". Scanning 17 3, 175(2006).

[40] L.Taiz and E.Zeiger,"Companion to Plant Physiology, Fifth Edition." http://5e.plantphys.net/article.php?ch=t[ampersand]id=66, Accessed 12/1/2013.

[41] E.Sozer, J.McNeur et al.,"Experimental progress towards laser acceleration of relativistic electrons with the Micro Accelerator Platform (MAP)," Pulsed Power Conference (PPC), 2013 19th IEEE , vol.1, no.5,16-21 (2013).

[42] R.D. Ruth, "The Development of the Next Linear Collider at SLAC," *Proc. of Workshop on Physics and Experiments with Linear Colliders*, Saarieselka, Finland, 191.

[43] R.J.England, Internal Technical Note, November 2012.

[44] Ginzburg V L and I M Frank, JETP, 16,1(1946).

[45] H. A. Macleod, Thin-Film Optical Filters. 4th ed. CRC Press/Taylor and Francis, (2010).

[46] E.Sozer., J.McNeur, K.Hazra, G. Travish "Laser-Induced Damage in a Dielectric Laser Accelerator," Under Development.